A COUPLED LATTICE-BOLTZMANN – NAVIER-STOKES METHODOLOGY FOR DRAG REDUCTION

A Dissertation
Presented to
The Academic Faculty

by

Nandita Yeshala

In Partial Fulfillment
of the Requirements for the Degree
Doctor of Philosophy in the
School of Aerospace Engineering

Georgia Institute of Technology
December 2010

A COUPLED LATTICE-BOLTZMANN – NAVIER-STOKES METHODOLOGY FOR DRAG REDUCTION

Approved by:

Dr. Lakshmi N. Sankar, Advisor
School of Aerospace Engineering
Georgia Institute of Technology

Dr. Jeff I. Jagoda
School of Aerospace E`ngineering
Georgia Institute of Technology

Dr. Suresh Menon,
School of Aerospace Engineering
Georgia Institute of Technology

Dr. Preston Martin
US Army Aeroflightdynamics Directorate
Aeromechanics Branch AFDD

Dr. Stephen M. Ruffin
School of Aerospace Engineering
Georgia Institute of Technology

Date Approved:[November 04, 2010]

Dedicated to,
My Father, Late Mr. Markandaiah Yeshala,
My Mother, Mrs. Parvathi Yeshala,
My Brother, Mr. Venu Madhav Yeshala.

ACKNOWLEDGEMENTS

I would like to express my sincere thanks to my thesis advisor, Dr. Lakshmi N. Sankar, for his guidance, advice and support throughout my research work. It has been a great learning experience to pursue my PhD under his guidance.

I would like to thank my thesis reading committee, Dr. Lakshmi N. Sankar, Dr. Suresh Menon, Dr. Stephen M. Ruffin, Dr. Jeff I. Jagoda and Dr. Preston Martin for providing valuable feedback on my work. I would especially like to thank my external reading committee member, Dr. Preston Martin for his encouragement and active participation during my work on the thesis project.

I would like to thank my colleagues, Dr. Sarun Benjanirat, Dr. Chanin Tongchitpakdee, Dr. Vishwas Iyengar, Sujeet Phanse, Dr. Mina Zaki, Goktan Guzel, Dr. Byung-Young Min, Dr. Nischint Rajmohan, Jeremy Bain, Ritu Priyanka Marpu, and Jeewoong Kim for the friendly atmosphere and support during my years in the lab. I would like to specially thank Dr. Byung-Young Min for the use of his solver for my work and for the innumerable valuable discussions regarding my research work.

I would like to thank all my friends, in India, as well as in and outside the United States, for their friendship and support.

Last but definitely not the least; I owe my deepest gratitude to my parents and brother, Markandaiah Yeshala, Parvathi Yeshala and Venu Madhav Yeshala for their encouragement and love. Their constant support and guidance has brought me to this stage. I dedicate this thesis work to them. I hope my father could see me achieve this goal he dreamed for me.

TABLE OF CONTENTS

LIST OF TABLES

Page

LIST OF FIGURES

Page

NOMENCLATURE

a	Speed of sound
A, B, C	Flux Jacobian matrices
A	Jet amplitude
A_j	Area of cross section of the jet slot
c	Chord
C_d	Drag coefficient
C_{d0}	Profile drag coefficient
C_l	Lift coefficient
C_p	Specific heat at constant pressure, pressure coefficient
C_μ	Jet momentum coefficient
c_s	Speed of sound in lattice units
d	Distance from the wall
D	Number of dimensions, Lower, diagonal and upper block triangular matrix
e	Total energy per unit volume
ei	Velocity vector in lattice domain
E, F, G	Inviscid flux matrices
E_v, F_v, G_v	Viscous flux matrices
f	Particle density distribution function (PDF)
f_{eq}	Local equilibrium PDF
f_{v1}	Viscous damping function
f_j	Jet actuation frequency in Hertz
$F+$	Reduced jet actuation frequency

g	Acceleration of gravity, external force
h_0	Specific total enthalpy
I	Identity matrix
J	Jacobian of transformation, outstroke
k	Thermal conductivity
Kn	Knudsen number
l	Length
L	Lift force, Reference length
L, U	Lower, diagonal and upper block triangular matrix
$\dot{m}_J$	Mass flow rate into or from active flow control device
M	Mach number, Million
max	Maximum
n_t	Grid velocity in the surface normal direction
n_x, n_y, n_z	Surface normal vector
N	Total number of velocity vectors, number of lattice sites, number of gas molecules
$\mathcal{O}$	Order
p	Pressure
P_j	Power used by the active flow control device
P_s	Power saved by the active flow control device
Pr	Prandtl number
Pr_t	Turbulent Prandtl number
q	Primitive variable
Q	State variable vector
Q	Number of distinct lattice velocities
R	Riemann invariant, cylinder radius, Boltzmann constant

Re	Reynolds number
RHS	Shorthand notation for the terms on the right hand side for any equation
S_{ij}	Strain rate
St	Strouhal number
t	Time
t_i	Weighting factor
T	Temperature, time period of the lift curve
u, v, w	Cartesian components of velocity
U, V, W	Contravarient velocity
V	Velocity
$\forall$	Volume
V_j	Velocity of the jet
w	Weights
W	Weighting function
x, y, z	Cartesian coordinates
x	Position vector
y^+	Viscous sub-layer length scale ($y\sqrt{\rho\tau_w}/\mu$)

Greek Symbols

δ	Central difference operator
Δ	Difference, Grid spacing
ε	Turbulent dissipation
ϕ	Limiter function, Phase angle
γ	Specific heat ratio
κ	Turbulent kinetic energy
λ	Eigenvalue, mean free path, characteristic velocity

η	Efficiency of the active flow control device
μ	Viscosity, Advance ratio
μ_l	Molecular viscosity
μ_t	Turbulent viscosity
ν	Kinematic viscosity
Ω	Collision operator
Ψ	Moment function
ρ	Denisty
ρ_{m}	Mean density of the fluid
ρ_{j}	Density of the jet
ρ_∞	Density of the free stream
σ	Cross section
τ	Time period, single time relaxation parameter, collision time
τ_{ij}	Shear stress tensor component
θ	Circumferential angle around cylinder
ω	Turbulent specific dissipation, solid angle
ξ, η, ζ	Curvilinear coordinates
ξ	Microscopic velocity, momentum

Subscripts

0, ∞, inf, ref	Reference value
d	Dimensionless units
i, j, k	Indices in three coordinate directions
jet	Jet parameter
lb	Lattice units
L, R	Left and right sides of the cell faces

min	Minimum
max	Maximum
n	Normal direction
p	Pressure, physical unit
t	Derivative with respect to time
$wall$	Variable on the wall surface
x, y, z	Derivatives with respect to Cartesian coordinates
ξ, η, ζ	Derivatives with respect to curvilinear coordinates

Superscripts

-1	Inverse matrix
l, r	Left and right sides of the cell faces
n, n+1	Time level
*	Non-dimensional variable
∧	Dimensional variable
–	Matrix in the computational domain
~	Roe-averaged quantity
+	Positive eigenvalue
-	Negative eigenvalue
'	Fluctuation quantity after average

Acronyms and Abbreviations

2-D	Two Dimensional
3-D	Three Dimensional
AFC	Active flow control
BBGKY	Bogoliubov, Born, Green, Kirkwood and Yvon hierarchy

BC	Boundary Condition
BGK	Bhatnagar-Gross-Krook
BL	Baseline
CFD	Computational Fluid Dynamics
DPD	Dissipative particle dynamics
DSMC	Direct simulation Monte Carlo
FHP	Frisch-Hasslacher-Pomeau
HPP	Homogenous Poisson process
LB	Lattice Boltzmann
LBE	Lattice Boltzmann Equation
LBGK	Lattice Boltzmann Bhatnagar Gross Krook Model
LBM	Lattice Boltzmann Method
LGCA	Lattice-gas cellular automata
FDS	Flux Difference Splitting
LU-SGS	Lower-Upper Symmetric Gauss Seidel
MBT	Micro Blowing Technique
MD	Molecular dynamics
MEMS	Micro-electro-mechanical systems
MRT	Multiple-relaxation time
MUSCL	Monotone Upstream-centered Scheme for Conservation Laws
NS	Navier-Stokes
ODE	Ordinary differential equation
PDE	Partial Differential Equation
PDF	Particle distribution function
RANS	Reynolds Averaged Navier-Stokes

RHS	Right Hand Side
SA, S-A	Spalart-Allmaras
SJA	Synthetic jet actuator
SPD	Smooth-particle hydrodynamics
SRT	Single relaxation time
UFS	Unified Flow Solver
VDF	Velocity distribution function

SUMMARY

Helicopter performance is greatly influenced by its drag. Pylons, fuselage, landing gear, and especially the rotor hub of a helicopter experience large separated flow regions, even under steady level flight conditions the vehicle has been designed for, contributing to the helicopter drag. Several passive and active flow control concepts have been studied for reducing helicopter drag. While passive flow control methods reduce drag, they do so at one optimized design condition. Therefore, passive drag reduction methods may not work for helicopters that operate under widely varying flight conditions. Active flow control (AFC) methods overcome this disadvantage and consequently are widely being pursued.

The present investigator has studied some of these AFC methods using computational fluid dynamics (CFD) techniques and has found synthetic (or pulsed) jets as one of the more effective drag reduction devices. Two bluff bodies, representative of helicopter components, have been studied and the mechanism behind drag reduction has been analyzed. It was found that the increase in momentum due to the jet, and a resultant reduction in the separated flow region, is the main reason for drag reduction in these configurations. In comparison with steady jets, synthetic jets were found to use less power for a greater drag reduction.

The flow inside these synthetic jet devices is incompressible. It is computationally inefficient to use compressible flow solvers in incompressible regions. In such regions, using Lattice Boltzmann equations (LBE) is more suitable compared to solving the incompressible Navier-Stokes equations. The length scales close to the synthetic jet devices are very small. LBE may be used to better resolve these small length scale

regions. However, using LBE throughout the whole domain would be computationally expensive since the grid spacing in the LBE solver has to be of the order of the mean free path. To address this need, a coupled Lattice Boltzmann-Navier-Stokes (LB-NS) methodology has been developed.

The LBE solver has been successfully validated in a standalone manner for several benchmark cases. The solver has also been shown to be of second order accuracy. This LBE solver has been subsequently coupled with an existing Navier-Stokes (NS) solver. Validation of the coupled methodology has been done for analytical problems with known closed form solution.

This LB-NS methodology is further used to simulate the flow past a cylinder where synthetic jet devices have been used to reduce drag. The LBE solver is used in the cavity of the synthetic jet nozzle while the NS solver is employed in the rest of the domain. The cylinder configuration was chosen to demonstrate drag reduction on helicopter hub shape geometries. Significant drag reduction is observed when synthetic jets are used, compared to the baseline no flow control case.

CHAPTER 1

INTRODUCTION

Bluff-body drag is the main contributor to the overall drag of a helicopter. The range, endurance, and maximum speed of a rotorcraft are significantly influenced by the vehicle drag. Pylons, rotor hubs, fuselage and landing gear of a helicopter experience large separated flow regions even under steady level flight conditions the vehicle has been designed for. Figure 1.1 shows these components on a RAH-66 Comanche. These components may experience additional separation in case of high angles of attack, yaw, pitch, gusts and flight maneuvers, even if they are aerodynamically optimized for a single design condition. In addition, the huge separation regions increase interference drag.

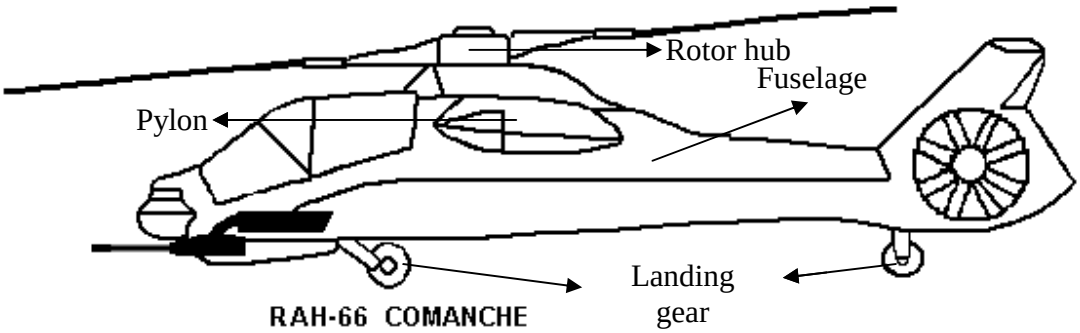

Figure 1.1: Rotor hub, pylon, fuselage and landing gear on a RAH-66 Comanche helicopter [1].

As Table 1.1 below indicates, even with a highly streamlined fuselage, and a streamlined hub configuration, the interference effects can lead to a total drag that is unacceptably high, degrading vehicle performance. Active and passive approaches for reducing the hub drag and hub interference drag are urgently needed.

Table 1.1. Vehicle Drag Breakdown (Ref. [1]- Prouty: Helicopter Performance, Stability, and Control)

Helicopter	OH6A	UH-1B	CH-47
Gross weight, lb	2550	9500	33000
Main rotor disc area, sq ft	550	1520	5900
f, Fuselage and nacelle, sq.ft	1.5	5	16.1
f, rotor hubs, sq.ft	1.2	5.5	14.1
f, Landing Gear, sq.ft	0.5	3	7.9
f, Empennage, sq ft	0.1	0.9	0
f, Miscellaneous, sq ft	1.7	5.1	5.1
Total f, sq ft	5	19.5	43.2
f/A	0.009091	0.012829	0.007322

1.1 Literature Study of Hub Drag Reduction Concepts

A number of flow control approaches for reducing hub drag have been studied by researchers. Flow control aims at improving the performance of a system involving fluid flow by means of inducing desirable changes to the flow. The common fluid-mechanical phenomena targeted by flow control are [3][4]:

- Delaying or accelerating laminar-to-turbulence transition.
- Suppressing or enhancing turbulence.
- Preventing or causing flow separation.

Various benefits are expected from such flow manipulations: drag reduction, lift improvement, mixing enhancement and flow-induced noise attenuation [5].

The flow control methods are classified into two categories according to their energy expenditure. In active flow method, external energy is introduced into a fluidic system via actuators. In contrast, passive flow control does not utilize external power sources [5].

1.1.1 Passive Concepts

Stroub et al. [2] have conducted experiments to study the effects of fairing, camber, lower surface curvature, and relative size of the hub on hub drag. These investigators also examined the effects of gap and hub fairing inclination on drag. In a follow-on study, Stroub [14] investigated the use of a large circular fairing on drag reduction. Larry Young et al. [15] have examined hub-fairing camber, hub-fairing thickness ratio, hub-fairing surface curvature, hub-fairing height with respect to the fuselage, inclusion of blade shanks in the hub fairings, hub- and pylon-fairing gaps, pylon-fairing cross-sectional geometry, pylon-fairing thickness ratio and camber.

Other passive approaches in use include rounding sharp corners, sealing the gaps, use of strakes, and add-on flow vanes [16]-[19]. Saltzman et al [16] showed a 40 percent reduction in aerodynamic drag of a delivery van when it's four square-shaped vertical corners were rounded. Add-on devices were shown to reduce aerodynamic drag up to 25 percent on a representative cab-over-engine tractor-trailer combination by Montoya et al [18],[19]. These concepts have been extensively studied in the context of automotive and truck aerodynamics. These concepts are extensively used in industry and found to be helpful in hub drag reduction. Although these methods have the advantage of being simple, one of their major drawbacks is that they are optimized for a single design condition.

There are several biologically inspired passive concepts. It is known that aquatic animals are superior to technologies developed by aeronautical engineers in a number of ways. Dolphins can achieve speed in excess of 10 m/s, while fish can accelerate at rates in excess of 50 m/sec^2. A variety of physical mechanisms contribute to this superior

performance. The addition of long polymer chains is known to reduce viscous drag. The mucus secreted over a fish surface is considered to contribute to the drag reduction. Sharks and other mammals have riblets on their skin which are known to act as fences that break up spanwise vortices, reduce skin friction, and decrease momentum loss. Compliant skins, essentially an elastic skin on top of the underlying dermis are considered effective in damping out instabilities that cause transition to turbulence. Constructive interference of vortices from the caudal fins of fish has been postulated as enhancing the propulsive efficiency. Finally leading edge bumps were found to behave like strakes on aircraft and may create vorticity that constructively interferes with stall and associated drag. Figure 1.2 shows a typical vortex generator, similar to riblets which help in drag reduction [20]. The dimpled, riblet-like, surface on golf balls [21] used to reduce separation is shown in Figure 1.3. It can be seen that due to the riblets, the flow separation is delayed and results in a thinner wake and therefore reduced drag. Reidy [22] showed a reduction of 8 percent in the drag of a flat plate in a water tunnel using v-groove riblets. The optimization of the riblet spacing for drag reduction was studied by Anderson et al [23]. Experiments conducted by Blick and Walters [24] on compliant surfaces showed a reduction in skin friction drag compared to a hard plate surface. Miklosovic et al [25] showed that scalloped leading-edge airfoils, similar to those in humpback whale flippers, reduce drag by enabling greater momentum exchange within the boundary layer which helps keep the flow attached. Drag minimizing design characteristics based on swimming of dolphins has been reviewed by Fish [26]. These characteristics include the streamline body shape and as well as appendages like the

dorsal fin which have round leading edges and tapering trailing edge which provide 'laminar' shapes for low drag.

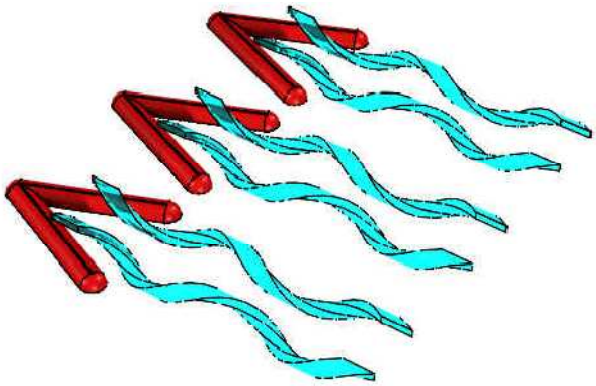

Figure 1.2: Vortex generators, Ref. [20]

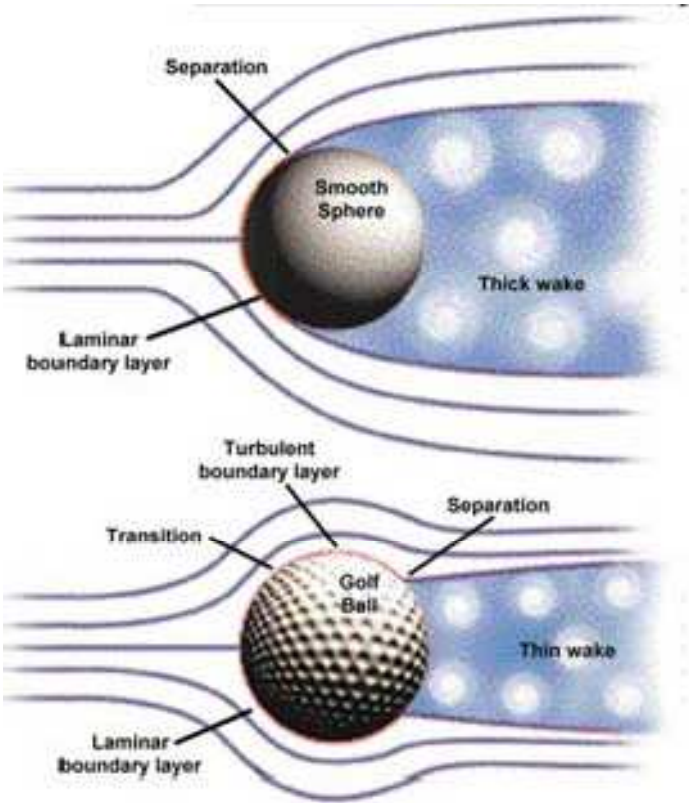

Figure 1.3: Reduction in the separated region in the wake of the sphere due to the dimpled riblet-like surface on a golf ball, Ref. [21].

1.1.2 Active Techniques

Active drag reduction concepts attempt to alter the wall shear layer behavior, and have been used in a number of ways. Some biologically inspired active flow control concepts are studied in Refs. [27],[28]. Triantafyllou et al [27] studied an oscillating NACA0012 airfoil to obtain the optimal frequency of oscillation for most efficient thrust from the airfoil. It was found that this optimal frequency is within a range which is same as that found in many fish that were also studied. Extending this work, Gopalakrishnan et al [28], used an oscillating airfoil in the wake of the cylinder in order to change the wake vorticity and its strength in a way that is considered desirable. This is considered similar to the oscillation of a fish tail fin compared to its main body.

Coanda jets keep the boundary layer attached to a highly curved surface and may be used to increase lift and decrease drag. Figure 1.4, reproduced here from Ref. [29], indicates how the trailing edge vortex shedding characteristics of a bluff body may be modified with blowing. Suction is often used for removal of low velocity reversed flow regions. A suction slot positioned within a separation bubble could remove the low momentum fluid and delay separation. Blowing may be used to energize the boundary layer by adding high momentum fluid into the boundary layer where the momentum is low. Blowing and circulation control require an external supply of compressed air, while suction requires a pump that will remove the low velocity flow and discharge it elsewhere in the flow. The ability of blowing or suction to modify the wake has been documented by William et al [30]. They experimentally observed that by suction or blowing of fluid through two rows of small holes on the cylinder surface, significant disturbances were produced which modified the pattern and frequencies of vortex shedding and the mean

flow. Kim and Choi [31] observed that in-phase forcing (suction or blowing) from two slits located at $\pm 90^{o}$ on the cylinder surface reduced drag and also attenuated vortex shedding. However, these concepts are thus difficult to employ in the hub region, particularly over rotating components (blade shank, pitch link, etc).

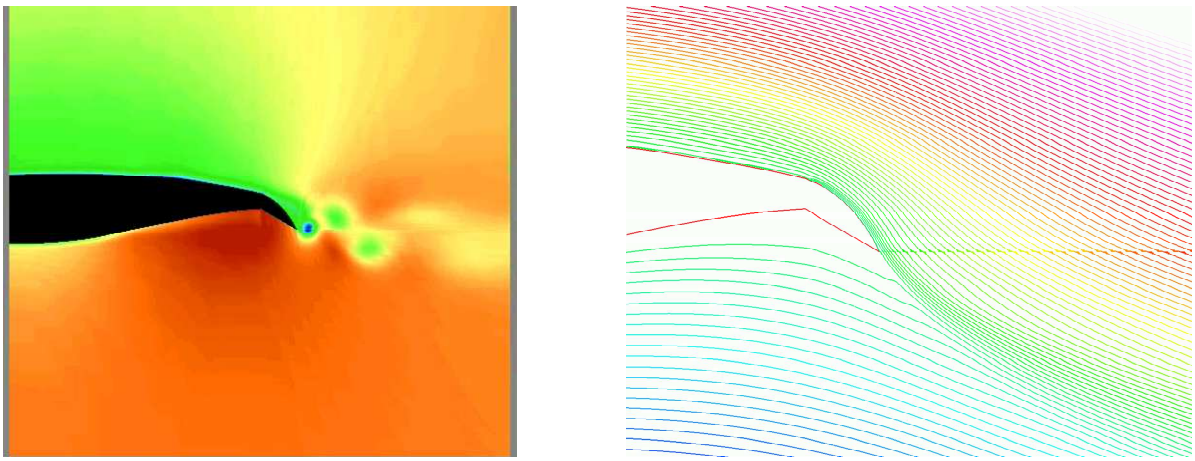

Figure 1.4: Effects of Coanda Jets on Trailing Edge Separation (Calculations by Yi Liu and L. Sankar, Ref. [29]).

1.1.2.1 Synthetic jet actuators

Synthetic jets have been proposed as an alternative and successfully used in literature to overcome these requirements [32]-[41]. Typically, a Synthetic Jet Actuator (SJA), consists of a closed cavity, an exit orifice on one side and an oscillating boundary on the other. The closed volume inside the actuator resonates with the oscillating boundary and thus the concentrated jets are ejected through the exit orifice. When the jets cross the orifice, viscous effects resulted in the vortical structures [6]. A series of vortices advancing to the external flow are referred to as “synthetic jets“.

The unique feature distinguishing synthetic jets from other methods is that synthetic jets are created from the periodic suction and blowing of a working fluid so that

the energy can be transferred to the flow without adding extra mass. In that sense, synthetic jets are widely known as “zero-net-mass flux flow”. Therefore, a SJA can operate in a stand-alone manner without any extra piping or fluidic packages and thus can be simply fabricated and easily integrated into fluidic systems [7]. This is one of the main advantages of using synthetic jet devices. Also, power required to drive these devices is lower compared to the steady blowing or suction.

Synthetic jets are composed entirely of entrained ambient fluid synthesized by the formation of a time-harmonic train of vortices that are created at the sharp edges of an orifice of an enclosed cavity. The fluid is drawn into and then pushed out of the cavity by the time periodic motion of an oscillating diaphragm, commonly made of a piezoelectric material, enclosed inside the cavity resulting in zero net mass flux across the orifice. This phenomenon is shown in Figure 1.5 [7]. During the in-stroke, the cavity expands, pressure decreases and low momentum air from the boundary layer above the orifice is drawn into the cavity. During the out-stroke, the volume is contracted and the cavity pressure increases forcing air out of the cavity. The shape mode (deflection) of the diaphragm at a given instant dictates amount of displaced fluid and hence the details of the instantaneous flow field through the orifice and the formation of the synthetic jet. A schematic of a synthetic jet actuator and the above mentioned mechanism is shown in Figure 1.6 from Ref. [7].

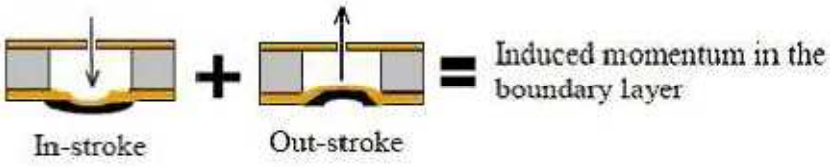

Figure 1.5 : Concept of a synthetic jet actuator, Ref. [7]

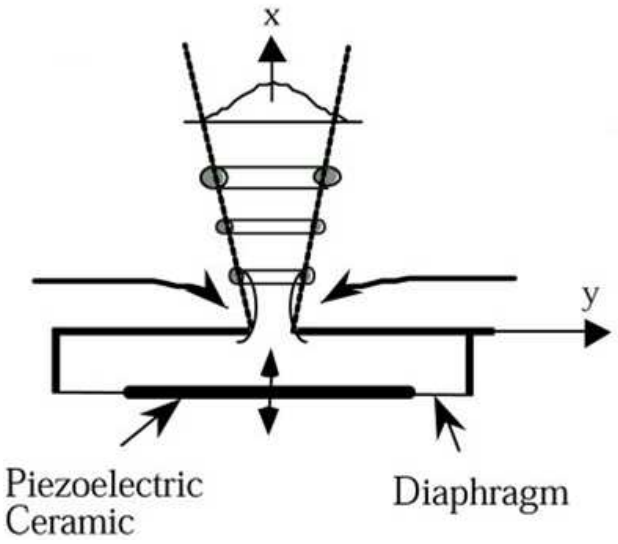

Figure 1.6: Schematic of a synthetic jet actuator, Ref [7].

The parameters that characterize synthetic jets have been broadly investigated. First, two parameters are defined to identify the feature of the vortices created by the jets [8]. The first parameter is a dimensionless stroke length, $L_0/d = \frac{1}{d}\int_0^\tau u_0(t)dt$, where $u_0(t)$ is the velocity at the jet exit slot, τ is half of an oscillating period and d the characteristic length scale of an jet exit slot. The second is the Reynolds number based on the impulse, $Re_{I_0} = I_0/\mu d$ $\left(I_0 = \rho d \int_0^\tau u_0^2(t)dt\right)$, where ρ is fluid density and μ is viscosity.

Particularly, in case that synthetic jets are involved for flow separation control, the amplitude and frequency of the oscillating jets are regarded as key parameters. This is due to the fact that a basic mechanism of synthetic jets is the amplification of shear layer instability by periodic excitation. The reduced jet actuation frequency, *F+*, is defined as

$$F^{+} = \frac{f_j L}{U_\infty} \tag{1.1}$$

where f_j is the actuation frequency (Hz), L the characteristic length of the separated region and U_∞ the free stream velocity. Physically, the inverse of this dimensionless property stands for the ratio of one period of jet actuation to the time of flight of free stream over the controlled surface [9].

To achieve control of vortex shedding and delay flow separation, F^{+} is typically kept of O(1) to match the natural instabilities associated with vortex shedding within the lock-in range. The lock-in range is the range of actuation frequencies to which the flow will respond with periodic shedding of vortices [10]. Some researchers use F^{+}= O(10) for vortex shedding suppression. Current designs for synthetic jet actuators include devices that have a resonance frequency different (usually much higher) than their application demands. In such designs, the resonance frequency is used as a carrier frequency and the actuator is pulsed at the shedding frequency for modulated actuation.

Previous research has established that 2 ~ 4 vortices should stay constantly on the controlled surface for the effective separation control and that the jet frequency operating within the range of $0.5 \leq F+ \leq 1.5$ creates those number of vortices regardless of the Reynolds number [9]. Moreover, the jet amplitude is associated with a jet momentum coefficient

$$C_\mu = J/\frac{1}{2}\rho L U_\infty^2, \quad \left(J = \frac{1}{\tau}\rho d \int_0^\tau u_0^2(t)dt\right) \tag{1.2}$$

which represents the momentum ratio between jets and free stream velocity [12]. This coefficient may be rewritten in terms of the jet amplitude, A, as follows.

$$C_\mu = \frac{(\rho dA)_{jet}}{(\rho LU)_\infty} \tag{1.3}$$

Many experiments have been conducted using SJAs to affect the aerodynamic flow characteristics of airfoils and bluff bodies. The most significant work with circular cylinders that is related to this research comes from Amitay in the late 1990s [32]. A thorough review of synthetic jets is presented in a paper by Glezer and Amitay [7]. Some applications for synthetic jets include improved heat transfer, jet vectoring, enhancing mixing, and controlling a turbulent boundary layer for drag reduction. A very rich body of literature exists in the area of flow control, and even a cursory discussion of these concepts is not attempted here. This concept has been used for the modification of the aerodynamic characteristics of bluff [32][33], control of lift and drag on airfoils [35]-[38], reduction of skin friction of a flat-plate boundary layer [39], mixing in circular jets [40], and control of internal flow separation [41]. Amitay et al [32][33] showed a reduction in drag of a cylinder with the use of synthetic jet actuators which essentially modified the shape of the bluff body. Increased lift and reduced pressure drag on airfoils was observed by Amitay et al [35]-[37] due to the attached flow that could be maintained on thick airfoils at angles of attack as high at 17.5^o with the use of AFC. Seifert and Pack [38] observed a delay in stall and improvement in post stall characteristics of a NACA0015 airfoil at high Reynolds number when oscillatory blowing was applied from the leading-edge region of the airfoil. Lorkowski et al [39] observed a 7 percent reduction in wall shear stress when an actuator was coupled with shear sensor units by an adaptive feed-forward control algorithm. Substantial increases in spreading rate and entrainment of the primary turbulent circular jet were observed by Davis and Glezer [40] by

employing controlled, azimuthally placed, synthetic jets at the exit of the primary jet. This is seen as a result of the temporal control of the large-scale structures within the flow by the amplitude modulation of the synthetic jets. Amitay et al [41] demonstrated that synthetic jet actuators placed downstream of the separation point of a two-dimensional serpentine duct model reattach the flow up to a Mach number of 0.3 with a momentum coefficient of the order of 10^{-4}. Flow reattachment reduces losses within the duct and can increase the volume flow rate. The reader is referred to references [42]-[49] for additional representative examples of drag reduction and flow control.

1.2 Multiscale Phenomena

The present study focuses on drag reduction through active flow control (AFC) methods including steady and synthetic jets. The sizes of the slots through which the jets emerge are usually much smaller than the characteristic length of the helicopter component under consideration. This difference in sizes leads to large differences in length scales between the flow close to the jet slot and far away from it. Length scales can be characterized using Knudsen number (Kn), which is defined as the ratio of the mean-free-path (λ) to the characteristic length scale (L). Based on this definition of Kn, it can be said that the problem of the flow past a bluff body where AFC has been employed, involves a wide range of Knudsen numbers. Therefore, it is a multi-scale phenomena problem.

Small Kn (< 0.03) represents the continuum flow since $\lambda << L$ and the flow is assumed to be continuous. In this regime, aerodynamics problems can be solved by using the Navier Stokes (NS) equations. For λ larger than L, say $Kn > 1$, aerodynamics concepts based on continuum break down and Boltzmann equation is the only equations

that can describe this free-molecular regime. This is called low-density flow and it is resolved using kinetic theory concepts with discrete particle models. Slip effects become important in the transition regime where $0.03 < Kn < 1$. For a subset of the transition regime, $0.03 < Kn < 0.2$, NS equations can be used if slip effects are included at boundary conditions. The criteria for the use of continuum and discrete particle models along with the equations used to resolve the flow field in different Kn regimes is shown in Figure 1.7.

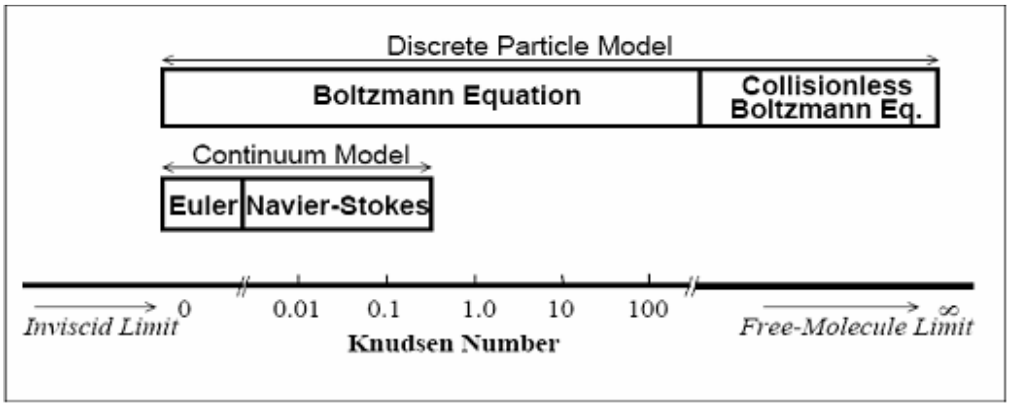

Figure 1.7: Range of applicability for Boltzmann equation and Navier-Stokes equations based on Knudsen number

Solving the Boltzmann equation is a nontrivial task, from both physical and numerical point of views. A large number of methods have emerged in the past few decades, which include molecular dynamics (MD) [51], direct simulation Monte Carlo (DSMC) [52], dissipative particle dynamics (DPD) [53], smooth-particle dynamics (SPD) [54], Lattice-gas cellular automata (LGCA) [55][56] and Lattice Boltzmann equation (LBE) [62]. Most of these methods are computationally intensive and suitable for certain scale ranges only. In the MD method, the exact trajectories of individual particles are calculated. DSMC simulates molecular interactions of particles, which represents groups

of molecules having the same properties such as velocity and temperature. The inter-particle collision is carried out according to probability of collision, i.e., pairs of molecules are selected randomly for elastic collision within a cell or subcell. Since in the DSMC method, the number of particles distributed in the field is directly related to the number of molecules, the computational effort is usually very large. The DPD scheme is similar to MD in that the particles move according to Newton's laws, but in DPD approximate terms are used to reduce the fast degrees of freedom so that the slow phenomena in, for example, polymer solutions may be studied. SPD consists of the discretization of the Navier-Stokes equations in a Lagrangian moving grid with the aid of a weight function. Therefore, the nodes of the grid can be identified as "smooth particles" interacting through prescribed laws of force, thus allowing to solve the Navier-Stokes equations with MD codes.

A particularly promising method is the Lattice Boltzmann method (LBM), which is a mesoscale method connecting the microscopic and macroscopic descriptions of the flow dynamics. Unlike the DSMC method, the number of particles distributed in the field is not related to the number of molecules in the LBM. Instead, it is only dependent upon the number of mesh points and the lattice model. Therefore, it is much more computationally efficient than the DSMC method [50], as discussed in the next section.

For the case of helicopter components which use AFC, the flow can be resolved using NS equations. However, in the vicinity of the AFC devices, where the length scales are very small compared to the characteristic length of the flow and the flow is incompressible, it is preferable to use incompressible flow solvers. While an incompressible Navier-Stokes equations can be used, there are several advantages of

using the Lattice Boltzmann equation in these regions. These advantages will be detailed in Chapter 2. Although LBE can also be used to model low Kn regimes, away from AFC devices, it is computationally inefficient to do so since LBE solvers require the lattice spacing to be of the order of the particle mean free path. Therefore, it is necessary to develop solvers which would couple NS and LBE methodologies to model such multiscale phenomena.

1.3 Literature Review of the Lattice Boltzmann concept

The Lattice Boltzmann method (LBM) emerged from Lattice gas automata (LGA) which was first proposed by Hardy and Pomeau [55] in 1972. The first LGA model was developed by Hardy et al. [56] and was known as the homogeneous Poisson process (HPP). However, the lack of Galilean invariance and the lack of isotropy lead to insufficient symmetry for Navier-Stokes equations recovery. Fisch et al. [57] developed the Frisch-Hasslacher-Pomeau (FHP) model which restored the Galilean invariance macroscopically as well. The LGA proposed by Frisch et al was a two-dimensional model representing the incompressible Navier-Stokes equations. Since then LGA have shown promise in solving a variety of partial differential equations and modeling physical phenomena [58]-[60].

A lattice gas automaton is constructed as a simplified, fictitious microworld in which space, time and particle velocities are all discrete. It consists of a regular lattice with particles residing on the nodes. The Boolean variables 0 and 1 represent the presence or absence or a particle at the node. Particles move from the present node to the neighboring node in a process called streaming. When particles move to the same site, collision occurs and the particles are redistributed according to a set of collision rules.

LGA had two problems: (a) a non-Galilean invariance property due to density dependence on the convection coefficient and an unphysical and explicit pressure dependence on velocity [61] and (b) inherent large amount of statistical noise.

In order to avoid these problems, several lattice Boltzmann equation (LBE) models have been proposed [62]-[69]. In the Lattice Boltzmann methods (LBM), the statistical noise is corrected by replacing the Boolean variables with a particle distribution function represented by floating point variables between 0 and 1. This LBE as a numerical scheme was first proposed by McNamara and Zanetti [62]. In their model, the form of the collision operator is the same as in the LGA, written in terms of distribution functions and completely neglecting the effects of correlations between particles. Higuera et al. [63][64] introduced a linearized collision operator that is a matrix and has no correspondence to the detailed collision rules. Chen et al. [66][68] and Qian et al. [65][67] proposed an LBM which does not use the Fermi-Dirac statistics used in earlier models. Also, it provides the freedom required for the equilibrium distribution to satisfy isotropy, Galilean invariance and to possess a velocity-independent pressure. The models in references [66]-[68] apply the single relaxation (SRT) approximation for the local equilibrium. SRT was first introduced by Bhatnagar, Gross and Krook [70] in the lattice Boltzmann BGK model (LBGK). This approximation assumes a single constant collision time during the LBE solution process, i.e. all the modes relax with exactly the same relaxation time.

Rothman and Zaleski [71] give a detailed derivation of the lattice Boltzmann equation which is the origin of both LGA and LBE. The formal connection between the lattice Boltzmann equation and the continuous Boltzmann equation was done in papers

by Luo and He [72][73] and Abe [74]. D'Humières [75] constructed a LBE model in moment space based on the generalized lattice Boltzmann equation. Dispersion, dissipation, isotropy, Galilean invariance and stability of this model was studied in detail by Lallemand and Luo [76]. In order to reduce dispersion and improve computational stability compared to SRT, multiple-relaxation time (MRT) was developed [76][77]. MRT is shown to have smaller regions of oscillations near singularities and offers a better convergence towards steady state [78] compared to SRT.

Three-dimensional work has been performed by Feiz et al[79] for square jets in cross flow using LBE-LES (Large Eddy Simulation). This work was then extended by Menon and Soo[80]. Corrections were made for convex edges and corners where the no-slip boundary condition was previously not satisfied due to insufficient unknown populations. While these simulations used single time relaxation (SRT) technique, work by Orphee et al[81] showed the advantage of using multiple time relaxation (MRT) technique for improved stability of the solution using the LBE-LES method. This methodology was further used for a coupled analysis using Lattice Boltzmann-Navier-Stokes by Feiz[82]. The present 3-D studies have incorporated corrections based on this prior work and extended for drag reduction studies for bluff bodies.

Many improvements have been made with regard to the implementation of boundary conditions [83]-[85], development of LBE methods for curvilinear boundaries [86][87], non-uniform mesh [88][89], irregular mesh [90] and grid refinement [91]. For further information on LBE, the reader is referred to the reviews by Benzi et al.[92], Chen and Doolen [93] and Yu et al [94].

Both LGA and LBM have been used in several applications, including hydrodynamics [95]-[98], flow through porous media [99][100], magneto-hydrodynamics [101][102], multiphase flow [103]-[106] and the reaction diffusion equation [107]-[109].

1.4 Coupling between lattice Boltzmann and Navier-Stokes equations

As mentioned earlier, to correctly model the physics of a multi-scale problem, it is necessary to couple the LBE and the NS equations. LBE is modeled close to the high Knudsen number region while NS is modeled away from it. Micro-flow phenomena and MEMS applications are some examples of multi-scale problems where LBE can be used [110][111]. LBE has also been used to simulate flow around synthetic jets [112][113]. However, for larger domains, like the Micro Blowing Technique (MBT) applications, it would be computationally expensive to use LBE throughout the domain. In this case, LBE and NS are required to be coupled, as shown by Feiz [82].

Such a coupled methodology for aerospace applications was first developed by Bourgat [114] and Tallec [115] for hypersonic rarefied flows around a space vehicle. Each of them used different method to data transfer between LBE and NS. Further, Crouseilles et al. [116] derived a hybrid scheme which integrates LBE and NS into one numerical scheme which could be used for multi-scale problems. Degond et al. [117] have shown that hybrid methods can be used to compute the unsteady shock wave produced by the diffraction of a plane moving shock wave that impinges upon a circular cylinder in a rarefied gas. More recently, Kolobov et al. [119] have demonstrated the capability of a Unified Flow Solver (UFS) to solve this coupled methodology using a Velocity Distribution Function (VDF) as the criteria to set the boundary condition at the interface. These methods need to be extended to aerodynamics applications like hub drag

reduction using AFC. This is the objective of the present research. The following chapter describes the details of the LBE method used in the present studies.

1.5 Research Objectives

The main objective of the present research is to develop a robust multi-scale modeling approach for two and three-dimensional flow control applications. In order to achieve this objective, firstly, benchmark simulations are performed to ensure that the model has temporal and spatial accuracy and conserves important quantities such as mass, momentum, energy, vorticity.

The model is then applied to a two-dimensional flow control problem and compared with experimental data. The multi-scale modeling methodology is further extended to three-dimensional flow control applications. Preliminary three-dimensional simulations are performed and analyzed to present the usefulness of the coupled methodology.

The present PhD thesis has been organized as follows. Chapter 2 details the numerical formulation of the Navier-Stokes equations used in the simulations presented in this thesis. The derivation of the Lattice Boltzmann equation starting from the Boltzmann equation is shown in Chapter 3.

Chapter 4 shows validations for several benchmark cases using the Lattice Boltzmann solver presented in the thesis. The multi-scale coupled methodology is demonstrated for a two-dimensional active flow control application in Chapter 5. This is followed by the preliminary results of the application of the coupled methodology for a three-dimensional active flow control problem in Chapter 6.

Derivation of the incompressible form of the Navier-Stokes equations from the Lattice Boltzmann equations using the Chapman Enskog derivation is documented in Appendix A. Prior to its use, the Navier-Stokes solver was extensively validated for flow control applications without the LBE interface. These applications are discussed in Appendix B. Additional validations for the Navier-Stokes solver alone are shown in Appendix C.

CHAPTER 2

NUMERICAL FORMULATION AND IMPLEMENTATION OF THE NAVIER-STOKES EQUATIONS

The present study uses an existing three-dimensional Navier-Stokes solver developed by Min [131][132] and couples it with an available open source software developed by Latt et al. [120]. This chapter details the numerical formulation involved in solving the Navier-Stokes equations.

2.1 Governing Equations

A three-dimensional compressible airflow solver, developed by Min [131][132] has been used as the Reynolds Averaged Navier-Stokes (RANS) solver for the coupled methodology presented in this thesis. The partial differential equation form of the three-dimensional Navier-Stokes (NS) equations in Cartesian co-ordinates is given as:

$$\frac{\partial Q}{\partial t}+\frac{\partial E}{\partial x}+\frac{\partial F}{\partial y}+\frac{\partial G}{\partial z}=\frac{\partial E_{\mathrm{v}}}{\partial x}+\frac{\partial F_{\mathrm{v}}}{\partial y}+\frac{\partial G_{\mathrm{v}}}{\partial z} \tag{2.1}$$

where Q is the flow vector, defined as:

$$Q=\begin{Bmatrix}\rho\\ \rho u\\ \rho \mathrm{v}\\ \rho w\\ e\end{Bmatrix} \tag{2.2}$$

Here, E, F and G are the inviscid flux vectors; $E_{\mathrm{v}}, F_{\mathrm{v}}$ and G_{v} are the viscous flux vectors, defined as:

$$E = \begin{Bmatrix} \rho \\ \rho u^2 + p \\ \rho u \mathrm{v} \\ \rho u w \\ u(e+p) \end{Bmatrix}, F = \begin{Bmatrix} \rho \\ \rho u \mathrm{v} \\ \rho \mathrm{v}^2 + p \\ \rho \mathrm{v} w \\ \mathrm{v}(e+p) \end{Bmatrix}, G = \begin{Bmatrix} \rho \\ \rho u w \\ \rho \mathrm{v} w \\ \rho w^2 \\ w(e+p) \end{Bmatrix} \tag{2.3}$$

$$E_v = \begin{Bmatrix} 0 \\ \tau_{xx} \\ \tau_{yx} \\ \tau_{zx} \\ E_x \end{Bmatrix}, F_v = \begin{Bmatrix} 0 \\ \tau_{xy} \\ \tau_{yy} \\ \tau_{zy} \\ E_y \end{Bmatrix}, G_v = \begin{Bmatrix} 0 \\ \tau_{xz} \\ \tau_{yz} \\ \tau_{zz} \\ E_z \end{Bmatrix} \tag{2.4}$$

The quantities, ρ, u, v, w are the flow density and the three Cartesian velocity components respectively. p is the static pressure, and e is the total energy per unit volume, defined as:

$$e = \frac{p}{\gamma - 1} + \frac{1}{2}\rho(u^2 + \mathrm{v}^2 + w^2) \tag{2.5}$$

The viscous stress terms are written as:

$$\begin{aligned} \tau_{xx} &= (\lambda + 2\mu)u_x + \lambda \mathrm{v}_y + \lambda w_z \\ \tau_{yy} &= \lambda u_x + (\lambda + 2\mu)\mathrm{v}_y + \lambda w_z \\ \tau_{zz} &= \lambda u_x + \lambda \mathrm{v}_y + (\lambda + 2\mu)w_z \\ \tau_{xy} &= \tau_{yx} = \mu\left(u_y + \mathrm{v}_x\right) \\ \tau_{xz} &= \tau_{zx} = \mu(u_z + w_x) \\ \tau_{yz} &= \tau_{zy} = \mu\left(\mathrm{v}_y + w_y\right) \end{aligned} \tag{2.6}$$

$$E_x = u\tau_{xx} + \mathrm{v}\tau_{xy} + w\tau_{xz} + k\frac{\partial T}{\partial x}$$

$$E_y = u\tau_{yx} + \mathrm{v}\tau_{yy} + w\tau_{yz} + k\frac{\partial T}{\partial y}$$

$$E_z = u\tau_{zx} + \mathrm{v}\tau_{zy} + w\tau_{zz} + k\frac{\partial T}{\partial z}$$

Here u_x, v_y, w_z, etc. are the velocity gradients. Using the Stokes hypothesis, the value λ is assumed to be related with molecular viscosity, μ, as:

$$\lambda = -\frac{2}{3}\mu \tag{2.7}$$

In turbulent flows, if an eddy viscosity model is used, the viscosity, $\upsilon(=\mu/\rho)$, is represented as the sum of the laminar viscosity and turbulent viscosity as shown below:

$$\upsilon = \upsilon_l + \upsilon_t \tag{2.8}$$

The laminar viscosity is estimated using Sutherland's law and the turbulent viscosity is estimated using turbulence models. Using the estimated viscosity, the thermal conductivity, k, is obtained as:

$$\frac{k}{\rho} = \frac{\upsilon_l C_p}{Pr} + \frac{\upsilon_t C_p}{Pr_t} \tag{2.9}$$

where C_p is the specific heat at constant pressure, Pr is the Prandtl number (≈ 0.72), and Pr_t is the turbulent Prandtl number (≈ 0.91).

2.2 Governing Equations in Generalized Co-ordinate System

There are two important steps involved in transforming the above Navier-Stokes equations from Cartesian co-ordinate system to a form which may be used in any generalized co-ordinate system. The first step is the non-dimensionalization of the

Navier-Stokes equations in order to remove the dependency of the solution on any given physical system of units. The second step is the transformation of the non-dimensionalized system of equations in Cartesian co-ordinates to a generalized co-ordinate system. Each of these steps is described below.

2.2.1 Non-dimensionalizing the governing equations

Non-dimensionalization is performed using reference values for length (L), density (ρ_∞), viscosity (μ_∞), pressure (p_∞) and speed of sound (a_∞). The reference Mach number (M_∞) and Reynolds number (Re_∞) are defined as follows:

$$M_\infty = \frac{V_\infty}{a_\infty}$$
$$Re_\infty = \frac{\rho_\infty V_\infty L}{\mu_\infty} \tag{2.10}$$

In the above equations, V_∞, is the free stream velocity. Using the non-dimensionalization below, the non-dimensionalized Navier-Stokes equations are obtained.

$$x^* = \frac{\hat{x}}{L} \qquad y^* = \frac{\hat{y}}{L} \qquad z^* = \frac{\hat{z}}{L} \qquad t^* = \frac{\hat{t}a_\infty}{L}$$

$$u^* = \frac{\hat{u}}{a_\infty} \qquad \mathrm{v}^* = \frac{\hat{\mathrm{v}}}{a_\infty} \qquad w^* = \frac{\hat{w}}{a_\infty} \qquad \rho^* = \frac{\hat{\rho}}{\rho_\infty}$$

$$p^* = \frac{\hat{p}}{\gamma p_\infty} \qquad \mu^* = \frac{\hat{\mu}}{\mu_\infty} \qquad e^* = \frac{\hat{e}}{\rho_\infty a_\infty^2}$$

2.2.2 Transformation to a Generalized Co-ordinate system

In order to generalize the above Cartesian form of the Navier-Stokes equations for curvilinear surfaces, co-ordinate transformation is performed and the Navier-Stokes equations in the generalized curvilinear system is obtained as:

$$\frac{\partial \bar{Q}}{\partial t}+\frac{\partial \bar{E}}{\partial \xi}+\frac{\partial \bar{F}}{\partial \eta}+\frac{\partial \bar{G}}{\partial \zeta}=\frac{\partial \bar{E}_{\mathrm{v}}}{\partial \xi}+\frac{\partial \bar{F}_{\mathrm{v}}}{\partial \eta}+\frac{\partial \bar{G}_{\mathrm{v}}}{\partial \zeta} \tag{2.11}$$

$$\bar{Q}=\frac{1}{J}\begin{Bmatrix}\rho\\ \rho u\\ \rho \mathrm{v}\\ \rho w\\ e\end{Bmatrix} \tag{2.12}$$

$$\bar{E}=\frac{1}{J}\begin{Bmatrix}\rho U\\ \rho uU+\xi_x p\\ \rho \mathrm{v}U+\xi_y p\\ \rho wU+\xi_z p\\ (e+p)U-\xi_t p\end{Bmatrix},\bar{F}=\frac{1}{J}\begin{Bmatrix}\rho V\\ \rho uV+\eta_x p\\ \rho \mathrm{v}V+\eta_y p\\ \rho wV+\eta_z p\\ (e+p)V-\eta_t p\end{Bmatrix},\bar{G}=\frac{1}{J}\begin{Bmatrix}\rho W\\ \rho uW+\zeta_x p\\ \rho \mathrm{v}W+\zeta_y p\\ \rho wW+\zeta_z p\\ (e+p)W-\zeta_t p\end{Bmatrix} \tag{2.13}$$

$$\bar{E}_{\mathrm{v}}=\frac{1}{J}\frac{M_\infty}{Re_\infty}\begin{Bmatrix}0\\ \xi_x\tau_{xx}+\xi_y\tau_{xy}+\xi_z\tau_{xz}\\ \xi_x\tau_{yx}+\xi_y\tau_{yy}+\xi_z\tau_{yz}\\ \xi_x\tau_{zx}+\xi_y\tau_{zy}+\xi_z\tau_{zz}\\ \xi_x E_x+\xi_y E_y+\xi_z E_z\end{Bmatrix},$$

$$\bar{F}_{\mathrm{v}}=\frac{1}{J}\frac{M_\infty}{Re_\infty}\begin{Bmatrix}0\\ \eta_x\tau_{xx}+\eta_y\tau_{xy}+\eta_z\tau_{xz}\\ \eta_x\tau_{yx}+\eta_y\tau_{yy}+\eta_z\tau_{yz}\\ \eta_x\tau_{zx}+\eta_y\tau_{zy}+\eta_z\tau_{zz}\\ \eta_x E_x+\eta_y E_y+\eta_z E_z\end{Bmatrix}, \tag{2.14}$$

$$\bar{G}_{\mathrm{v}}=\frac{1}{J}\frac{M_\infty}{Re_\infty}\begin{Bmatrix}0\\ \zeta_x\tau_{xx}+\zeta_y\tau_{xy}+\zeta_z\tau_{xz}\\ \zeta_x\tau_{yx}+\zeta_y\tau_{yy}+\zeta_z\tau_{yz}\\ \zeta_x\tau_{zx}+\zeta_y\tau_{zy}+\zeta_z\tau_{zz}\\ \zeta_x E_x+\zeta_y E_y+\zeta_z E_z\end{Bmatrix}$$

where the curvilinear co-ordinates (t,ξ,η,ζ) are related to the Cartesian co-ordinates (t,x,y,z) as:

$$\xi = \xi(x, y, z, t)$$
$$\eta = \eta(x, y, z, t) \tag{2.15}$$
$$\zeta = \zeta(x, y, z, t)$$

In the above equations, J is the Jacobian of the transformation, and U, V, W are the contravariant velocity components along the curvilinear co-ordinates computed as:

$$U = \xi_t + \xi_x u + \xi_y \mathrm{v} + \xi_z w$$
$$V = \eta_t + \eta_x u + \eta_y \mathrm{v} + \eta_z w \tag{2.16}$$
$$W = \zeta_t + \zeta_x u + \zeta_y \mathrm{v} + \zeta_z w$$

The quantities $\xi_t, \eta_t,$ and ζ_t are related to the grid velocities (x_t, y_t, z_t) in the physical domain as:

$$\xi_t = -x_t \xi_x - y_t \xi_y - z_t \xi_z$$
$$\eta_t = -x_t \eta_x - y_t \eta_y - z_t \eta_z \tag{2.17}$$
$$\zeta_t = -x_t \zeta_x - y_t \zeta_y - z_t \zeta_z$$

Here, $\xi_x, \xi_y, \xi_z,$ etc. are the computed metrics. For a more detailed description of the co-ordinate transformation, the reader is referred to Ref. [133].

2.3 Discretized Equations: Calculation of Inviscid and Viscous Fluxes

The discretized form of the governing equation, Eqn. (2.11), at a cell (i, j, k) may be written as follows using central differences:

$$\frac{\partial \bar{Q}_{i,j,k}}{\partial t} = -\left(\frac{\bar{E}_{i+\frac{1}{2},j,k} - \bar{E}_{i-\frac{1}{2},j,k}}{\Delta\xi} + \frac{\bar{F}_{i,j+\frac{1}{2},k} - \bar{F}_{i,j-\frac{1}{2},k}}{\Delta\eta} + \frac{\bar{G}_{i,j,k+\frac{1}{2}} - \bar{G}_{i,j,k-\frac{1}{2}}}{\Delta\zeta} \right) + \frac{\bar{E}_{\mathrm{v}_{i+\frac{1}{2},j,k}} - \bar{E}_{\mathrm{v}_{i-\frac{1}{2},j,k}}}{\Delta\xi} + \frac{\bar{F}_{\mathrm{v}_{i,j+\frac{1}{2},k}} - \bar{F}_{\mathrm{v}_{i,j-\frac{1}{2},k}}}{\Delta\eta} + \frac{\bar{G}_{\mathrm{v}_{i,j,k+\frac{1}{2}}} - \bar{G}_{\mathrm{v}_{i,j,k-\frac{1}{2}}}}{\Delta\zeta} \tag{2.18}$$

where, for convenience:

$$\Delta\xi = \xi_{i+\frac{1}{2},j,k} - \xi_{i-\frac{1}{2},j,k} = 1$$

$$\Delta\eta = \eta_{i,j+\frac{1}{2},k} - \eta_{i,j-\frac{1}{2},k} = 1 \tag{2.19}$$

$$\Delta\zeta = \zeta_{i,j,k+\frac{1}{2}} - \zeta_{i,j,k-\frac{1}{2}} = 1$$

Here, $\left(i \pm \frac{1}{2}, j \pm \frac{1}{2}, k \pm \frac{1}{2}\right)$ represents six faces of the cell. Using the central difference operator, δ, Eqn. (2.18) is re-written in following form:

$$\frac{\partial \bar{Q}_{i,j,k}}{\partial t} = -\left(\delta_\xi \bar{E} + \delta_\eta \bar{F} + \delta_\zeta \bar{G}\right) + \left(\delta_\xi \bar{E}_\mathrm{v} + \delta_\eta \bar{F}_\mathrm{v} + \delta_\zeta \bar{G}_\mathrm{v}\right) \tag{2.20}$$

Equation (2.20) is the final form of the governing equation before a numerical scheme is applied. The first term on the right-hand side represents the inviscid flux, and the second term represents viscous flux. Among the many numerical schemes proposed for the computation of the inviscid fluxes, i.e. $\bar{E}_{i\pm\frac{1}{2},j,k}, \bar{F}_{i,j\pm\frac{1}{2},k}, \bar{G}_{i,j,k\pm\frac{1}{2}}$, Roe's flux-difference splitting scheme [134] is used in the present study. Roe flux scheme has been chosen since this approximate linear solution to the Riemann problem was deemed sufficient for the present studies. At the i^{th} cell interface, taking into account the wave propagation direction, the numerical flux $\bar{E}$ is computed as:

$$\bar{E}_{i+\frac{1}{2}} = \frac{1}{2}\left\{\left(\bar{E}(q_L) + \bar{E}(q_R)\right) - \left|\tilde{A}\right|(q_R - q_L)\right\} \tag{2.21}$$

where $\tilde{A} = \frac{\partial \bar{E}}{\partial q}$ and q_R and q_L represent the flow vector on the right and left side of the cell face respectively, given by:

$$q_L = \begin{bmatrix} \rho_L \\ u_L \\ \mathrm{v}_L \\ w_L \\ p_L \end{bmatrix} \qquad\qquad q_R = \begin{bmatrix} \rho_R \\ u_R \\ \mathrm{v}_R \\ w_R \\ p_R \end{bmatrix}$$

Here, $\bar{E}(q_L)$ and $\bar{E}(q_R)$ are the fluxes calculated using the q_L and q_R flow vectors, as shown below:

$$\bar{E}_L = \begin{bmatrix} \rho_L U_L \\ \rho_L U_L u_L + p_L n_x \\ \rho_L U_L \mathrm{v}_L + p_L n_y \\ \rho_L U_L w_L + p_L n_z \\ \rho_L U_L h_{0L} - p_L n_t \end{bmatrix} \qquad\qquad \bar{E}_R = \begin{bmatrix} \rho_R U_R \\ \rho_R U_R u_R + p_R n_x \\ \rho_R U_R \mathrm{v}_R + p_R n_y \\ \rho_R U_R w_R + p_R n_z \\ \rho_R U_R h_{0R} - p_R n_t \end{bmatrix}$$

The quantities h_0, (n_x, n_y, n_z) and n_t are the specific total enthalpy ($h_0 = (e+p)/\rho$), surface normal vector, and the grid velocity in the surface normal direction, respectively. The accuracy of q_R and q_L, determines the spatial accuracy of the solution. In the present study, these values are calculated using the Monotone Upstream-centered Scheme for Conservation Laws (MUSCL) [135] reconstruction. This formulation is defined as:

$$\begin{aligned} q_L &= q_i + \phi^l \left[\frac{(1-k)}{4}(q_i - q_{i-1}) + \frac{(1+k)}{4}(q_{i+1} - q_i) \right] \\ q_R &= q_{i+1} - \phi^r \left[\frac{(1+k)}{4}(q_{i+1} - q_i) + \frac{(1-k)}{4}(q_{i+2} - q_{i+1}) \right] \end{aligned} \tag{2.22}$$

where

k = 1: 2nd order central difference,

k = 1/3 : 3rd order upwind scheme

The limiter function, ϕ, is introduced to maintain stability and to eliminate spurious numerical oscillations by reducing the order of accuracy in the regions where

large gradients and discontinuities exist. In the present study, van Albada flux limiter [136] is used to calculate this value:

$$\phi^l = \frac{2(q_i - q_{i-1})(q_{i+1} - q_i) + \varepsilon}{(q_i - q_{i-1})^2 + (q_{i+1} - q_i)^2 + \varepsilon}$$
$$\phi^r = \frac{2(q_{i+1} - q_i)(q_{i+2} - q_{i+1}) + \varepsilon}{(q_{i+1} - q_i)^2 + (q_{i+2} - q_{i+1})^2 + \varepsilon} \tag{2.23}$$

Here, ε is a small number (~ 10^{-20}) to prevent indeterminacy.

The second term in Eqn. (2.21), can be expressed using the Vinokur and Liu [137] formula as:

$$\left|\tilde{A}\right|(q_R - q_L) = \left|\tilde{\lambda}_1\right| \begin{Bmatrix} \Delta\rho \\ \Delta\rho u \\ \Delta\rho \mathrm{v} \\ \Delta\rho w \\ \Delta \mathrm{e} \end{Bmatrix} + \delta_1 \begin{Bmatrix} \tilde{\rho} \\ \tilde{\rho}\tilde{u} \\ \tilde{\rho}\tilde{\mathrm{v}} \\ \tilde{\rho}\tilde{w} \\ \tilde{\rho}\tilde{h}_0 \end{Bmatrix} + \delta_1 \begin{Bmatrix} 0 \\ n_x \\ n_y \\ n_z \\ \widetilde{U}_c \end{Bmatrix} \tag{2.24}$$

where:

$$\begin{aligned}
\delta_1 &= C_1 \frac{\Delta p}{\tilde{\rho}\tilde{a}^2} + 0.5 C_2 \frac{\Delta U_c}{\tilde{a}} \\
\delta_2 &= C_1 \tilde{\rho} \Delta U_c + 0.5 C_2 \frac{\Delta p}{\tilde{a}} \\
C_1 &= -\left|\tilde{\lambda}_1\right| + 0.5\left(\left|\tilde{\lambda}_2\right| + \left|\tilde{\lambda}_3\right|\right) \\
C_2 &= \left|\tilde{\lambda}_2\right| - \left|\tilde{\lambda}_3\right| \\
\tilde{\lambda}_1 &= \widetilde{U} \\
\tilde{\lambda}_2 &= \widetilde{U} + \tilde{a} \\
\tilde{\lambda}_3 &= \widetilde{U} - \tilde{a} \\
\widetilde{U} &= n_t + n_x \tilde{u} + n_y \tilde{\mathrm{v}} + n_z \tilde{w} \\
\widetilde{U}_c &= n_x \tilde{u} + n_y \tilde{\mathrm{v}} + n_z \tilde{w} \\
\Delta U_c &= U_c|_R - U_c|_L = n_x(u_R - u_L) + n_y(\mathrm{v}_R - \mathrm{v}_L) + n_z(w_R - w_L)
\end{aligned} \tag{2.25}$$

Here, the operator Δ is defined as $\Delta(\bullet) = (\bullet)|_R - (\bullet)|_L$. The quantities with the superscript '~' represent Roe-averaged values, and are defined for any flow variable $\emptyset$ except ρ as:

$$\tilde{\rho} = \sqrt{\rho_R \rho_L}$$

$$\tilde{\emptyset} = \emptyset_L \left(\frac{1}{1 + \sqrt{\rho_R / \rho_L}} \right) + \emptyset_R \left(\frac{\sqrt{\rho_R / \rho_L}}{1 + \sqrt{\rho_R / \rho_L}} \right) \tag{2.26}$$

The viscous fluxes $(\bar{E}_\mathrm{v}, \bar{F}_\mathrm{v}, \bar{G}_\mathrm{v})$ are computed using symmetric second order central difference scheme at the cell interface. The derivatives in Eqn. (2.14) are calculated using first order forward difference, as:

$$\emptyset_\xi \big|_{i+\frac{1}{2}} = \frac{\emptyset_{i+1} - \emptyset_i}{\Delta\xi} \qquad \emptyset_\xi \big|_{i-\frac{1}{2}} = \frac{\emptyset_i - \emptyset_{i-1}}{\Delta\xi} \tag{2.27}$$

2.4 Time Marching Scheme

The Lower-Upper Symmetric Gauss-Seidel (LU-SGS) implicit method is used for marching in time. Equation (2.20) can be written in an implicit formulation with first order backward differencing in time as:

$$\frac{1}{J}\frac{\Delta Q^{n+1}}{\Delta t} = -\left(\delta_\xi \bar{E}^{n+1} + \delta_\eta \bar{F}^{n+1} + \delta_\zeta \bar{G}^{n+1}\right) + \left(\delta_\xi \bar{E}_\mathrm{v}^{n} + \delta_\eta \bar{F}_\mathrm{v}^{n} + \delta_\zeta \bar{G}_\mathrm{v}^{n}\right) \tag{2.28}$$

Here, $\Delta Q^{n+1} = Q^{n+1} - Q^n$, the superscript n and n+1 represent time level. The viscous terms are treated explicitly with flow quantities at time level n. Note that the grid Jacobian, J, is treated as a constant over a time period since the cell volume is not changed for stationary grid. The inviscid flux terms are linearized using Taylor series expansion as follows:

$$\bar{E}^{n+1} \cong \bar{E}^n + [A^n]\Delta Q^{n+1}$$
$$\bar{F}^{n+1} \cong \bar{F}^n + [B^n]\Delta Q^{n+1} \tag{2.29}$$
$$\bar{G}^{n+1} \cong \bar{G}^n + [C^n]\Delta Q^{n+1}$$

Where the flux Jacobian matrices are defined as:

$$[A] = \frac{\partial \bar{E}}{\partial Q} \qquad [B] = \frac{\partial \bar{F}}{\partial Q} \qquad [C] = \frac{\partial \bar{G}}{\partial Q} \tag{2.30}$$

The detailed form of the Jacobian matrix may be written as given by Pulliam and Steger [138]:

$$[K] = \frac{1}{J}\begin{bmatrix} k_t & k_x & k_y & k_z & 0 \\ k_x\phi^2 - u\theta & \Theta - k_x\sigma_2 u & k_y u - \sigma k_x \mathrm{v} & k_z u - \sigma k_x w & \sigma k_x \\ k_y\phi^2 - \mathrm{v}\theta & k_x \mathrm{v} - \sigma k_y u & \Theta - k_x\sigma_2 \mathrm{v} & k_z \mathrm{v} - \sigma k_y w & \sigma k_y \\ k_z\phi^2 - w\theta & k_x w - \sigma k_z u & k_y w - \sigma k_z \mathrm{v} & \Theta - k_x\sigma_2 w & \sigma k_z \\ \theta(\phi^2 - E) & k_x E - \sigma u\theta & k_y E - \sigma \mathrm{v}\theta & k_z E - \sigma w\theta & k_t + \gamma\theta \end{bmatrix} \tag{2.31}$$

Where:

$$\begin{aligned} \phi^2 &= (\gamma - 1)\,(u^2 + \mathrm{v}^2 + w^2)/2 \\ \theta &= k_x u + k_y \mathrm{v} + k_z w \\ \sigma &= \gamma - 1 \\ \sigma_2 &= \gamma - 2 \\ \Theta &= k_t + \theta \\ E &= \frac{\gamma e}{\rho} - \phi^2 \end{aligned} \tag{2.32}$$

The matrix $[K]$ is $[A]$ or $[B]$ or $[C]$ when the k is chosen as ξ or η or ζ. With Eqn. (2.29), Eqn. (2.28) may be re-arranged as:

$$\left[I + J\Delta t\left(\delta_\xi A^n + \delta_\eta B^n + \delta_\zeta C^n\right)\right]\Delta Q^{n+1} = (RHS)^n \tag{2.33}$$

Where I is the identity matrix and the right-hand side term, (RHS), is sometimes referred as the residual.

$$(RHS)^n = -J\Delta t\left(\delta_\xi \bar{E}^n + \delta_\eta \bar{F}^n + \delta_\zeta \bar{G}^n\right) + J\Delta t\left(\delta_\xi \bar{E}_\mathrm{v}^n + \delta_\eta \bar{F}_\mathrm{v}^n + \delta_\zeta \bar{G}_\mathrm{v}^n\right) \tag{2.34}$$

Equation (2.33) is a matrix system, which is computationally very expensive to invert. To reduce the computational time, the matrix inside the bracket on the left-hand side is approximately factored using a Lower-Upper Symmetric Gauss-Seidel (LU-SGS) implicit method proposed by Yoon and Jameson [139]. In the LU-SGS scheme, Eqn. (2.33) is expressed as:

$$(L + D + U)\Delta Q^{n+1} = (RHS)^n \tag{2.35}$$

Where L is a lower block triangular matrix with null matrices on the diagonal, D is a block diagonal matrix and U is an upper block triangular matrix with null matrices on the diagonal. For the case of non-singular matrix D, Eqn. (2.35) may be re-written as:

$$D(D^{-1}L + I + D^{-1}U)\Delta Q^{n+1} = (RHS)^n \tag{2.36}$$

Using LU-factorization, Eqn. (2.36) may be approximated as:

$$D(I + D^{-1}L)(I + D^{-1}U)\Delta Q^{n+1} = (RHS)^n \tag{2.37}$$

Or

$$(D + L)D^{-1}(D + U)\Delta Q^{n+1} = (RHS)^n \tag{2.38}$$

Where:

$$\begin{aligned}
(D + L) &= I - J\Delta t\left(\frac{A^-}{\Delta\xi} - \delta_\xi^- A^+ + \frac{B^-}{\Delta\eta} - \delta_\eta^- B^+ + \frac{C^-}{\Delta\zeta} - \delta_\zeta^- C^+\right) \\
D &= I + J\frac{\Delta t}{\Delta\xi}(A^+ - A^-) + J\frac{\Delta t}{\Delta\eta}(B^+ - B^-) + J\frac{\Delta t}{\Delta\zeta}(C^+ - C^-) \\
(D + U) &= I + J\Delta t\left(\frac{A^+}{\Delta\xi} + \delta_\xi^+ A^- + \frac{B^+}{\Delta\eta} + \delta_\eta^+ B^- + \frac{C^+}{\Delta\zeta} + \delta_\zeta^+ C^-\right)
\end{aligned} \tag{2.39}$$

The operator $\delta_\xi^-, \delta_\eta^-$ and δ_ζ^- are the first-order backward differences, while $\delta_\xi^+, \delta_\eta^+$ and δ_ζ^+ are the first-order forward differences. The matrices $A^\pm, B^\pm$ and $C^\pm$ are the

decomposed matrices based on the eigenvalues and eigenvectors. However, directly computing them is computationally expensive, and an approximated approach proposed by Yoon and Jameson [139] is used in the present study.

$$\begin{aligned} A^{\pm} &= \frac{1}{2}(A \pm r_A I) & r_A &= k_A max(|\lambda_A|) \\ B^{\pm} &= \frac{1}{2}(B \pm r_B I) & r_B &= k_B max(|\lambda_B|) \\ C^{\pm} &= \frac{1}{2}(C \pm r_C I) & r_C &= k_C max(|\lambda_C|) \end{aligned} \tag{2.40}$$

Here, λ_A, λ_B and λ_C are the eigenvalues of the matrices A, B and C, respectively. The constants k_A, k_B and k_C are user-input quantities (≥ 1) to enhance stability by increasing diagonal dominance of the system of equations. However, if the values are greater than 1, the convergence ratio is reduced. In the present study, $k_A = k_B = k_C = 1$ is used. The maximum eigenvalues may be evaluated as follows:

$$\begin{aligned} max(|\lambda_A|) &= |U| + a\left(\xi_x^2 + \xi_y^2 + \xi_z^2\right)^{\frac{1}{2}} \\ max(|\lambda_B|) &= |V| + a\left(\eta_x^2 + \eta_y^2 + \eta_z^2\right)^{\frac{1}{2}} \\ max(|\lambda_C|) &= |W| + a\left(\zeta_x^2 + \zeta_y^2 + \zeta_z^2\right)^{\frac{1}{2}} \end{aligned} \tag{2.41}$$

Using Eqn. (2.39), (2.40) and (2.41), Eqn. (2.38) is sequentially solved as shown below:

$$\begin{aligned} (D + L)\Delta Q^{**} &= (RHS)^n \\ D^{-1}\Delta Q^{*} &= \Delta Q^{**} \\ (D + U)\Delta Q^{n+1} &= \Delta Q^{*} \end{aligned} \tag{2.42}$$

The matrices on the left-hand side of Eqn. (2.42) have either lower, diagonal, or upper part only with all others zero. Thus, inversion of each matrix is easily

accomplished by backward or forward substitution. Once ΔQ^{n+1} is obtained, the new Q^{n+1} is computed from $Q^{n+1} = Q^n + \Delta Q^{n+1}$.

2.5 Turbulence Modeling

The shear stress terms, τ_{ij}, in the Eq. (2.14) is composed of viscous stress and Reynolds stress components. An eddy viscosity model is used and the Reynolds stress term is defined as $-\overline{u_i' u_j'} = 2\upsilon_t S_{ij}$. Thus, the viscosity in the Eq. (2.14) is the sum of molecular viscosity and eddy viscosity as shown below:

$$\upsilon = \upsilon_l + \upsilon_t \tag{2.43}$$

The eddy viscosity in the present study is estimated using the one-equation Spalart and Allmaras (SA) transport model [140]. The SA turbulence model was chosen from the many other models available in present NS solver, since it was found to be sufficient to resolve the flow field in the turbulent cases considered. In this model, the eddy viscosity, υ_t, is computed from:

$$\upsilon_t = \tilde{\nu} f_{\nu 1} \tag{2.44}$$

Where the viscous damping function, $f_{\nu 1}$, is given by:

$$f_{\nu 1} = \frac{\chi^3}{\chi^3 + c_{\nu 1}^3} \quad \text{and} \quad \chi = \frac{\tilde{\nu}}{\nu} \tag{2.45}$$

The damping function goes to zero at the wall and gradually rises to unity as the distance from the wall increases. The operating parameter $\tilde{\boldsymbol{\nu}}$ is determined by the transport equation as follows:

$$\begin{aligned} \frac{D\tilde{\nu}}{Dt} = c_{b1}[1 - f_{t2}]\tilde{S}\tilde{\nu} + \frac{1}{\sigma}\left[\nabla \cdot \left((\nu + \tilde{\nu})\nabla\tilde{\nu}\right) + c_{b2}(\nabla\tilde{\nu})^2\right] \\ - \left[c_{w1} f_w - \frac{c_{b1}}{\kappa^2} f_{t2}\right]\left[\frac{\tilde{\nu}}{d}\right]^2 + f_{t1}\Delta U^2 \end{aligned} \tag{2.46}$$

On the right hand-side, each term represents production, diffusion, dissipation, and trasition/trip effects, respectively. The individual components are defined as:

$$\tilde{S} = S + \frac{\tilde{\nu}}{\kappa^2 d^2} f_{v2} \qquad f_{v2} = 1 - \frac{\chi}{1 + \chi f_{v1}}$$

$$f_w = g\left[\frac{1 + c_{w3}^6}{g^6 + c_{w3}^6}\right]^{\frac{1}{6}} \qquad g = r + c_{w2}(r^6 - r) \tag{2.47}$$

$$r = \frac{\tilde{\nu}}{\tilde{S}\kappa^2 d^2} \qquad f_{t2} = c_{t3} exp(-c_{t4}\chi^2)$$

$$f_{t1} = c_{t1} g_t exp\left(-c_{t2}\frac{\omega_t^2}{\Delta U^2}[d^2 + g_t^2 d_t^2]\right)$$

Where:

d_t is the distance from the field point to the trip point on the wall

ω_t is the wall vorticity at the trip

ΔU is the difference between velocity at the field point and that at the trip

$g_t \equiv min(0.1, \Delta U/\omega_t \Delta x_t)$

x_t is the grid spacing along the wall at the

And, the constants are:

$c_{b1} = 0.1355$ $\quad c_{b2} = 0.622$ $\quad \sigma = 2/3$ $\quad \kappa = 0.41$

$c_{w1} = \frac{c_{b1}}{\kappa^2} + \frac{(1 + c_{b2})}{\sigma}$ $\quad c_{w2} = 0.3$ $\quad c_{w3} = 2$ $\quad c_{v1} = 7.1$

$c_{t1} = 1$ $\quad c_{t2} = 2$ $\quad c_{t3} = 1.2$ $\quad c_{t4} = 0.5$

In the current study, the trip is not applied and the flow field is assumed as full turbulent flows.

2.6 Initial Conditions

In the beginning of the analysis, flow properties in the Navier-Stokes domain were initialized with free stream properties as:

$$\begin{aligned} \rho &= \rho_\infty \\ u &= u_\infty \\ \mathrm{v} &= \mathrm{v}_\infty \\ w &= w_\infty \\ p &= p_\infty \end{aligned} \tag{2.48}$$

2.7 Boundary Conditions

At solid walls, no-slip adiabatic wall temperature condition was applied. For this the following condition is satisfied.

$$\begin{aligned} \vec{V}_{wall} &= \vec{V}_{grid} \\ \left.\frac{\partial T}{\partial n}\right|_{wall} &= 0 \end{aligned} \tag{2.49}$$

Zero gradient of pressure at the wall was also assumed, i.e. $(\partial p/\partial n|_{wall} = 0)$.

At the block interfaces including wake-cut behind trailing edge, ghost cell was used to maintain the solution accuracy. Ghost cells are non-existent grid points whose flow variables assist in maintaining solution continuity between different blocks of the grid. The properties of the ghost cell were obtained from inner cell value of the opposite block. Two consecutive ghost cell properties are required for third order scheme, and four ghost cell values are required for 7^{th} order scheme. For node-centered scheme, the flow properties at the interface were obtained by interpolating the fist inner cell value of the current block and the ghost cell value next to the interface.

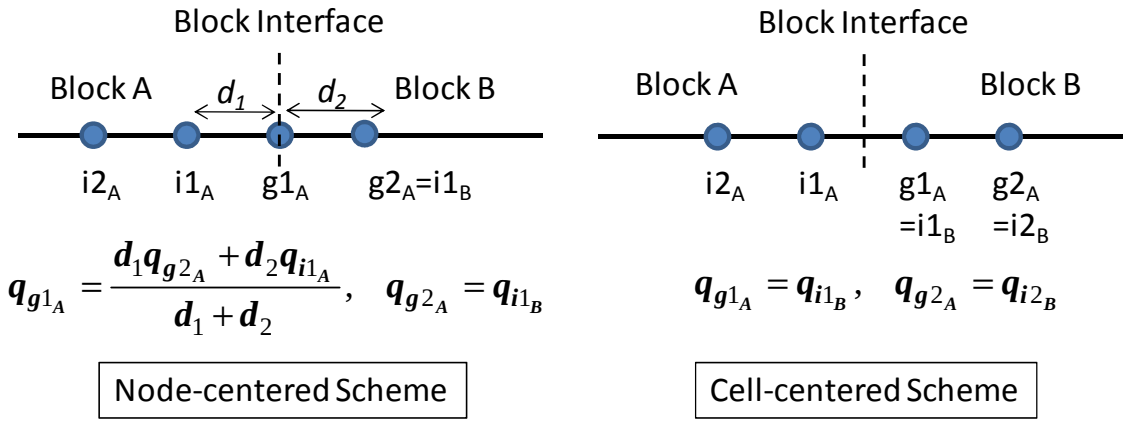

Figure 2.1: Interface boundary condition

At the outer boundaries including far-field, inboard, and outboard surfaces, characteristics based inflow/outflow boundary condition was applied to prevent non-physical wave reflection at the boundary. The details of this boundary condition may be found in classical CFD texts [141]. In this boundary condition, Riemann invariants are written as:

$$R^+ = \vec{V}_n + \frac{2a}{\gamma - 1}$$
$$R^- = \vec{V}_n - \frac{2a}{\gamma - 1} \tag{2.50}$$

And the characteristic velocities are:

$$\lambda_1 = \vec{V}_n + a$$
$$\lambda_2 = \vec{V}_n - a \tag{2.51}$$

Here, $\vec{V}_n$ is the normal velocity directing outward from the computational domain. If $\vec{V}_n$ is a negative value, so is λ_2, inflow condition is applied. In this case, if the value of λ_1 is also negative, all the information comes from the free stream. If λ_1 value is positive, one piece of information comes from the interior and others come from the free stream.

If $\vec{V_n}$ is a positive value, so is λ_1, outflow condition is applied. In such a case, if the value of λ_2 is positive, all the information comes from the interior. If the value of λ_2 is negative, one piece of information comes from the free stream and others come from the interior of the domain. Detailed computation of flow properties may be found in reference [141].

CHAPTER 3

NUMERICAL FORMULATION AND IMPLEMENTATION OF THE LATTICE BOLTZMANN EQUATION

The Lattice Boltzmann Equation (LBE) method simulates a flow system by tracking the evolution of particle distributions instead of tracking particles as in the case of Lattice Gas Automata (LGA). It also differs from the traditional computational fluid dynamics (CFD) methods in that it does not directly solve for macroscopic variables which appear in the Navier-Stokes (NS) equations. LBE recovers the Navier-Stokes equations using the Chapman-Enskog expansion [65][66].

Solving LBE has the following advantages over Navier-Stokes equations: (a) the convection operator in LBE is linear which is much faster and easier to compute than the non-linear advection term in the Navier-Stokes equations, (b) the Poisson equation for pressure, which is difficult to solve, is not solved in LBE since the macroscopic properties of the flow field are not directly calculated, (c) the macroscopic properties of the flow are obtained by simple arithmetic integration of microscopic properties in LBE and are therefore easier to implement.

3.1 Boltzmann Equation

The Boltzmann equation is part of the classical statistical physics, and describes the behavior of a gas on the microscopic scale. The kinetic theory of gases deals with the description of gas states on the molecular level. It introduces a function to describe the state of the gas by considering the position and velocity of each molecule in the gas. In a three-dimensional space, the velocity and position of a molecule at a point A can be

described by the six values $(x_1, x_2, x_3, \xi_x, \xi_y, \xi_z)$, where $(x_1, x_2, x_3) = \vec{x}$ is the position, and $(\xi_x, \xi_y, \xi_z) = \vec{\xi}$ is the velocity of the molecule. For a gas with N molecules, the state of the molecules can be described by N points with six values representing each molecule. For a typical gas with order of 10^{19} molecules per cubic centimeter, this level of detail is computationally expensive to model. Therefore, the density of the gas is used as a defining parameter for a volume of gas. Let dN be the number of points in this volume, then

$$f(\vec{x}, \vec{\xi}) = \frac{dN}{d\vec{x}, d\vec{\xi}} \tag{3.1}$$

where f is the molecular velocity distribution function. Integrating this function over all possible values for position and velocity would yield N, the total number of molecules. This function is a fundamental quantity in the Boltzmann equation. The following three approximations are made in deriving the Boltzmann equation:

1. Particle collisions are only considered between two particles. In this form it restricts the equation to diluted gases, where it can be assumed that in each collision only two particles are involved.
2. The particles are point-like and structureless. Therefore, it is assumed that their velocities are not correlated before and after the collision.
3. The third approximation is that the collision dynamics are instantaneous and not influenced by an external force (which is equivalent to a short-range potential for the interaction).

The second and third assumptions are made since the influence of a particle on another particle is negligible except when they collide and their regions of influence

touch each other. This collision process between two particles is considered instantaneous, and as such not affected by any external forces.

Including an external force g, the Boltzmann equation for f may be written as:

$$\frac{\partial f}{\partial t} + \vec{\xi} \cdot \frac{\partial f}{\partial \vec{x}} + \vec{g} \cdot \frac{\partial f}{\partial \vec{\xi}} = \Omega(f) \tag{3.2}$$

where the left hand side describes the overall motion of the molecules with the microscopic velocity $\vec{\xi}$ through the force field that is given by $\vec{g}$ at $\vec{x}$, while the right hand side models the interaction of molecules with the collision operator Ω. It is an integral equation that includes the differential collision cross section σ for the two particles. This operator σ may be calculated geometrically by approximating the molecules with rigid spheres for the collision. The incoming particle velocity is transformed into the outgoing velocity, and as such, the equation represents the link to the underlying molecular dynamics. Ω for two particles with the subscripts 1 and 2 may be written as:

$$\Omega(f) = \int (f_1' f_2' - f_1 f_2) \sigma(|\overrightarrow{u_1} - \overrightarrow{u_2}|, \vec{\omega})\, d\vec{\omega} d\overrightarrow{x_2} \tag{3.3}$$

where $\vec{\omega}$ denotes the solid angle over which is integrated and around which collisions are considered, respectively. As can be seen in Equation (3.3), the cross section σ is calculated with the solid angle of the collision and the relative speed of the two particles $|\overrightarrow{u_1} - \overrightarrow{u_2}|$. This equation furthermore includes Boltzmann's closure assumption, that leads to the aforementioned assumptions of a diluted gas with very localized, short-range interactions of the molecules:

$$f_{12} = f_1 f_2 \tag{3.4}$$

Using the BBGKY hierarchy (Bogoliubov, Born, Green, Kirkwood and Yvon [144]) an approximation for f_N may be calculated, which may subsequently be truncated to get an equation for f_{12}.

In the H-theorem (named after the function H(t), see below), Boltzmann showed in 1872, that the quantity

$$H(t) = -\int f ln(f) d\vec{\xi}\, d\vec{x} \tag{3.5}$$

obeys

$$\frac{dH}{dt} \geq 0 \tag{3.6}$$

Here $f\left(\vec{x}, \vec{\xi}, t\right)$ is any function that fulfills the Boltzmann equation. The equality sign in Equation (3.6) only holds when f is a Maxwell distribution (see Equation (3.9) below). Equation (3.6) may be imagined as a quantitative measure for the irreversibility from thermo-dynamics, whereas the H-theorem states that it is a monotonically increasing function in time. The evolution of the system only stops when the system has reached its global equilibrium with a maximal entropy H.

Due to the complicated nature of the collision operator Ω, it is often replaced by simpler expressions that still preserve the collision invariants [145] and, as stated in the H-theorem, tend towards a Maxwellian distribution. The standard model for this is the BGK approximation [70]:

$$\Omega_{BGK}(f) = \frac{f^{eq} - f}{\tau} \tag{3.7}$$

Here f^{eq} is a Maxwellian distribution representing the local equilibrium that is parameterized by the conserved quantities density ρ, speed $\vec{\xi}$ and temperature T. Each

collision changes the distribution function f_1 proportional to the departure from the local equilibrium f^{eq}, where the amount of this correction is modified by the relaxation time τ. The typical collision time τ is a function of the properties of the gas and its current state. In the BGK approximation τ is simplified as a single constant value chosen based on the criteria described in the following sections of this chapter.

The local equilibrium is reached when $\Omega(f^{eq}, f^{eq})$ vanishes. With this property it can be shown that f is a collision invariant, and as such does not change under the effect of a collision. The density ρ, momentum ξ_a and energy E are the Lagrangian parameters. Assuming a normalized particle mass of 1, they can be computed in the following way:

$$\begin{aligned} \int f d\vec{\xi} &= \rho \\ \int f u_a d\vec{\xi} &= \rho \xi_a \\ \int f \frac{u^2}{2} d\vec{\xi} &= \rho E \end{aligned} \tag{3.8}$$

The macroscopic flow speed ξ_a, density ρ and fluid temperature T parameterize the Maxwell distribution (sometimes also called Maxwell-Boltzmann distribution). For three dimensions it is:

$$f^M = \rho \left(\frac{m^2}{2\pi RT} \right)^{3/2} e^{\frac{-\left(\vec{\xi}-\vec{u}\right)^2 m^2}{2RT}} \tag{3.9}$$

where R is the Boltzmann constant, and m the mass of a particle.

3.2 Derivation of the Lattice Boltzmann equation

This section explains the derivation of the Lattice Boltzmann equation from the continuous Boltzmann equation based on the description in Refs. [73][146], starting from

an arbitrary kinetic equation. The next section details the derivation of the Navier-Stokes equations from the Lattice Boltzmann equation using the Chapman-Enskog expansion. Abbreviations for f and g are used as: $f(\vec{x},\vec{\xi},t) = f(t)$ and $f(\vec{x}+\vec{\xi}a,\vec{\xi},t+a) = f(t+a)$.

The Boltzmann equation with the BGK collision approximation is used as the starting point:

$$\frac{\partial f(t)}{\partial t} + \vec{\xi}\nabla f(t) = -\frac{1}{\lambda}\big(f(t) - g(t)\big) \tag{3.10}$$

where f is the particle distribution function at time *t*, position $\vec{x}$ for the microscopic velocity $\vec{\xi}$. $1/\lambda = A \cdot n$ is the relaxation time for the collision, that is calculated from the number of particles *n* and the proportional coefficient *A*. Here, the collision term has been linearized according to Equation (3.7), for simplicity, without loss of generality. *g* is the Maxwell distribution f^M from Equation (3.9).

The hydrodynamic properties of the fluid, the density ρ, velocity $\vec{u}$ and the temperature *T* can be calculated with the moments of the function *f*. Here, the energy ϵ from the energy density $\rho\epsilon$ can be used to determine the temperature of the fluid.

$$\begin{aligned} \rho &= \int f(\vec{x},\vec{\xi},t)d\vec{\xi} \\ \rho\vec{u} &= \int \xi f(\vec{x},\vec{\xi},t)d\vec{\xi} \\ \rho\epsilon &= \int \frac{1}{2}(\vec{\xi}-\vec{u})(\vec{x},\vec{\xi},t)d\vec{\xi} \end{aligned} \tag{3.11}$$

Note that the equilibrium distribution function g is calculated with these hydrodynamic moments, although it is written as a function of time and velocity. Hence, these values have to be correctly approximated after discretization.

Equation (3.10) can be formulated as an ordinary differential equation (ODE):

$$\frac{Df}{Dt} + \frac{1}{\lambda} f = \frac{1}{\lambda} g \tag{3.12}$$

where

$$\frac{D}{Dt} = \frac{\partial}{\partial t} + \vec{\xi}\nabla \tag{3.13}$$

is the time derivative along the microscopic velocity. Equation (3.12) is a linear ODE of first order, therefore, using a standard formula to solve this type of equation, solutions can be found with:

$$f(t + \delta_t) = f(t) \cdot e^{-\frac{\delta_t}{\lambda}} + \frac{1}{\lambda} e^{-\frac{\delta_t}{\lambda}} \cdot \int_0^{\delta_t} e^{\frac{t'}{\lambda}} g(t + t') dt' \tag{3.14}$$

Assuming that δ_t is very small and g is a smooth function, $g(t + t')$ can be approximated with linear interpolation for $0 \leq t' \leq \delta_t$. Furthermore, $e^{-\frac{\delta_t}{\lambda}}$ can be Taylor expanded in δ_t to the first order and equation (3.14) can be simplified to:

$$f(t + \delta_t) - f(t) = -\frac{\delta_t}{\lambda}\big(f(t) - g(t)\big) \tag{3.15}$$

Here, the relaxation time $\frac{\delta_t}{\lambda}$, is usually written as $\frac{1}{\tau}$.

The Maxwell distribution that is used as the equilibrium distribution function g is defined in equation (3.9). For a particle mass of 1 and D dimensions, it can be written as:

$$g(\vec{u}) = \frac{\rho}{(2\pi RT)^{D/2}} e^{-\frac{\left(\vec{\xi} - \vec{u}\right)^2}{2RT}} \tag{3.16}$$

This function is Taylor expanded in $\vec{u}$ upto the third order, which is a good approximation for small velocities. Expanding the quadratic form in the exponent of *e* and Taylor expanding the results yields the following equation:

$$g(0+\vec{u}) = \beta \cdot \left(1 + \frac{\vec{\xi}\cdot\vec{u}}{RT} + \frac{\left(\vec{\xi}\cdot\vec{u}\right)^2}{2(RT)^2} - \frac{\vec{u}^2}{2RT}\right) \tag{3.17}$$

where $\beta = \frac{\rho}{(2\pi RT)^{D/2}} e^{-\frac{\vec{\xi}^2}{2RT}}$. The following formula will be used as the local equilibrium distribution for the following derivations:

$$f^{(eq)} = \frac{\rho}{(2\pi RT)^{D/2}} e^{-\frac{\vec{\xi}^2}{2RT}} \left(1 + \frac{\vec{\xi}\cdot\vec{u}}{RT} + \frac{\left(\vec{\xi}\cdot\vec{u}\right)^2}{2(RT)^2} - \frac{\vec{u}^2}{2RT}\right) \tag{3.18}$$

The above equation gives the equilibrium distribution function along infinitely many velocity directions. Computers can however only handle a finite amount of variables, and represent them with a finite accuracy. Therefore, the infinite space of equation (3.18) must be replaced by a finite set of scalar values that are appropriate for the numerical investigation of the problem. This step is called the *space discretization* of the problem. The moments of the particle distribution functions are important for the consistency with the Navier-Stokes equations. Another important property that has to be retained by the discretization is the isotropy, which is the most important of the Navier-Stokes symmetries. Therefore the lattice should be invariant to rotations of the problem – this can be shown by isotropy-tensors as in Ref. [145]. But for the LBM derivation, the moments are directly used as constraint for the numerical integration method. The following discretization is done for the two-dimensional, nine-velocity (D2Q9) model of LBM. The use of the nine-velocity model instead of the simpler five-velocity model comes from the consideration of lattice symmetry; the LBE cannot recover the correct

Navier-Stokes equations unless sufficient lattice symmetry is guaranteed as described in reference [57].

For accurate results, the integrations of the second moment still have to be correct for models that include the temperature. As an isothermal model will be used, only the first moment, the velocity, will be required. The moments of Equation (3.18) in two dimensions can generally be written as follows:

$$I = \int \psi(\vec{\xi}) f^{(0)} d\vec{\xi}$$

$$= \frac{\rho}{(2\pi RT)^{D/2}} \int \psi(\vec{\xi}) e^{-\frac{\vec{\xi}^2}{2RT}} \left(1 + \frac{\vec{\xi} \cdot \vec{u}}{RT} + \frac{(\vec{\xi} \cdot \vec{u})^2}{2(RT)^2} - \frac{\vec{u}^2}{2RT} \right) d\vec{\xi} \tag{3.19}$$

where ψ is the moment function, that contains powers of the velocity components

$$\psi(\vec{\xi}) = \xi_x^m \xi_y^n \tag{3.20}$$

This is necessary, as the moments equation above also contains powers of the velocity in the parentheses to the right. After restructuring of the equation, moments of up to the third order will occur in the equation - one from the velocity moment, and two from the $(\vec{\xi} \cdot \vec{u})^2$ term. Ψ is replaced by its components in equation (3.20), $\vec{\xi}$ and $\vec{u}$ are replaced with their scalar x and y components in this two-dimensional derivation. Substituting these in equation (3.19) and simplifying, we obtain the following equation:

$$I = \frac{\rho}{\pi} \left(\sqrt{2RT}\right)^{m+n-2} \left[\left(1 - \frac{\vec{u}^2}{(2RT)} \right) I_x^m I_y^n + \frac{2\left(u_x I_x^{m+1} I_y^n + u_y I_x^m I_y^{n+1}\right)}{\left(\sqrt{2RT}\right)} + \frac{u_x^2 I_x^{m+2} I_y^n + 2u_x u_y I_x^{m+1} I_y^{n+1} + u_y^2 I_x^m I_y^{n+2}}{RT} \right] \tag{3.21}$$

where I_i^m is the m-th moment of the function $e^{-\zeta^2}$, given by:

$$I_i^m = \int e^{-\zeta_i^2} \zeta_i^m d\zeta_i \tag{3.22}$$

The crucial step for the derivation of the LBM is to use the proper quadrature formula to numerically integrate these moments. The quadrature works in the following way:

$$\int f(x)W(x)dx = \sum_{j=1}^{N} w_j f(x_j) \tag{3.23}$$

where W(x) is the weighting function, e^{-x^2} in this case, and f(x) is a polynomial in x, e.g. $f(\zeta_x) = \zeta_x^m$. The integral over the multiplication of these two functions is approximated by the sum over function evaluations at the values x = x_j with the weights w_j. The values x_i are also called abscissas. In total, there are N abscissas and weights. For the integration of functions like $e^{-\zeta^2}$ a Gauss-Hermite quadrature can be applied, which is correct for W-polynomials up to the order (2N −1). The order of the Gauss-Hermite quadrature has to be chosen according to the order of the moment-polynomial ψ. Since the model is isothermal, the energy due to the temperature is be kept constant. Therefore, there is no additional level of freedom for the temperature, but for the moment integration it has to be considered. Therefore, for a ψ of second order, and second order terms in the $(\vec{\xi} \cdot \vec{u})$ term, moments of up to fourth order have to be integrated correctly. This requires a Gauss-Hermite quadrature of third order (N = 3):

$$I_i^m = \sum_{j=1}^{3} w_j (\zeta_j)^m \tag{3.24}$$

with the following weights and abscissas:

$$\zeta_1 = -\sqrt{3/2}\,, \zeta_2 = 0, \zeta_3 = +\sqrt{3/2} \tag{3.25}$$

$$w_1 = \frac{\sqrt{\pi}}{6}, w_2 = \frac{2\sqrt{\pi}}{3}, w_3 = \frac{\sqrt{\pi}}{6}$$

After applying the Gauss-Hermite quadrature, the moment function may be written as:

$$I = \frac{\rho}{\pi}\sum_{i=1}^{3}\sum_{j=1}^{3} w_i w_j \psi(\zeta_{i,j})\left(1 + \frac{\vec{\xi}\cdot\vec{u}}{RT} + \frac{(\vec{\xi}\cdot\vec{u})^2}{2(RT)^2} - \frac{\vec{u}^2}{2RT}\right) \tag{3.26}$$

where $\zeta_{i,j}$ is the vector given by the quadrature abscissas $\zeta_{i,j} = (\sqrt{2RT})(\zeta_i, \zeta_j)^T$. As the two sums run over three values for i and j each, there are a total of nine possible values for $\zeta_{i,j}$ and $w_i w_j$. For these a new single index will be introduced. Furthermore, a number of substitutions can be made. As an isothermal model is used, the temperature T has no physical relevance, and can be replaced by a constant $c = \sqrt{3RT}$. The speed of sound $c_s = 1/\sqrt{3}$ in the model yields $c_s^2 = c^2/3 = RT$. The weights, divided by π read:

$$\begin{gathered} w_0 = w_2 w_2 = 4/9 \\ w_{1..4} = w_1 w_2, w_2 w_1, w_3 w_2, w_2 w_3 = 1/9 \\ w_{5..8} = w_1 w_3, w_3 w_1, w_1 w_1, w_3 w_3 = 1/36 \end{gathered} \tag{3.27}$$

Each component of the vectors $\zeta_{i,j}$ is either 0 or $\pm\sqrt{RT}\sqrt{3/2} = \pm\sqrt{3RT} = c$:

$$\begin{gathered} \vec{e}_0 = \zeta_{1,1} = (0,0)^T \\ \vec{e}_{1..4} = \zeta_{1,2}, \zeta_{2,1}, \zeta_{3,2}, \zeta_{2,3} = (\pm 1, 0)^T c, (0, \pm 1)^T c \\ \vec{e}_{5..8} = \zeta_{1,3}, \zeta_{3,1}, \zeta_{1,1}, \zeta_{3,3} = (\pm 1, \pm 1)^T c \end{gathered} \tag{3.28}$$

With these discrete velocities, equation (3.26) reads:

$$I = \sum_{\alpha=1}^{9} W_\alpha \psi(\vec{e}_\alpha) f_\alpha^{eq} \tag{3.29}$$

Here W_α can be identified as $2\pi RT e^{\frac{\vec{\xi}^2}{2RT}}$. This yields the known form of the equilibrium distribution function for each of the nine velocities:

$$f_\alpha^{eq} = w_\alpha \rho \left(1 + \frac{3\vec{e}\cdot\vec{u}}{c^2} + \frac{9(\vec{e}\cdot\vec{u})^2}{2c^4} - \frac{3\vec{u}^2}{2c^2}\right) \tag{3.30}$$

Note that the lattice velocity vectors were given by the chosen Gauss-Hermite quadrature. The configuration of the lattice was in this case also obtained from these velocities. It is possible to discretize velocities and lattice configuration differently, as has been shown in Refs. [72][77]. Other LBM models like the D3Q27 model can be derived in the same way.

In order to couple the equations, both, LBE and NS equations are required to solve the same physics. This is proven in the Chapman-Enskog expansion described in Appendix A.

3.3 Implementation of the Lattice Boltzmann Method

Lattice Boltzmann Methods, as the name suggests, work on a given lattice. Depending on the field of application, different lattices may be used. These are named DXQY, where X is the number of dimensions, 2 in this case, and Y determines the number of distinct lattice velocities. LBM can be described as a type of cellular automaton, which means that the fluid is modeled by many cells of the same type. All cells are updated each time step by simple rules, that take into account the state of the surrounding cells. The complex behavior of the automaton emerges from the interaction of the cells, and not, for example, by describing system properties as functions of space and time.

The most general form of the lattice Boltzmann equation is:

$$f_i\left(x+e_t\Delta t, t+\Delta t\right)= f_i\left(x,t\right)+\Omega\left(f\left(x,t\right)\right) \qquad i=0,1,...(N-1) \tag{3.31}$$

Equation (3.31) states that the streamed particle distribution function (PDF) f_i at the neighboring node at the next time step is the current PDF plus the collision operator Ω_i. The streaming of a PDF occurs in the time Δt over a distance Δx which is the distance between the lattice sites. Here e_i is the velocity vector in the i^{th} direction, N is the total number of velocity vectors for the model, **x** is the position vector and t is the current time. The collision operator may be further simplified into a linear collision term that relaxes the PDF to an equilibrium state [70]. This form of the lattice Boltzmann equation is called the LBGK equation and is given as:

$$f_i\left(x+e_i\Delta t, t+\Delta t\right)= f_i\left(x,t\right)-\frac{f_i\left(x,t\right)- f_i^{eq}\left(x,t\right)}{\tau} \quad \text{i = 0,1,…(N-1)} \tag{3.32}$$

Here, τ is the single relaxation parameter, which controls the rate of approach to equilibrium and f^{eq} represents the local equilibrium PDF. The parameter τ is related to the kinematic viscosity, ν, of the fluid as:

$$\nu=\left(\tau-\frac{1}{2}\right)c_s^2\Delta t \tag{3.33}$$

Kinematic viscosity is a function of τ, the speed of sound c_s and the time scale, Δt, for the problem. Since ν is positive, τ has to be greater than half. The speed of sound depends on the lattice Boltzmann model chosen.

The LBM models an incompressible fluid by particles that are allowed to move only along the lattice velocity vectors. A single cell of the D2Q9 model is depicted in Figure 3.1. Each side of the cell has length 1, so the volume of a cell is 1, too. The lattice velocities are shown and numbered. They point from the cell center to each face of the surrounding face, and to the midpoints of all face edges. For the simulation, all cells have

to store the number of particles that move along each of the lattice vectors, the particle distribution functions. They are usually called f_i where the values for i correspond to the numbers of the lattice vectors. If cells of this type are arranged in a three-dimensional grid, each lattice vector points to a neighboring cell that has a particle distribution function into the inverse direction. Note, that the vector with the number 0 has length zero, and amounts for particles resting in this cell. These particles are not moving anywhere in the next time step, but some of them may be accelerated due to collisions with other particles - so the amount of resting particles can change.

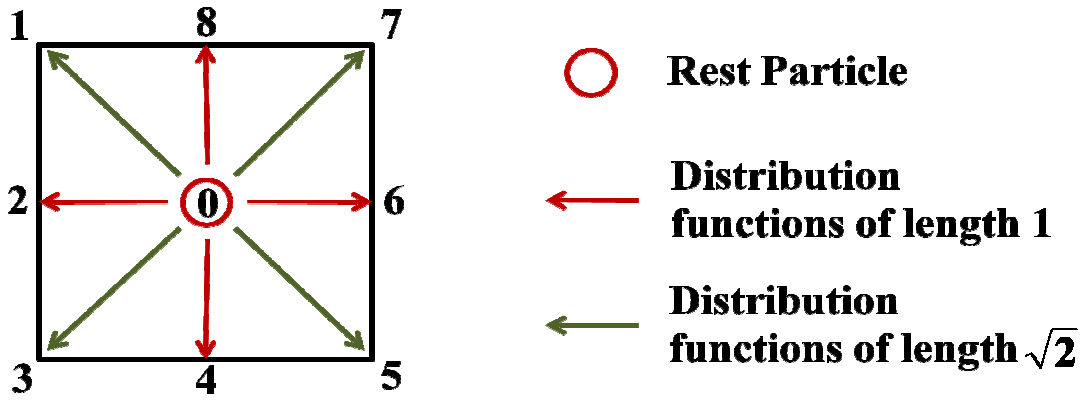

Figure 3.1: D2Q9 Lattice cell

For a square lattice, the LBGK D2Q9 model is expressed as:

(3.34)

For the D2Q9 model, ν is given by eq. (3.33) and $c_s^2 = c/3$, where $c = \Delta x / \Delta t$. For a square lattice, c =1, therefore, c_s^2 = 1/3. The particle speed e_i is given by:

$$e_i = \begin{cases} 0, & i = 0 \\ \left(cos(\pi(i-1)/2), sin(\pi(i-1)/2)\right), & i = 1,2,3,4 \\ \sqrt{2}\left(cos\left(\pi\left(i-4-\frac{1}{2}\right)/2\right), sin\left(\pi\left(i-4-\frac{1}{2}\right)/2\right)\right), & i = 5,6,7,8 \end{cases} \quad (3.35)$$

The local equilibrium PDF f^{eq} is a function of the macroscopic velocity at each lattice site and is computed as:

$$f_i^{(eq)} = t_i\rho\left[1 + 3(e_i \cdot u) + \frac{9}{2}(e_i \cdot u)^2 - \frac{3}{2}u \cdot u\right],$$
$$t_0 = \frac{4}{9}; \quad t_i = \frac{1}{9}, i = 1,2,3,4; \quad t_i = \frac{1}{36}, i = 5,6,7,8 \quad (3.36)$$

where t_i is the weighting factor specific for each velocity direction, ρ is the density per node and $\mathbf{u} = (u_x, u_y)$ is the macroscopic flow velocity. The three scalar products between the velocity and lattice vectors can be calculated easily. They need to be scaled accordingly and then summed up to be adjusted by the according weight and density. Now, depending on τ the fluid reaches this equilibrium faster or slower. The new particle distribution functions f_i' are calculated with:

$$f_i' = (1-\tau)f_i + \tau f_i^{(eq)} \quad (3.37)$$

These f_i' are then stored in the corresponding cell. When all cells have been collided the next stream step can be performed. The combined collision and streaming step is shown in Equation (3.34). From the particle distribution functions two important physical values can be calculated. By summing up all 9 distribution functions the density for the volume of this cell can be calculated, assuming that all particles have the same mass of 1. As the distribution functions contain the amount of particles moving in a certain direction for each cell, the sum of all particles in a single cell is its density (the

mass per volume). Another important information for each cell is the speed and overall direction in which the particles of one cell move. For this the momentum density needs to be calculated. It is again the sum of all particle distribution functions, but each distribution function is first multiplied by the lattice vector. Thus, the particle distribution function 0 is multiplied with $(0, 0)^T$, which always amounts to zero, distribution function f_1 is multiplied by $(-1, 1)^T$ and added to distribution function f_2 times $(-1, 0)^T$ and so on. This results in a two-dimensional vector that is scaled by the density, as the particle distribution functions contain a total amount of particles. Therefore, simply dividing the momentum density by the density, calculated as described above, yields the velocity vector for a cell. For simplicity the density is usually set to one in the beginning of a simulation. While the LBM is used to simulate incompressible fluids, meaning that the density is constant everywhere in the fluid, this constraint is relaxed during a LBM simulation. In a simulation one will usually encounter density differences, but for reasonable parameters the overall behavior will equal that of an incompressible fluid. Thus the density and velocities can be computed at each node as:

$$\rho = \sum_{i=0}^{8} f_i \,, \qquad \rho u = \sum_{i=1}^{8} f_i e_i \tag{3.38}$$

The change in pressure can be calculated as:

$$\delta p = (\rho - \rho_m) c_s^2 = \frac{(\rho - \rho_m)}{3} \tag{3.39}$$

where ρ_m is the mean density of the fluid. The simulation process consists of two steps that are repeated for each time step. One is the stream step, in which the actual movement of the particles throughout the grid is performed, the other accounts for the collisions that occur during this movement, and thus is called the collide step. For

simplicity, the size of a cell, the length of a timestep and the initial density will be normalized to 1 and will not be included in the following formulas.

The stream step consists only of copying operations, as shown in Figure 3.2. For each cell, all distribution functions are copied to the adjacent cell in the direction of the lattice vector. Hence, for the cell with the coordinates [i, j] the distribution function for the lattice vector pointing upwards is copied to the upward distribution function of cell [i, j + 1]. As the lattice vector 0 does not point anywhere, its particle distribution function is not changed in the stream step. In practice, while performing streaming, care must be taken to prevent any overwriting of distribution functions that are needed for the streaming of another cell.

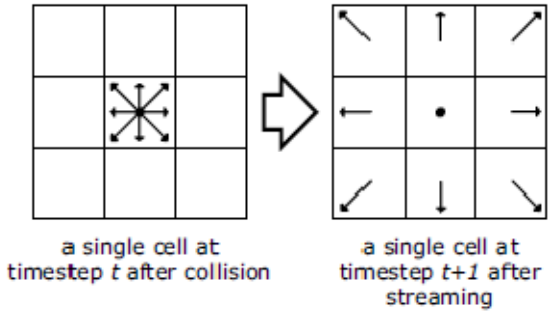

Figure 3.2: Particle distribution function of a D2Q9 lattice before and after streaming [149].

The collision step is a bit more complicated. The streaming step would just result in the probability distribution functions moving through the grid. The velocities and densities of the cells would change, with no further interaction. However, in a real fluid, the particles are constantly colliding, scattering other particles into different directions and due to their chaotic movement influencing adjacent layers of fluid. The collision step does not change the density or velocity of a cell; it only changes the distribution of the particles for all particle distribution functions, as depicted in Figure 3.3.

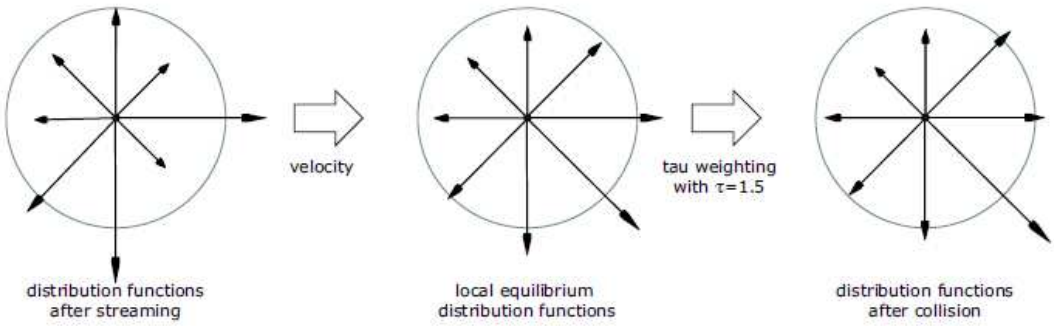

Figure 3.3 : During the collide step the distribution functions from the stream step are used to calculate the velocity in each cell, which is necessary for the local equilibrium distribution functions [149].

Consider, for example, a cell [*i, j*] where the fluid moves along the positive x-axis. It will not lose any particles during collision, but the movement will be scattered to other lattice velocities that point in direction of the positive x-axis. The ones pointing into the opposite directions will become smaller. In the next stream step, neighboring cells with x coordinate $i + 1$ will receive a slightly larger particle distribution function from cell [*i, j*], while cell at $i - 1$ will receive slightly smaller ones. In the collide step several parameters are necessary. The relaxation time τ, that can have values in the range of 1/2 and 2, determines the viscosity of the fluid. For small values (< 1) the fluid will behave more like honey, while values close to 2 will result in very turbulent and chaotic behavior (resembling fluids like water). The density of the cell will be denoted by ρ while the velocity vector is $\vec{u} = (u_1, u_2)^T$.

The solution procedure for a typical LB method during one time step is shown in Figure 3.4.

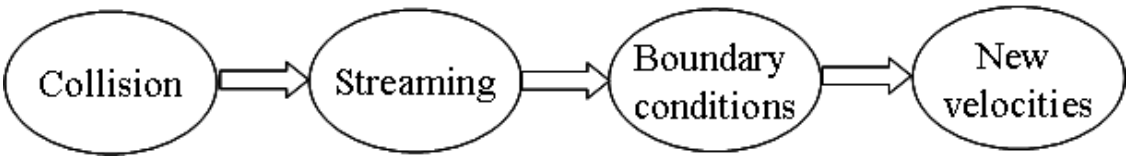

Figure 3.4: A typical time step in the Lattice Boltzmann Method

The above process is repeated until the PDFs are relaxed to an equilibrium state in the case of a steady flow problem. In the case of transient flow phenomena, the PDFs and velocities at each node will not converge to an equilibrium value, as in the case of the conventional Navier-Stokes solver.

Note that simulation of compressible fluid flows using the isothermal LBGK model is not practical. To adequately represent the speed of sound in air ($c_s|_{T=300K} = \sqrt{\gamma RT} \approx 300m/s$ and $\nu_{air} \approx 10^{-5}\, m^2/s$), considered as an ideal gas, a time step $\delta_t = \nu/\left((\tau - 1/2)c_s^2\right) \approx 10^{-8}\ s$ would be required for the D2Q9 ''stream-and-collide'' LBGK scheme (with $(\tau - 1/2) = 10^{-2}$ to ensure the numerical stability). The corresponding grid size is $\delta_x = \sqrt{3}c_s\delta_t \approx 1\ \mu m$. Similar estimates for water (c_s ≈1500 m/s and $\nu_{H2O} \approx 10^{-7}$ m/s) yield $\delta_t \approx 10^{-11}$ s and $\delta_x \approx 10$ nm [118].

3.4 Boundary Conditions

Boundary conditions are a very important part of the LBM. The challenge for researchers has been to develop and implement boundary conditions that are second-order accurate in space so as to match the accuracy of the lattice Boltzmann equation. Several boundary condition treatments have been proposed for the D2Q9 model. Some of these treatments which are used in the present study are described below.

3.4.1 No slip wall

The bounce-back scheme is the simplest type of treatment used for a solid wall. It has its roots in the Lattice Gas method. In this treatment when a particle streams into a wall or lattice site representing something solid, it will bounce back from that site and return in the direction it originated. No-slip walls imply that close to the boundary the fluid does not move at all. Hence, each Lattice Boltzmann cell next to a boundary should have the same amount of particles moving into the boundary as moving into the opposite direction. This will result in a zero velocity, and can be imagined as reflecting the particle distribution functions at the boundary. The reflection process is shown in Figure 3.5, for the no-slip case. The top two rows in the figure represent lattice cells in the flow field and the third, bottom, row represents the wall. The colored lattice directions which point toward the wall reflect back into the flow domain by the application of the no-slip boundary condition.

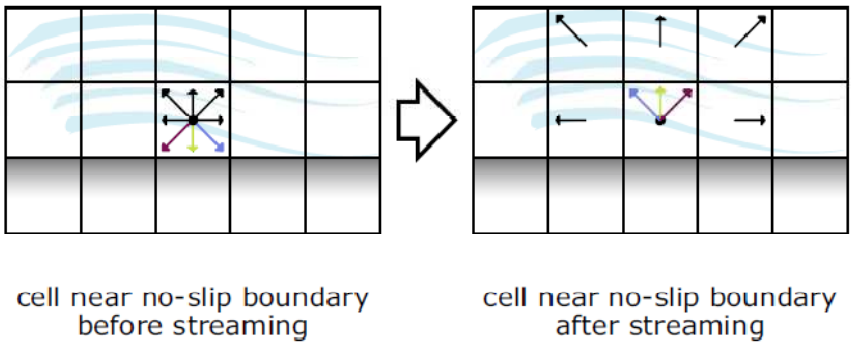

Figure 3.5 : No-slip boundary condition representation, [149].

For the implementation of the no-slip boundary condition, this means, that boundary and fluid cells need to be distinguished. A flag array has to be introduced and initialized to declare all boundary cells as “no-slip” and all inner cells as “fluid”. The real handling of the boundary cells would happen in the streaming loop. Here the flag array

are checked, and if the neighboring cell is a boundary cell, the opposite distribution function from the current cell would be taken.

A particle will return to the lattice site or node it originated from in two time steps since the wall is located exactly one lattice distance away. Although, it is simple to implement, this method has been shown to be first-order accurate and produced a slip velocity at the wall. A slight modification to this bounce-back method is the "shifted" or "halfway" bounce-back method. This method, which places an imaginary wall halfway between nodes, is second-order accurate. Equations (3.16) and (3.17) are used to calculate PDF using these two methods. Figure 3.6 illustrates the two methods.

$$f_{i'}(x_F, t + 2\Delta t) = f_i^c(x_F, t) \tag{3.40}$$

$$f_{i'}(x_F, t + \Delta t) = f_i^c(x_F, t) \tag{3.41}$$

Equation (3.40) says that the post-advection PDF value in the direction opposite of the wall i' at fluid node F ($f_{i'}$) will be equal to the post-collision PDF value in the direction of the wall i (f_i^c) after two time steps. This is the bounce-back method whereas eq. (3.41) says that this is true for the halfway bounce-back scheme after just one time step. This is the shifted bounce-back method. While an improvement in accuracy is seen for the halfway bounce-back method, a slip velocity still existed at the wall. The other drawback of the bounce-back methods is that they don't lend themselves to accurately representing more complex boundaries. For example, with either method a curved surface must be represented with a stair step approximation of that surface. This effect can somewhat be mitigated by increasing the resolution of the lattice sites to get a smoother approximation of the surface, but this adds to computational time. The major advantage

of the bounce-back methods is that they are simple, easy to implement, and cost little computational time.

In order to account for the curved cylinder boundary, in the present study, an interpolation based boundary condition presented by Bouzidi et al. [86] has been implemented. Quadratic interpolations in combination with the bounce-back method are used to calculate PDF values in the present study. Figure 3.6 illustrates the two cases where the wall is less than one-half Δx and greater than one-half Δx.

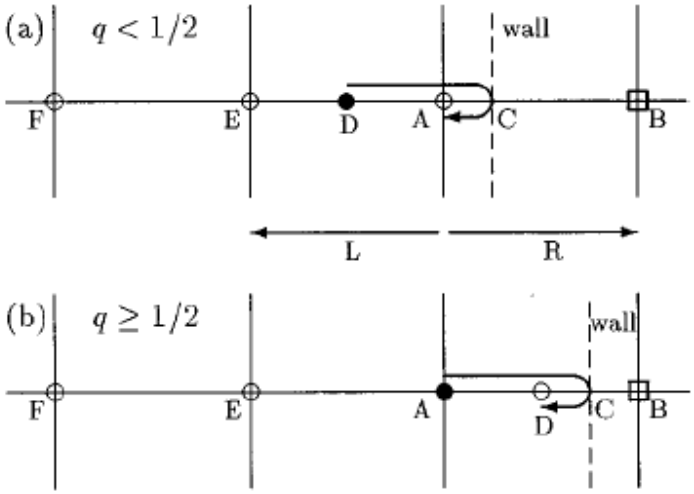

Figure 3.6: Illustration of the Bouzidi Interpolation boundary condition treatment

As in the case of the bounce-back scheme, the post advection PDFs in the opposite direction ($f_{i'}$) are calculated based on the value of q, as:

$$f_{i'}(x_A, t+\Delta t) = q(2q+1)f_i^c(x_A,t) + (1+2q)(1-2q)f_i^c(x_A - e_i, t) - q(q-2q)f_i^c(x_A - 2e_i, t), \qquad q < {}^1/_2 \tag{3.42}$$

$$f_{i'}(x_A, t+\Delta t) = \frac{1}{q(2q+1)}f_i^c(x_A,t) + \frac{(2q-1)}{q}f_i^c(x_A,t) + \frac{(1-2q)}{(1+2q)}f_i^c(x_A - e_i, t), \quad q \geq {}^1/_2 \tag{3.43}$$

Here, q is the normalized distance from the node A to the wall, i.e. $q = |AC|/|AB|$.

3.4.2 Velocity boundary conditions

The velocity boundary conditions proposed by Zou and He [85] has been implemented in the present study for use as inlet and outlet boundary conditions. Consider a solid node that represents a wall below the flow regime as shown in Figure 3.7.

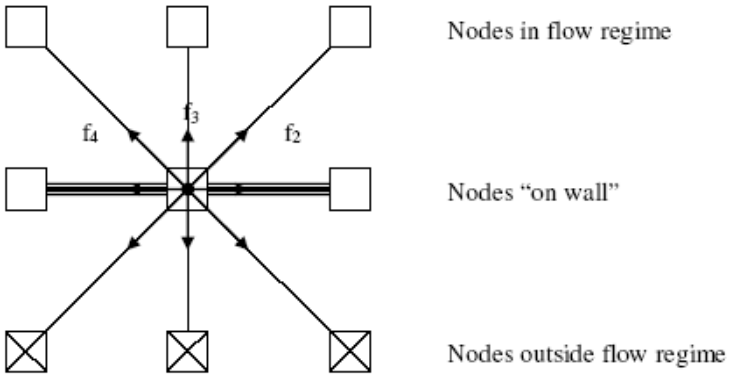

Figure 3.7: Illustration of the Zou and He [86] boundary condition

This hydrodynamic boundary treatment calculation uses the conservation equations (Equations (3.38)) for density and momentum density to get the following three equations:

$$f_2 + f_5 + f_6 = \rho - (f_0 + f_1 + f_3 + f_4 + f_7 + f_8) \tag{3.44}$$

$$f_5 - f_6 = \rho u_x - (f_1 - f_3 - f_7 + f_8) \tag{3.45}$$

$$f_2 + f_5 + f_6 = \rho u_y + (f_4 + f_7 + f_8) \tag{3.46}$$

Solving eqns. (3.44) and (3.46) gives:

$$\rho = \frac{1}{1-u_y}[f_0 + f_1 + f_3 + 2(f_4 + f_7 + f_8)] \tag{3.47}$$

The present scheme assumes that bounce-back for the non-equilibrium part of the particle distribution normal to the wall applies. This gives the following fourth equation:

$$f_2 - f_2^{eq} = f_4 - f_4^{eq} \Rightarrow f_2 = f_4 + \left(f_2^{eq} - f_4^{eq}\right) \tag{3.48}$$

Using the equilibrium equations for f_5 and f_6, f_5 can be solved for directly. Finally, using eqns. (3.45) and (3.46), expressions for f_5 and f_6 can be derived in terms of u_x and u_y. The final equations for f_2, f_5 and f_6 are:

$$f_2 = f_4 + \frac{2}{3}\rho u_y \tag{3.49}$$

$$f_5 = f_7 - \frac{1}{2}(f_1 - f_3) + \frac{1}{2}\rho u_x + \frac{1}{6}\rho u_y \tag{3.50}$$

$$f_6 = f_8 + \frac{1}{2}(f_1 - f_3) - \frac{1}{2}\rho u_x + \frac{1}{6}\rho u_y \tag{3.51}$$

The collision step is applied to the boundary nodes also. With the appropriate values of the velocity components, this boundary condition can be used for no-slip boundary condition treatment as well. Although this scheme yields improved accuracy compared to the bounce-back boundary condition, it is difficult to implement for general geometries because there is a need to distinguish distribution functions according to their orientation to the wall. Nevertheless, for the cases considered in the present study, this boundary treatment was sufficient to obtain agreeable results.

3.5 Lattice Boltzmann – Navier-Stokes Coupled Methodology

3.5.1 Conversion between microscopic and macroscopic variables

The LBE solves for the microscopic variables where as the RANS solver used in the present study solves for the macroscopic values such as density, velocities and pressure. In order to couple a LB and NS solver, the transformation between the LB variables and the macroscopic variables needs to be determined. A formulation for

conversion from one set of variables to another is described below. This conversion was built on the formulation of Lätt [120]; however a different coupling approach is used in the present study.

In this approach, three reference units are considered, dimensionless units, lattice units and physical units represented by subscripts d, lb and p respectively. Also, reference quantities are denoted by the subscript o. First the reference length of the simulation is chosen. Say, N lattice sites are used to represent $l_{o,p}$ physical reference length. Therefore, the reference length in lattice units, $l_{o,lb}$ = N. In the dimensionless units system, by definition, the reference velocity and length are unity.

$$u_{o,d} = 1; l_{o,d} = 1 \tag{3.52}$$

Therefore, the lattice spacing δx_d in dimensionless units is given by:

$$\delta x_d = \frac{l_{o,d}}{N} = \frac{1}{N} \tag{3.53}$$

Assume a reference velocity of $u_{o,lb}$ (<0.1) in lattice units. Then the dimensionless time step can be obtained as:

$$\delta t_d = \delta x_d * u_{o,lb} \tag{3.54}$$

Using dimensional analysis, the reference time scale is given by:

$$t_{o,p} = \frac{l_{o,p}}{u_{o,p}} \tag{3.55}$$

The physical time step and the physical spacing are then formulated as:

$$\delta t_p = \delta t_d * t_{o,p} \quad \delta x_p = \delta x_d * l_{o,p} \tag{3.56}$$

The dimensionless and then the physical velocity are calculated as:

$$u_d = \frac{\delta x_d}{\delta t_d} * u_{lb}; \quad u_p = \frac{l_{o,p}}{t_{o,p}} * u_d = \frac{l_{o,p}}{t_{o,p}} * u_{o,p} * u_{lb} \tag{3.57}$$

Note that the initial density in the NS solver is kept as 1 kg/m^3 to keep it consistent with the reference density of 1 in lattice units. However, they can also be converted using $\rho_{lb} = \rho_p / \rho_{o,p}$.

Change in pressure in lattice units is calculated using an equation of state type of formulation as follows:

$$\delta p_{lb} = c_s^2 \left(\rho_{lb} - \rho_{o,lb} \right) \tag{3.58}$$

Finally, using dimensional analysis, the change in pressure and finally the physical pressure are obtained as:

$$\delta p_p = \rho_{o,p} * u_{o,p}^2 * \delta p_{lb}; \quad p_p = p_{o,p} + \delta p_p \tag{3.59}$$

where $p_{o,p}$ is the reference physical pressure. The reverse of the above equations is used to obtain the values of the variables in lattice units.

3.5.2 Boundary condition formulation for the LBE-NS coupled methodology

The present study uses a one cell overlap between the LB and NS (node-centered) solvers where the information is exchanged between the two solvers. Figure 3.8 below summarizes this formulation. In this figure, i represents the ith node in each of the

domains and $imax_{lb}$ represents the maximum i^{th} node in the LB domain. I=0 represents the ghost cell location in the NS solver.

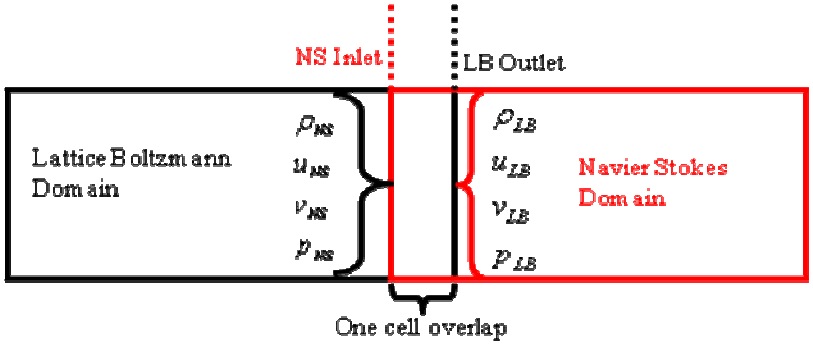

$$\rho_{LB_{i=i\max LB}} = \rho_{NS_{i=2}}$$
$$u_{LB_{i=i\max LB}} = u_{NS_{i=2}}$$
$$v_{LB_{i=i\max LB}} = v_{NS_{i=2}}$$

$$\rho_{NS_{i=0}} = \rho_{LB_{i\max LB-1}}$$
$$u_{NS_{i=0}} = u_{LB_{i\max LB-1}}$$
$$v_{NS_{i=0}} = v_{LB_{i\max LB-1}}$$
$$p_{NS_{i=0}} = p_{LB_{i\max LB-1}}$$

Figure 3.8. Information exchange between LB and NS solvers.

At the interface, the LB microscopic values are converted to macroscopic density, velocities and pressure based on Eqns. (3.57) and (3.59). In the node-to-node matching grid used in the present study, these macroscopic values are read by the NS solver at the corresponding node and used as ghost cell information when formulating the characteristic inflow/outflow type boundary condition at the inlet, i = 1.

The microscopic density and velocity values are obtained by converting the macroscopic values based on the formulation described in the previous sub-section. These values are then used to impose the boundary condition at the LB interface. This information exchange is performed at every time step.

Low Mach number implies a much larger acoustic time scale compared to the convective time-scale. Trying to project the incompressible NS equations onto the compressible NS equations requires expensive methods such as preconditioning. Instead, the compressible NS equations are projected onto its incompressible counterpart so that it

yields the incompressible NS equations in the limit of small Mach number. Therefore, the Mach number dependency on pressure is treated by adding the fluctuating pressure which scales with the inertia of the velocity field and the reference pressure which is related to the mean speed of sound. The present coupling methodology at the interface between the incompressible LBE solver and the compressible NS solver has been implemented using this procedure such that the overall performance of the coupled solver is not deteriorated due to the coupling procedure. This is similar to that explored by Iourokina and Lele[121] and Hou and Mahesh[122].

The extension of the coupled methodology for curvilinear surfaces (Figure 3.9) is performed by using bilinear interpolation of the flow field quantities at the curved surface. This interpolation, used by Tannehill et al[123] for irregular boundaries, was sufficient for the present studies since the grid spacing in the region of use is very small and the gradients within one cell are not large. Although the boundary condition is locally first-order accurate, the solution is still globally second-order accurate due to the spatially second-order accurate solvers used. This is similar to the method used by industrial solvers such as OVERFLOW, where a local first-order accurate boundary condition is used in globally second-order accurate solver.

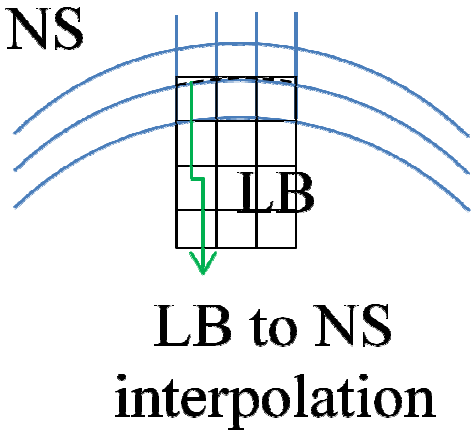

Figure 3.9: Coupled methodology for curved surfaces.

Note that the LBE solver used in the present analysis does not use turbulence modeling. Since the flow in the synthetic jet cavity used is incompressible layer and the LBE domain extends only into the laminar sublayer of the NS flow, turbulence modeling has not been used in the LBE solver. However, turbulence modeling has been used in the NS solver.

CHAPTER 4

NUMERICAL STUDIES AND VALIDATIONS OF THE LATTICE BOLTZMANN SOLVER

In order to further study the physics of the phenomena occurring close to the active flow control devices used for hub drag reduction, and to correctly model the flow in high Knudsen number regions, the present lattice Boltzmann (LBE) solver has been used.

Following the procedure described in Chapter 3, the present LBE solver has first been validated for benchmark channel flows like the Poiseuille flow and the Couette flow. In order to compare the solution from the lattice Boltzmann formulation with that from a conventional Navier-Stokes solver, validation has been done for flow past a two-dimensional cylinder in a channel. The results for these cases are presented below.

4.1 Validations for the Lattice Boltzmann Solver

4.1.1 Poiseuille flow

In order to validate the present LBE solver, a two-dimensional benchmark Poiseuille flow has been studied and compared to analytical solution. The computational domain consists of a two-dimensional channel with its width assumed to be 2L = 2. The length of the channel is set to twice the width. The top and bottom walls are implemented as a wall with no-slip boundaries while the left and right boundaries are implemented as inlet and outlet boundaries respectively. Assume *xmax* and *ymax* number of lattice nodes uniformly distributed in the x (streamwise) and y (cross stream) directions respectively. Uniform distribution ensures that the streamwise and cross stream spacing between

adjacent nodes is same. Therefore, $\Delta x = \Delta y = \delta = 2/(ymax-2)$, since the first and last nodes are the bounce-back nodes with the wall located halfway between the bounce-back node and the first flow node. Let number of nodes in the x direction be lx = *xmax* and in the y direction be ly = *ymax*-2. The flow is initially assumed to be at the equilibrium distribution, with a constant density ρ_0 and zero velocity. Steady state is assumed to be reached when the residue drops below 10^{-8}. The residue is defined as:

$$residue = \sqrt{\frac{\sum_i \sum_j \left[\left(u_x(i,j,t+\Delta t) - u_x(i,j,t)\right)^2 + \left(u_y(i,j,t+\Delta t) - u_y(i,j,t)\right)^2 \right]}{\sum_i \sum_j \left[u_x^2(i,j,t) + u_y^2(i,j,t) \right]}} \tag{4.1}$$

where *i* and *j* are the node indices along the x and y directions respectively. Also, maximum relative error in velocity is defined as:

$$error_{\max} = \max \frac{\sqrt{\left(u_x^t - u_x\right)^2 + \left(u_y^t - u_y\right)^2}}{u_0} \tag{4.2}$$

where u_x^t and u_y^t are the analytical x and y velocities respectively and u_0 is the peak velocity. The maximum error is taken over the entire domain.

4.1.1.1 Validation of the two-dimensional Poiseuille flow

The Reynolds number of the flow is assumed to be 10 and the relaxation parameter (τ) is chosen as 0.8 (based on the requirement that it satisfy the relation $Re = \frac{u_o 2L}{\nu}$, where 2L=ly=N). The initial peak velocity u_0 is set to 0.015625 at the inlet. The x direction velocity profile obtained from the present simulations has been compared with the analytical solution for lx = 128 and ly = 64. After steady state is reached, when the residue is less than 10^{-8}, the streamwise velocity u_x at the outlet of the channel is

normalized using the maximum centerline velocity at the outlet and this profile is compared to the analytical Poiseuille profile given by:

$$\frac{u_x}{u_c} = 1 - \frac{y^2}{L^2} \tag{4.3}$$

Here u_c is the maximum centerline streamwise velocity at the outlet. The results obtained are shown in Figure 4.1. The comparison shows excellent agreement between the Poiseuille profile obtained from analytical solution and present simulations.

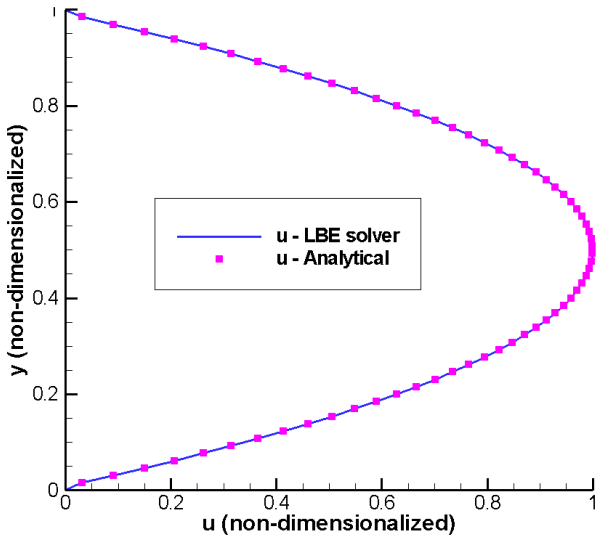

Figure 4.1: Comparison of the Poisseuille profile between the analytical and present simulations.

4.1.1.2 Spatial order of accuracy of the solver

In order to verify the spatial accuracy of the present solver, grid sensitivity studies have been performed. Similar to the test conditions provided in the paper by Zou and He [85], Reynolds number (Re) is assumed to be 10 and the relaxation parameter τ is set to 0.8. While keeping these values constant, the lattice spacing δ is varied from ½ to 1/64 in multiples of two. The peak velocity, u_0, varies with δ according to the equation:

$$u_0 = \frac{\nu \,\mathrm{Re}}{2L} = \frac{[(2\tau - 1)/6]\delta \,\mathrm{Re}}{2L} \tag{4.4}$$

For each of six different grid sizes based on δ, the max error in velocity is calculated. The spatial order of the code is then calculated using the following formula:

$$order = \frac{\log\left(\frac{\text{Maximum error in coarser grid}}{\text{Maximum error in finer grid}}\right)}{\log(2)} \tag{4.5}$$

where the number '2' is obtained by dividing ly (number of lattice nodes in the cross stream direction) of the finer grid with that of the coarser grid.

Table 4.1 shows the spatial order of accuracy of the present solver for the 2-D Poiseuille flow case. It can be seen that as the grid becomes finer, the order approaches two. This implies that the code is second-order accurate, given sufficient number of grid points.

Table 4.1: Spatial order of accuracy for the lattice Boltzmann solver for a 2-D Poiseuille flow

Grid (lx x ly)	Order
8 x 4	-
16 x 8	1.7845
32 x 16	1.7014
64 x 32	1.8568
128 x 64	1.9281
256 x 128	1.9614

4.1.2 Validation of Couette flow

Another benchmark problem of interest is the Couette flow. The domain considered is a two-dimensional channel. The left and right boundaries of the channel are modeled as the inlet and outlet respectively, similar to the Poiseuille flow case. The bottom boundary is set as a no-slip wall whereas the top boundary is implemented as a moving wall with a uniform velocity u_0. Initially the flow is at rest and the probability

distribution functions (PDFs) are set to their equilibrium values. For Re = 10, τ = 0.8 and a 128 x 64 uniform Cartesian grid, after convergence, the u_x component of velocity at the outlet was non-dimensionalized by u_0. This velocity is compared to the analytical solution given by $u_x/u_0 = y/2L$, where 2L is the channel width.

Figure 4.2 shows the comparison of the u_x velocity components between the present computation and the analytical solution. Excellent agreement is seen between the two profiles.

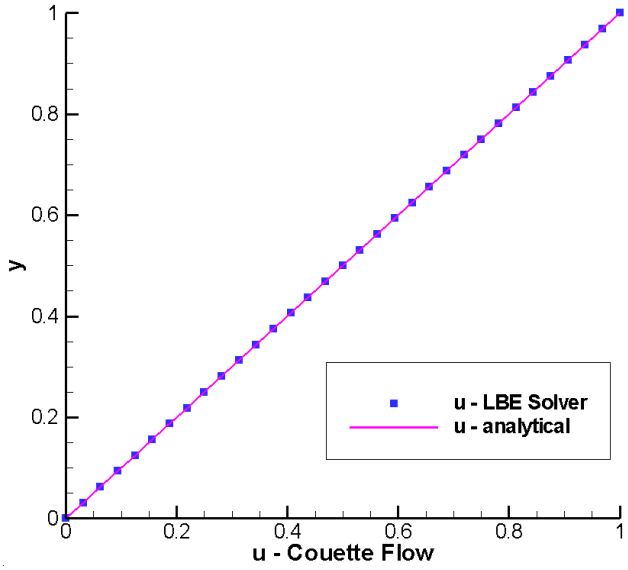

Figure 4.2: Comparison of analytical and computed u velocity profiles for Couette flow in a 2-D channel

The Poiseuille and Couette flow validations show the present lattice Boltzmann models' capability to handle free, non-obstructed, fluid flow.

4.1.3 Flow past a cylinder in a two-dimensional channel

A benchmark case of flow past a circular cylinder in a 2D channel, described by Schäfer and Turek [140], was chosen to validate the LB solver. The results are validated against those given by Mei et al. [151]. Figure 4.3 shows the domain, which is a two-

dimensional channel with no-slip walls at the top and the bottom. The center of the cylinder of radius, R = 12.8 units is placed such that it is a distance 4R and 4.2R from the bottom and top wall of the channel respectively. The inlet is a distance 4R away from the center of the cylinder, in front of it. The exit boundary condition is approximately 40R downstream of the cylinder center.

The grid is a 564x105 uniform Cartesian grid. Reynolds number based on average inlet velocity ($\overline{U}$) and cylinder diameter (2R) is 100. Single relaxation parameter, τ = 0.55 and $\overline{U}$ = 0.0651 are used to match the values used in reference [151]. Note that these values of τ and $\overline{U}$ satisfy the relation $Re = 2R\overline{U}/\nu$, where ν is a function of τ. The initial flow field is set to the Poiseuille flow velocity profile throughout the channel. Lift and drag coefficients are calculated based on the momentum-exchange method described by Mei et al. [151]. Strouhal number is calculated as St = 2R/$\overline{U}$ T. Here, T is the period of the lift curve.

As expected, the flow is unsteady for the given Reynolds number and periodic vortex shedding is observed as shown in Figure 4.4. St was calculated to be 0.2935 which is around 2.2% off from the CFD predicted St. Minimum and maximum values of C_l and C_d were obtained and compared with CFD predictions and the results obtained by Mei et al. [151] using an LBE solver. These results are shown in Table 4.2. C_d^{min} and C_d^{max} from the present computation agree to within 3.5% of expected results. However, C_l^{min} and C_l^{max} are off by around 8% and 11% respectively from predictions. The difference in C_l could be because no correction was made to include the one-half grid spacing at wall boundaries where halfway wall bounce-back was implemented. The results shown above validate the LBE solver for use in the coupled Lattice Boltzmann-Navier-Stokes studies.

From these calculations, it is observed that LBE alone is sufficient to capture the global flow field and integrated forces accurately. However, in order to use LBE for a larger domain, the number of grid points required is much larger compared to the NS solver. This is due to the requirement of the LBE grid spacing to be of the order of the mean free path. This would in turn require a lot more computational time to simulate compared to the NS alone solutions. Therefore, a coupled methodology is preferred which could adopt the better characteristics from both the solvers.

The Navier-Stokes solver used in the Lattice Boltzmann-Navier-Stokes (LB-NS) coupled methodology has been validated by Min et al. [131][132] for several benchmark cases. These studies are not repeated in the present study. A subset of the Navier-Stokes simulations performed by the present author has been documented in Appendix B.

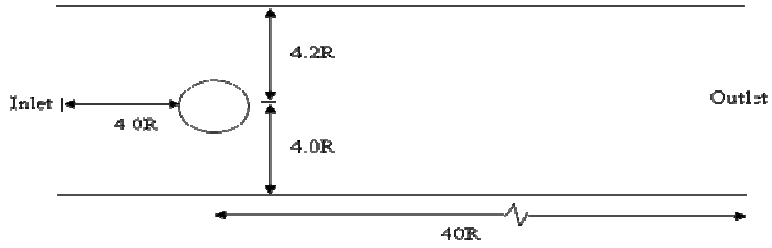

Figure 4.3 : **Cylinder placement in the 2D channel.**

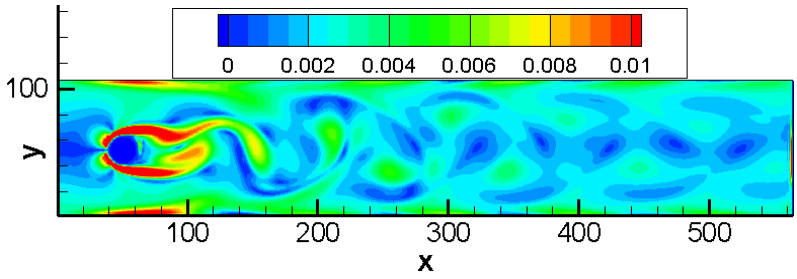

Figure 4.4 : Instantaneous vorticity contours for a flow past a 2D cylinder in a channel.

Table 4.2. Comparison of St, C_l and C_d between LBE solvers and CFD for the flow over a 2D cylinder

Number	Method	St	C_d^{max}	C_d^{min}	C_l^{max}	C_l^{min}
1	Present study	0.2935	3.1747	3.1123	0.9046	-0.9583
2	CFD	0.2950-0.3050	3.2200-3.2400		0.9900-1.0100	
3	Mei et al. [151]	0.3033	3.2358	3.1771	1.0045	-1.0347
	% Difference between 1 and 2	2.2%	1.74%		10.55%	
	% Difference between 1 and 3	3.34%	1.93%	2.08%	11.04%	7.97%

4.2 Validations for the coupled Lattice Boltzmann-Navier-Stokes methodology

4.2.1 Wave traveling from Lattice Boltzmann to Navier-Stokes domain

In order to validate the LB-NS coupled methodology for simple flow problems a Gaussian wave originating from the LB domain is studied as it passes the LB-NS interface into the NS domain. A two-dimensional channel with dimensions of 0.02m x 0.005m was chosen. The domain is split into two equal halves with the left half modeled using the LBE solver and the right half modeled using the NS solver. The LB inlet is modeled as a time-varying sinusoidal velocity inlet boundary condition and the NS outlet as a characteristic outlet boundary. The outlet of LB and the inlet of NS are modeled as part of the LB-NS coupled boundary. The bottom and top walls of the channel are modeled as symmetry boundaries.

A uniform grid was chosen in both the streamwise and normal directions. The characteristic length was chosen as N = 51. Therefore, the LB and NS solvers each have a grid size of 101x51, with a node-to-node matching at the interface.

The LB domain is initialized with a constant reference velocity and density. The time-varying inlet boundary condition is defined as:

$$M = M_o + A\sin(\omega t)$$

$$\mathrm{A} = 0.01; \quad \mathrm{M_o} = 0.05$$

In the above equation, M represents the physical Mach number of the flow. The non-dimensional frequency is 7.35. The NS domain is initialized with freestream conditions. After one half sinusoidal cycle, free stream velocity condition is imposed at the inlet in order to observe the propagation of the velocity disturbance that was introduced. The disturbance propagates through the LB domain in the direction of the NS

domain. Due to the symmetry boundary conditions, the problem is essentially one-dimensional and the velocity could be analyzed by following the wave along the centerline of the channel.

Figure 4.5 shows the non-dimensional centerline velocity $(u-u_o)/A$ at different times along the channel length. The plot is shown at non-dimensional times $u_o t/L$ = 16.95, 50.85, 84.75, 118.65, 152.55, 186.45, 220.35, 254.25, 288.15. The dashed line in Figure 4.5 indicates the interface between LB and NS domains. No non-physical change in wave shape or spurious oscillations are observed at the interface.

Figure 4.6 shows the two-dimensional streanwise velocity of the wave traveling from the LB to the NS domain at times $u_o t/L$ = 16.95, 101.7, 186.45, 220.35, 254.25, 288.15 and 339. Again, a smooth transition of the wave between the domains is observed.

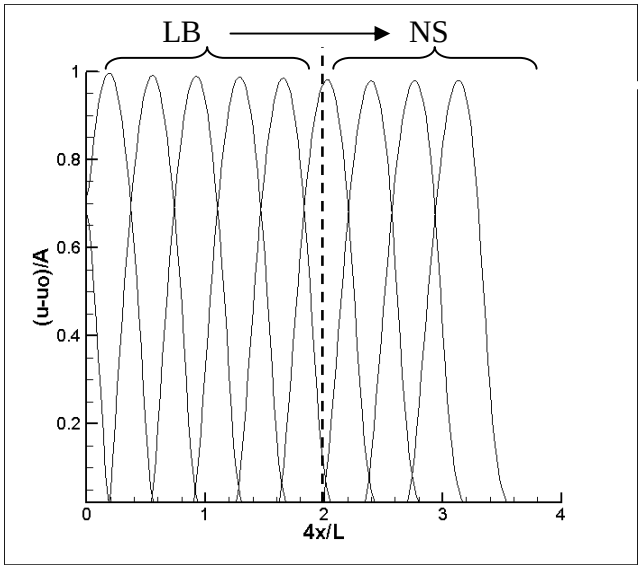

Figure 4.5 : Non-dimensional streamwise velocity along the channel at different time intervals using LB-NS coupled methodology

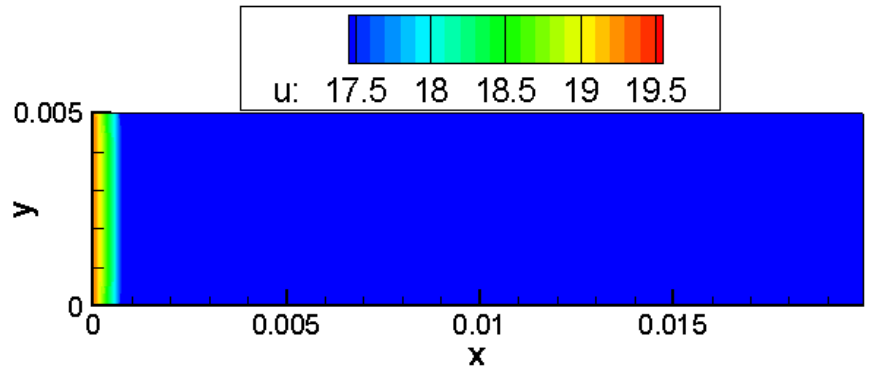

(a)

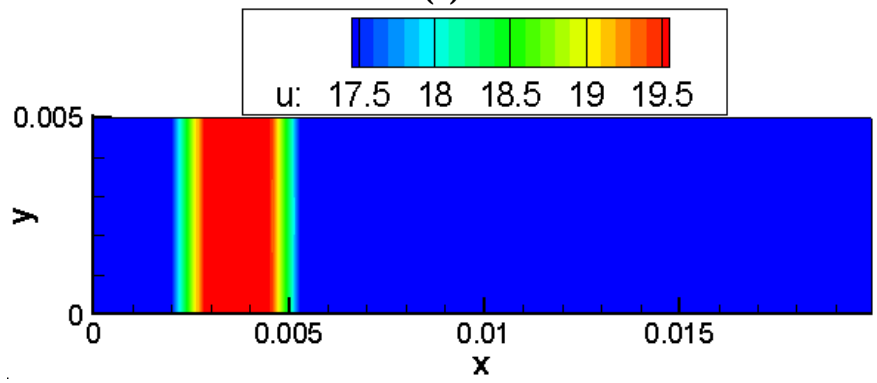

(b)

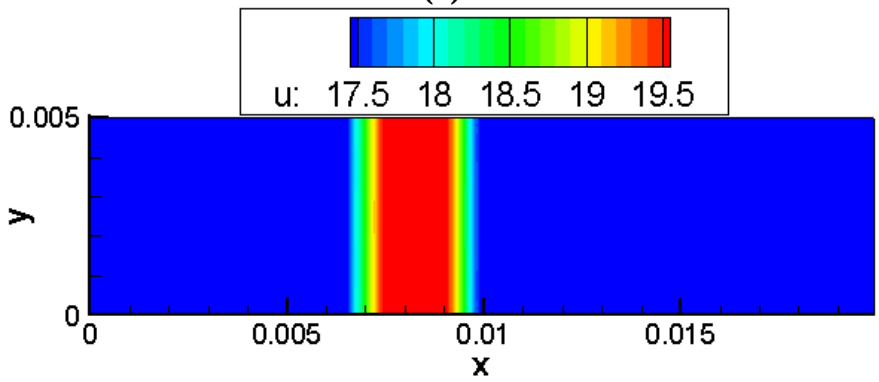

(c)

Figure 4.6 : Streamwise velocity of the wave traveling from LB to NS domain at $u_o t/L$ = (a) 16.95 (b) 101.7 (c) 186.45 (d) 220.35 (e) 254.25 (f) 288.15 (g) 339.

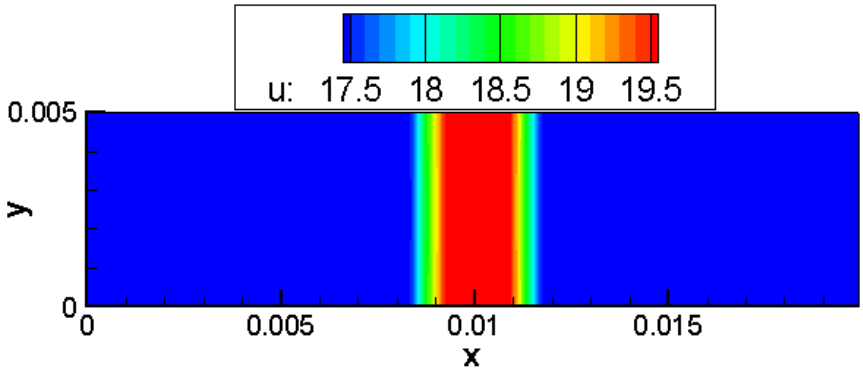

(d)

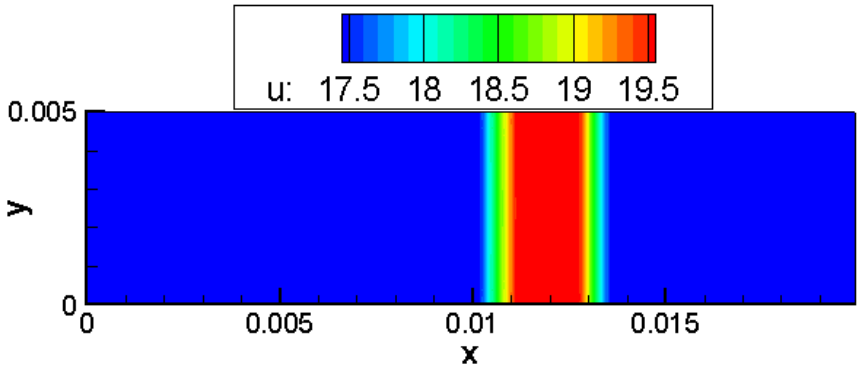

(e)

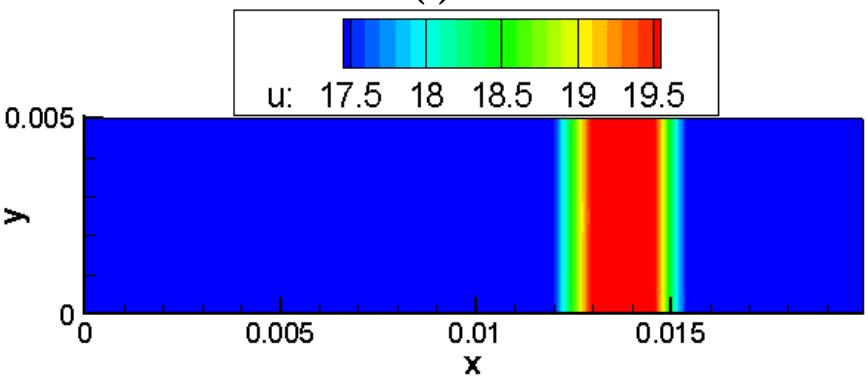

(f)

Figure 4.6 continued

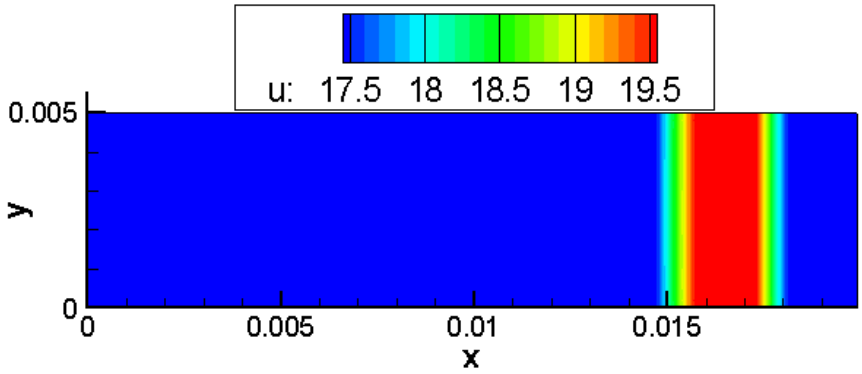

(g)
Figure 4.6 continued

4.2.2 Wave traveling from Navier-Stokes to Lattice Boltzmann domain

In order to ensure that the information propagates correctly not only from LB to NS domain, but also from NS to LB domain, as in a subsonic case, a wave traveling from the NS to the LB domain was studied. The wave is initiated from the NS domain and passes the interface to enter the LB domain. A two-dimensional channel, with the same dimensions and description as the one used in the case of the wave traveling from the LB to NS domain, was chosen for this study. All the inlet and outlet boundary conditions are reversed, compared to that shown in the previous sub-section. The right boundary of NS acts as an inlet with a sinusoidally varying inlet velocity.

With a characteristic length of N = 51, the same grid of 101 x 51 is generated for both LB and NS domains. The inlet boundary condition for the NS domain in non-dimensional units is given by:

$$M = M_o + A\sin(\omega t)$$

$$\mathrm{A} = 0.01; \quad \mathrm{M_o} = 0.05$$

Density is initialized to the reference density. The LB domain is initialized with the freestream conditions. After one half sinusoidal cycle, free stream velocity condition

is imposed at the inlet in order to observe the propagation of the velocity disturbance that was introduced. The disturbance propagates through the NS domain in the direction of the LB domain. The absolute value of the non-dimensional centerline streamwise velocity $|u-u_o|/A$ is shown in Figure 4.7. The dashed line in Figure 4.7 represents the interface between the LB and NS domains. The plots are shown at time intervals $u_o t/L$ = 16.95, 50.85, 84.75, 118.65, 152.55, 186.45, 220.35, 254.25, 288.15. No non-physical changes in the wave shape are observed due to the implementation of the LB-NS coupled interface.

Figure 4.8 shows the two-dimensional streanwise velocity of the wave traveling from the NS to the LB domain at times $u_o t/L$ = 16.95, 101.7, 186.45, 220.35, 254.25, 288.15 and 339. A smooth transition of the wave between the domains is observed. This shows that the LB-NS coupled methodology does not generate non-physical wave shapes and therefore could be used for studies on the active flow control concept.

In addition, the coupled LBE-NS methodology has been validated for the passage of an acoustic pulse from the LBE to the NS domain and vice versa. These studies have been documented in reference [152].

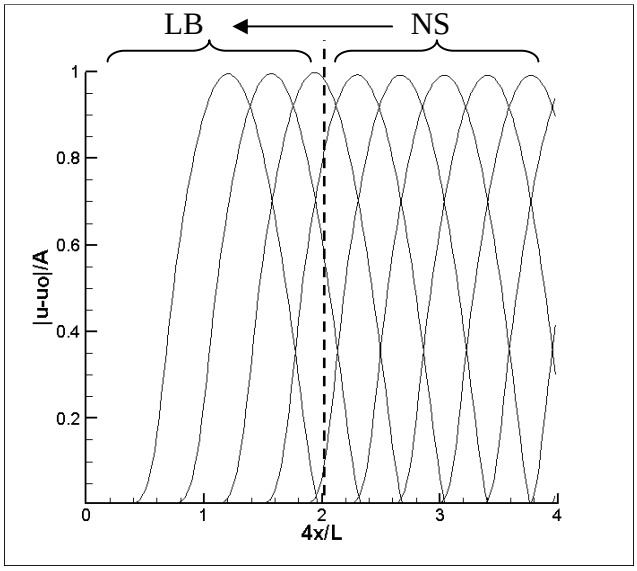

Figure 4.7 : Non-dimensional streamwise velocity along the channel at different time intervals using LB-NS coupled methodology

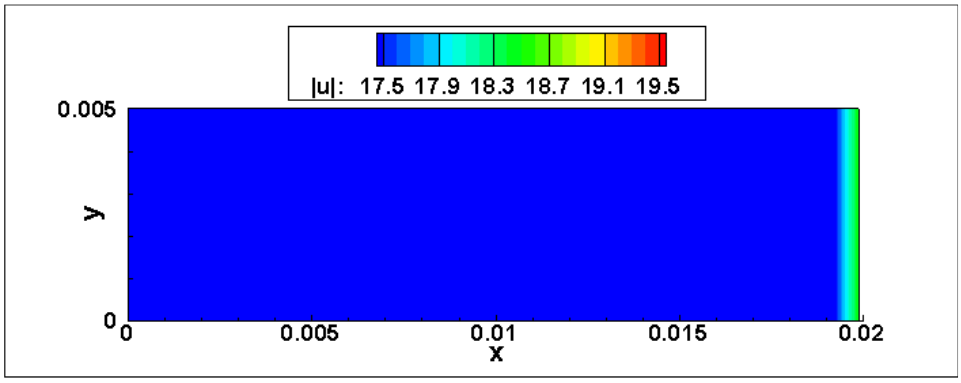

(a)

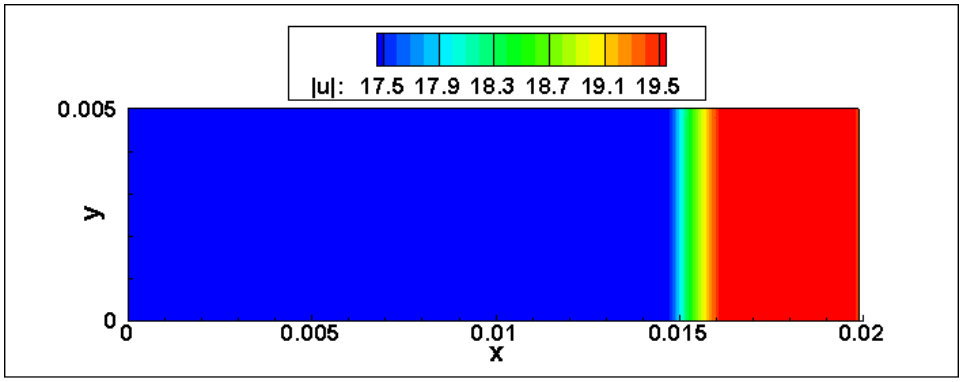

(b)

Figure 4.8: Streamwise velocity of the wave traveling from NS to LB domain at $u_o t/L$ = (a) 0.0 (b) 67.8 (c) 101.7 (d) 113.0 (e) 124.3 (f) 169.5 (g) 237.3

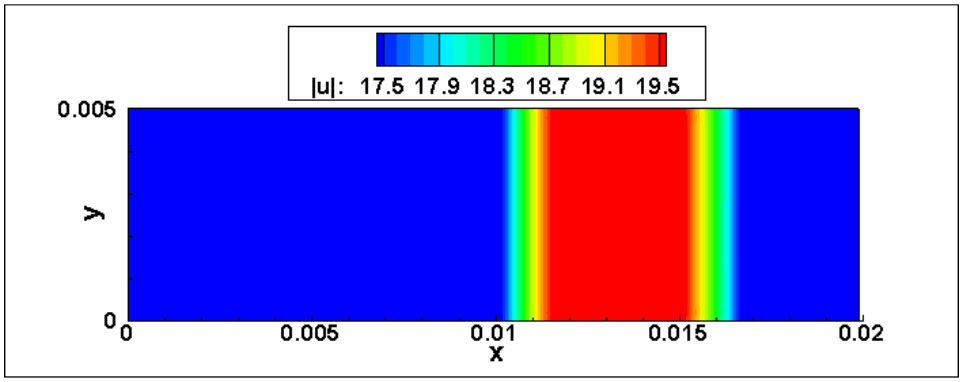

(c)

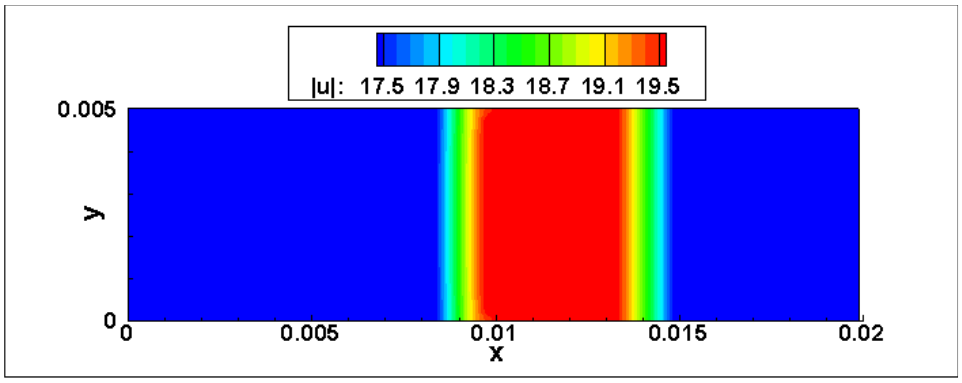

(d)

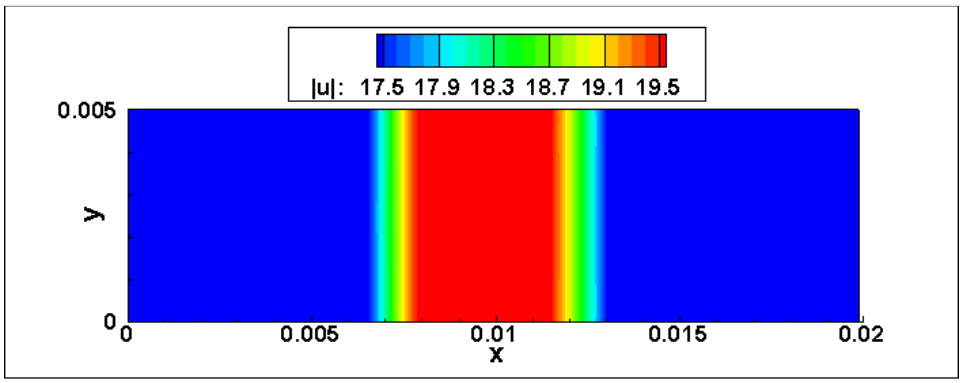

(e)

Figure 4.8 continued.

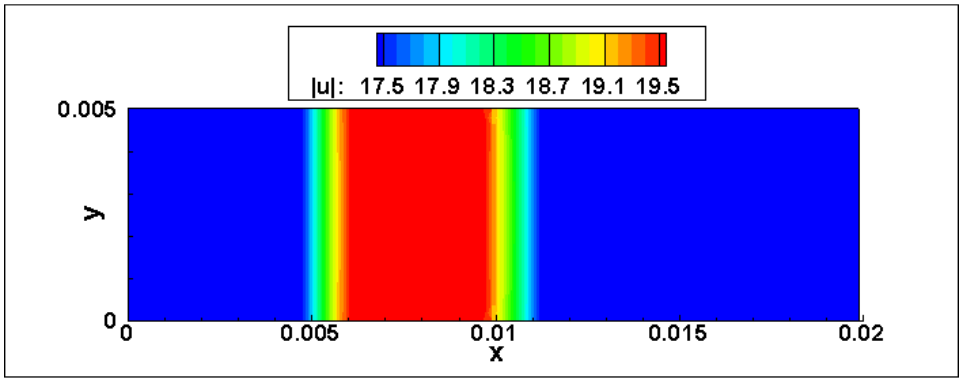

(f)

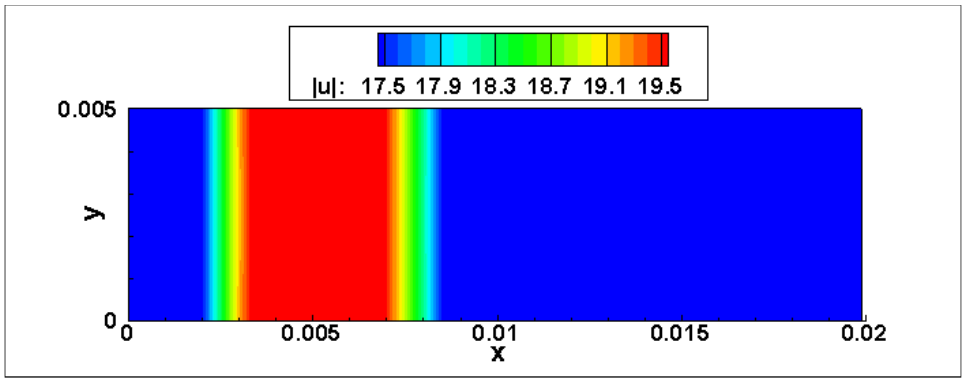

(g)

Figure 4.8 continued.

CHAPTER 5

RESULTS OF THE TWO-DIMENSIONAL COUPLED LATTICE BOLTZMANN-NAVIER-STOKES SIMULATIONS

Cylinder geometry is a good representation of the helicopter hub. Even at low Reynolds numbers, massive separation is observed in the wake of this bluff body. As mentioned in Chapter 1, the bluff body drag is a main contributor to the helicopter drag. Therefore, this case has been chosen to demonstrate the Lattice Boltzmann-Navier-Stokes (LB-NS) coupled methodology for an active flow control (AFC) application. A brief description of the Lattice Boltzmann (LB) concept was presented in Chapter 3. Several benchmark validations have been documented in Chapter 4 for the Lattice Boltzmann solver used in the present studies. Chapter 4 also shows the validations for the two-dimensional coupled LB-NS methodology. This methodology has been extended to flow problems involving active flow control, where the active flow control unit is modeled using the LB method and Navier-Stokes (NS) is used to simulate the rest of the domain. The results for one such active flow control application are presented in this chapter.

5.1 Navier-Stokes simulations for baseline flow past a cylinder without active flow control

The baseline, no AFC, case setup was chosen, to match the parameters from the experiments conducted by Glezer et al. [153], at a Reynolds number (based on the cylinder diameter) of 75500.

Baseline calculations are performed using the Navier-Stokes solver alone. For this case, a cylinder is placed in the center of an external flow domain. The computational domain size is 10 times the cylinder diameter of 0.0632m. Initially an extensive study is

performed on the baseline case in order to ensure that the grid and the numerical models used in the LB-NS coupled methodology are optimal values. An O-type grid with 294 points in the azimuthal direction and 90 grid points in the normal direction was chosen for the baseline cylinder case with no AFC. Spalart-Allmaras (SA) turbulence model is used in these studies. The flow is initialized with the free stream conditions.

Due to the high Reynolds number of the flow, unsteady flow is observed as expected. Flow separates behind the cylinder and vortex shedding is observed in the wake of the cylinder. Figure 5.1 shows an instantaneous snapshot of the vortex shedding in the wake of the cylinder. After several time step iterations, when the solution is periodic in time, the results are analyzed within one such shedding cycle. In order to obtain quantitative data from the simulation to compare with experiment, the results are time-averaged over one shedding cycle of the cylinder. On close inspection of the time-averaged result, the flow field shows that the separation behind the cylinder starts at an angle of around 94^{o} from the front stagnation point of the cylinder as shown in Figure 5.2 which also shows the time-averaged streamwise velocity field with the velocity vectors.

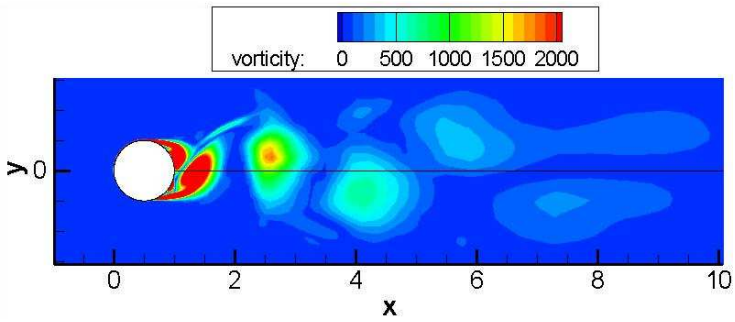

Figure 5.1: Instantaneous vorticity behind the cylinder at Re = 75500.

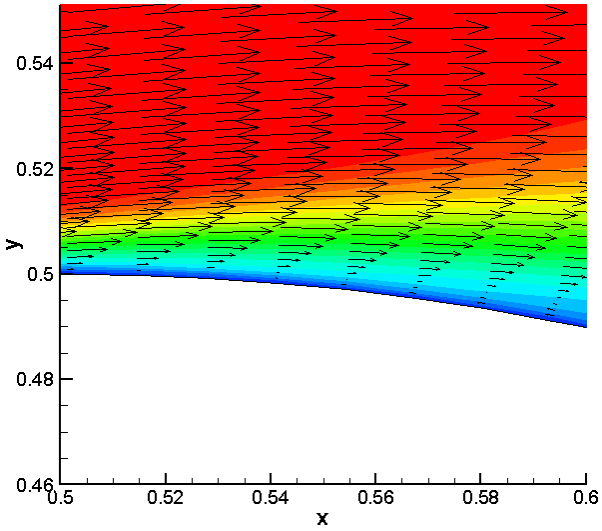

Figure 5.2: Time-averaged velocity distribution around the cylinder at Re = 75500 showing the separation point.

Figure 5.3 shows the distribution of the time-averaged pressure coefficient (C_p) around the surface of the cylinder. The angle theta (θ) is measured in degrees starting from the leading edge and moving clockwise around the cylinder. In experiment, a tripped case was also conducted. In this case, a thin wire was placed at $\theta = \pm 35^o$ to the freestream in order to obtain early transition to turbulence. The difference in C_p between experiment and computation may also be because the flow Re is close to the sub-critical Reynolds number and computations were made assuming the flow to be fully turbulent. The pressure drag coefficient (C_d) was calculated to be 1.19 which is well above the experimental C_d value of 0.95. This could be because the onset of separation is seen much earlier in computations (~94^o), due to lower turbulence levels, as compared to the delayed separation (~110^o) observed in experiment. Therefore, the same baseline calculations are performed with a two-equation turbulence model, κ–ω SST and compared with the present SA simulations.

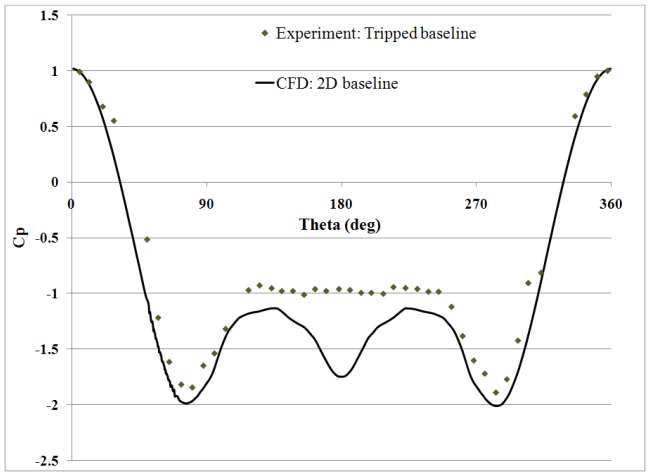

Figure 5.3: Time-averaged Cp comparison between experiment and simulation on the surface of the cylinder at Re = 75500.

However, the results from the κ–ω SST simulations did not show much improvement compared to the SA turbulence model data. The same separation point was observed. A comparison of the time-averaged Cp distribution between experiment and simulations is shown in Figure 5.4. The difference in pressure drag between the two turbulence models is less than 1%. Therefore, SA model is assumed sufficient for further calculations.

In addition to the above mentioned baseline simulations, validations have been performed for other Reynolds numbers using the Navier-Stokes solver alone. These have been documented in Appendix C in order to not detract from the present analysis.

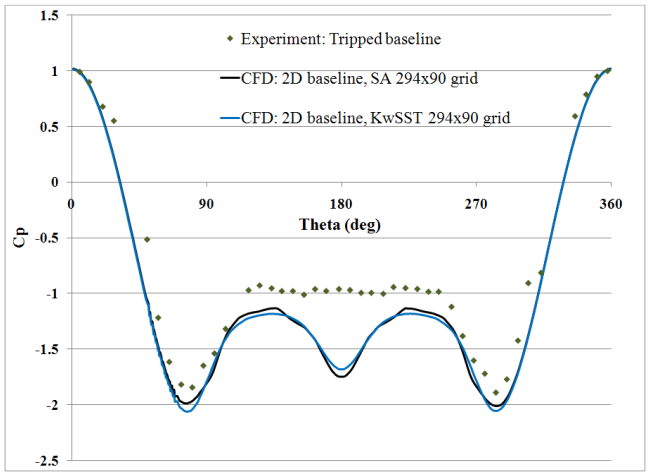

Figure 5.4: Cp comparison between experiment, SA simulation and κ–ω SST simulation.

5.1.1 Grid sensitivity studies

In order to capture the separation point accurately, the grid is refined to have 479 points in the azimuthal direction and the number of grid points in the boundary layer is also increased to have a total of 120 grid points in the normal direction. Baseline calculations are performed using this finer grid. Figure 5.5 shows that, increasing the number of grid points has not improved the Cp comparison between simulations and experiment. There is less than 3% difference between the pressure drag obtained from the coarse grid and that obtained from the finer grid. Therefore the subsequent two-dimensional studies, performed for the LB-NS coupled methodology are done using the 294x90 O-type grid with the SA turbulence model.

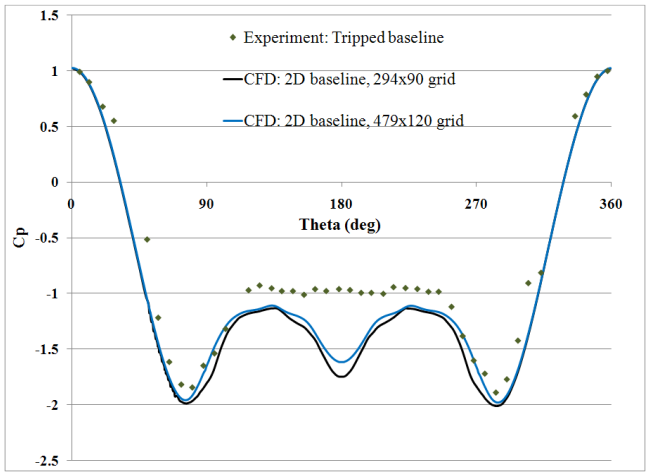

Figure 5.5: Cp comparison between experiment and simulations for two different grids: 294x90 and 479x120.

The difference in the Cp between experiment and the two-dimensional case is attributed to the strong three-dimensional nature of the largely separated flow in the wake of the cylinder. This is verified in the preliminary results for the three-dimensional LB-NS coupled simulations discussed in Chapter 6. However, initial LB-NS coupled simulations are performed in two-dimensions to validate the methodology.

5.2 Flow past a cylinder using the coupled LB-NS methodology for active flow control

For the same external flow conditions as the baseline case, two slots, each of width, b (same as experiment), and depth (nominal value is assumed) of 0.5mm and 1.264mm, respectively, was chosen for the geometry of the synthetic jet cavity. The slots are placed at an angle of 110^{o} to the freestream velocity. The synthetic jet cavity was modeled using the Lattice Boltzmann equations while the rest of the domain is modeled using the Navier-Stokes equations. Figure 5.6 shows a descriptive cartoon of the configuration. The dimensions in Figure 5.6 are not drawn to scale. The synthetic jet is

actuated sinusoidally by applying a time varying velocity boundary condition at the base of the cavity. The jet velocity is normal to the surface of the base of the synthetic jet cavity. Strouhal number of the jet is 2.5; set same as in experiment.

The comparison of the baseline and AFC time-averaged C_p distribution versus theta is shown in Figure 5.7. The use of synthetic jets only over the upper surface generated a large asymmetry in pressure over the upper and lower surfaces of the cylinder. Separation location moves aft as a result of synthetic jet actuation. The suction peak around 90 degrees is increased as a result, both in test data and simulations. This results in a smaller recirculation zone in the wake. Improved pressure recovery was observed in the aft region. The drag coefficient with the use of the synthetic jets is just 40% of the computed 3D baseline drag as a result.

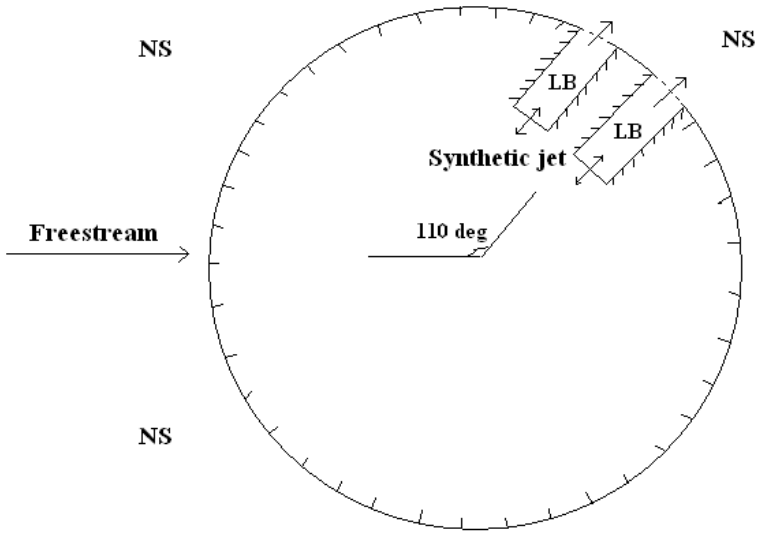

Figure 5.6: Sketch of the flow past cylinder configuration with the synthetic jet location (not drawn to scale).

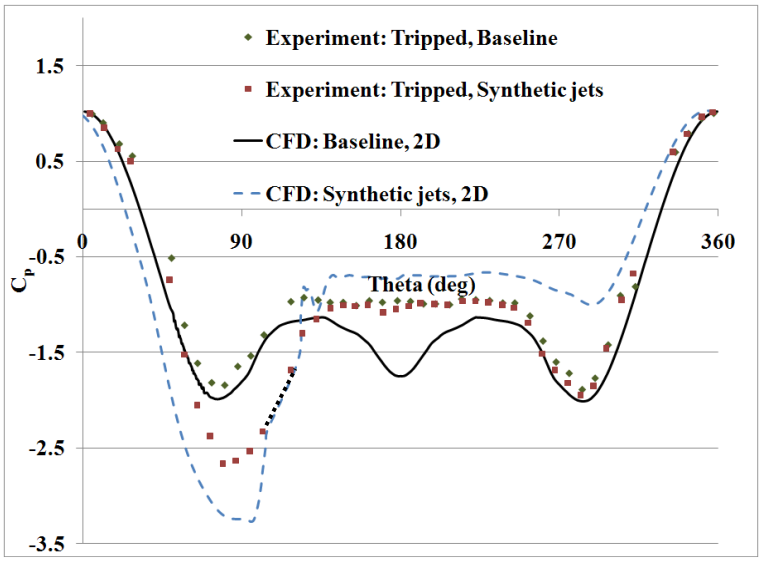

Figure 5.7: Time-averaged Cp distribution on the surface of the cylinder ay Re=75500 for the AFC case.

The effect of the synthetic jet can be studied by analyzing the time averaged flow field data. Figure 5.8 shows the time-averaged velocity field in the wake of the cylinder for (a) the baseline case (b) the active flow control case and (c) shows the non-dimensionalized streamwise velocity at the location x/D = 3.5 behind the cylinder. The asymmetry in the flow due to the addition of synthetic jets only on the upper surface of the cylinder is observed in Figure 5.8(b). The increase in the momentum of the flow due to the synthetic jets can be seen in Figure 5.8(c) which shows that the velocity deficit, on the upper side of the cylinder, at x/D=3.5 is less in the AFC case compared to the baseline case.

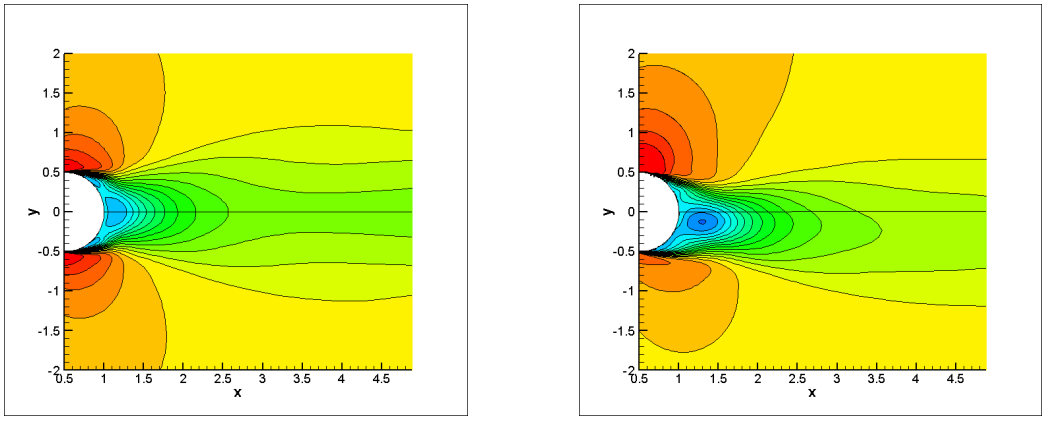

(a) (b)

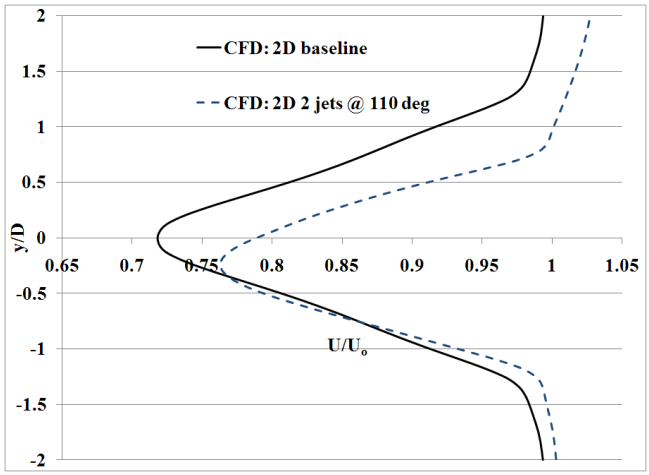

(c)

Figure 5.8: Time-averaged velocity field in the wake of the cylinder for (a) Baseline case (b) AFC case (c) Velocity deficit at x/D =3.5 (dashed line in (a) and (b)).

An instantaneous snapshot of the velocity contours is shown in Figure 5.9. It can be seen that high velocity pockets of flow are generated and convected on the upper side of the cylinder wake. These high pockets of velocity are ejected from the synthetic jet slots during the blowing part of the synthetic jet cycle. In effect, the high velocity increases the momentum of the flow on the upper side of the cylinder wake and delay the separation compared to the baseline flow as shown in Figure 5.10. Several instantaneous snapshots of the velocity field superimposed by streamlines are compared between

baseline (left column) and AFC (right column) case in Figure 5.10 in one shedding cycle of the cylinder. It can be observed that in all the snapshots, the separation point is delayed in the AFC case. During the suction part of the synthetic jet cycle, the low momentum fluid is drawn into the cavity. Since the synthetic jet slots are placed after the separation point, during the blowing part of the cycle, the high momentum fluid entering the NS domain, entrains the low momentum fluid behind the slot location. This again ensures the delay in separation point in the AFC case.

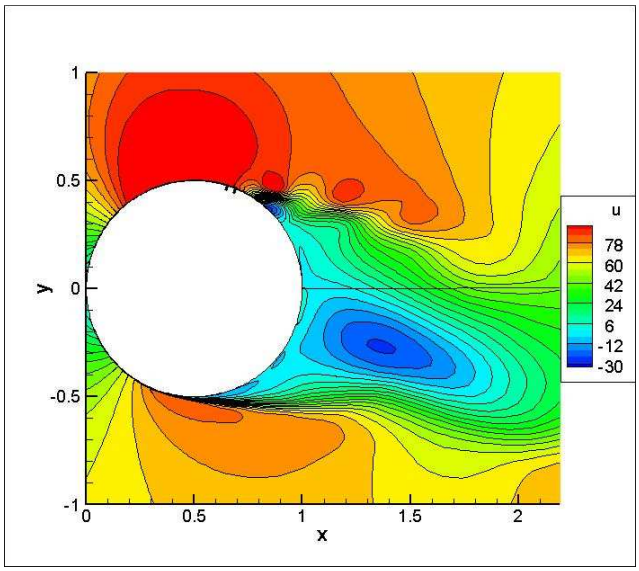

Figure 5.9: Intsntaneous velocity contours in the vicinity of the cylinder.

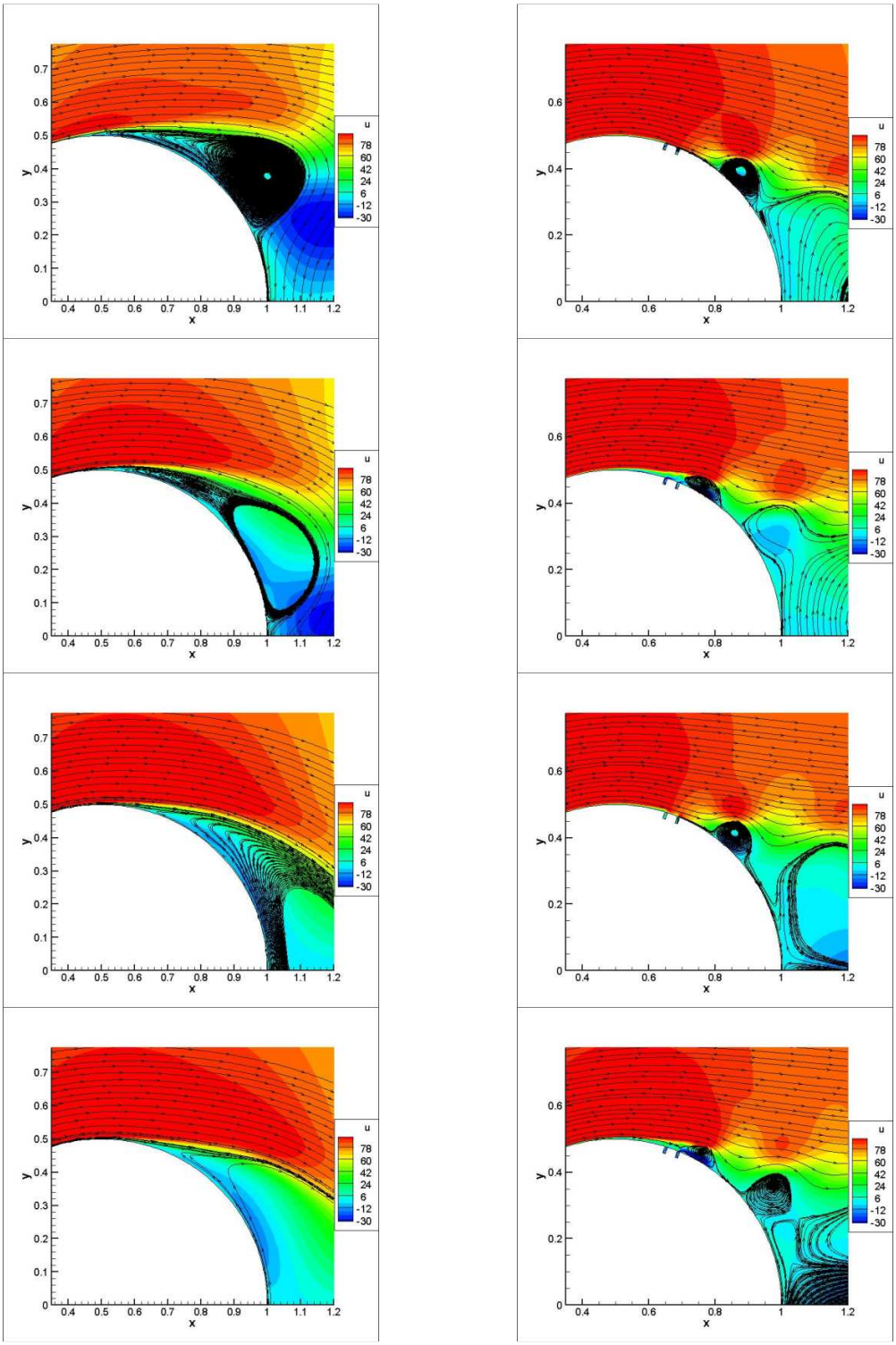

Figure 5.10: Comparison of instantaneous velocity field superimposed with streamlines near the synthetic jet between baseline (left column) and AFC (right column) case.

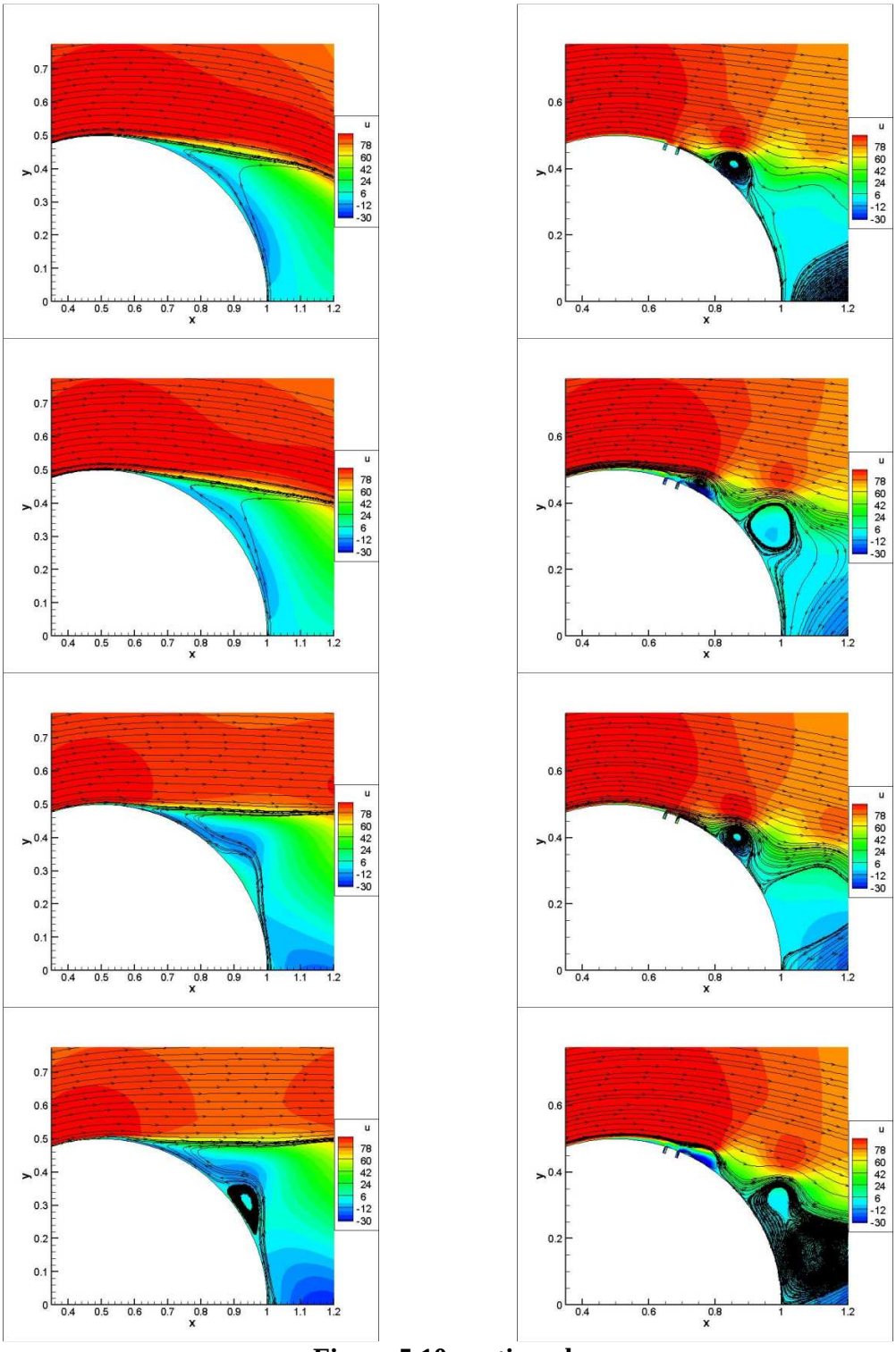

Figure 5.10 continued.

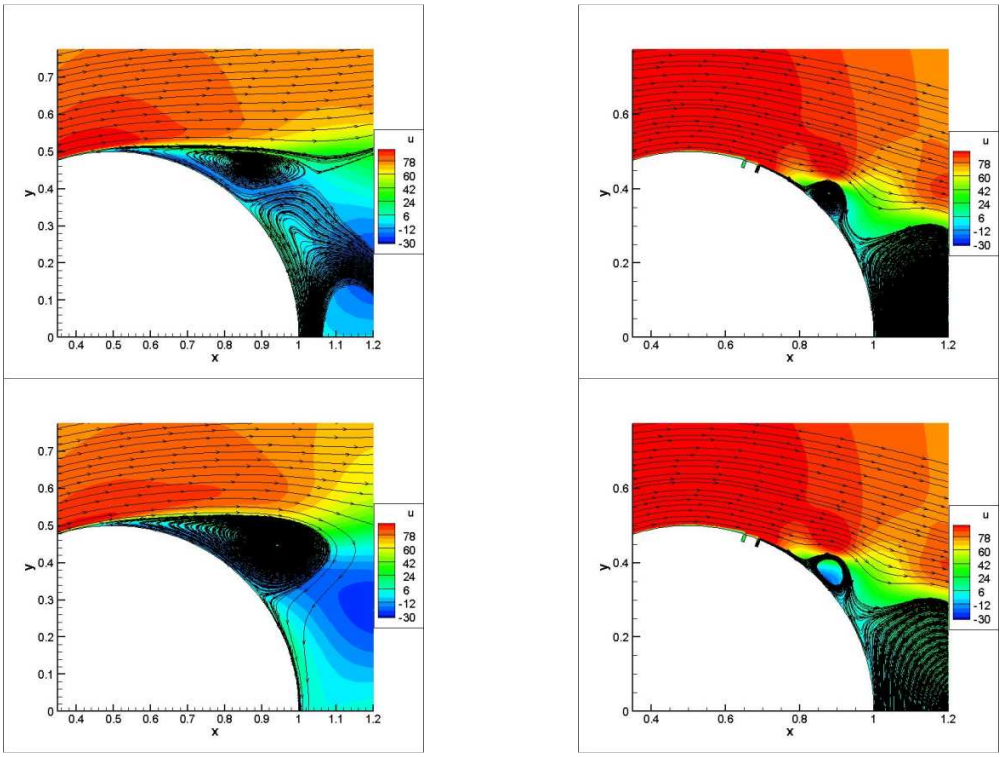

Figure 5.10 continued.

Analysis of the flow field inside the synthetic jet cavity is important in order to understand the physical phenomena behind drag reduction. Figure 5.11 shows the time-averaged pressure distribution inside the two synthetic jet cavities. The streamlines superimposed on this solution clearly shows the recirculation region inside the cavities. This physics would be lost if the cavities are not modeled in the simulation and the pressure peaks obtained using surface synthetic jet simulation would be more pronounced. Individually, instantaneous blowing and suction parts of the synthetic jet cycle are shown in Figure 5.12. It can be seen that the synthetic jet slot performs the pulsed cycle, while affecting the boundary layer close to the jet. However, this local change results in a global change in the flow field and ultimately reduces drag.

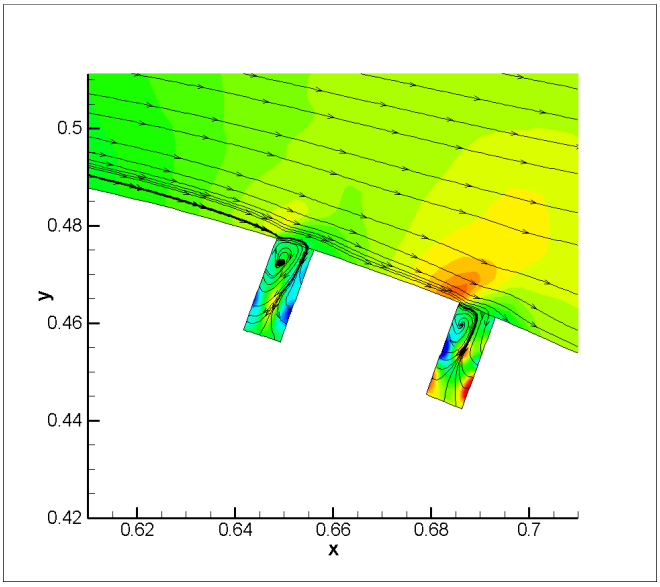

Figure 5.11: Time-averaged pressure distribution inside the synthetic jet cavities.

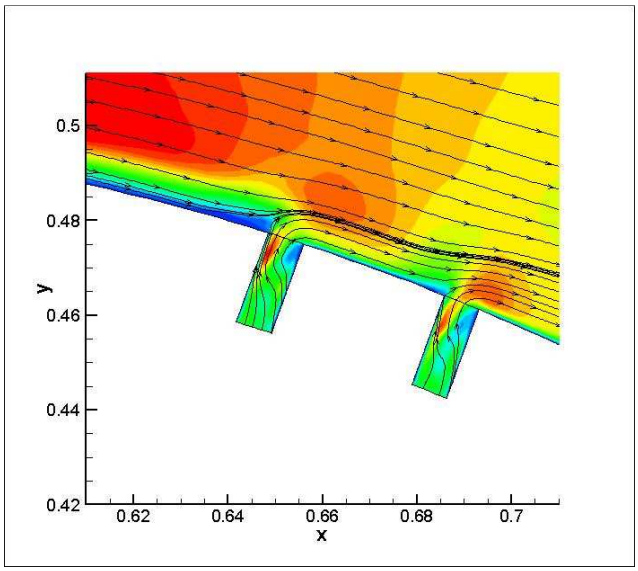

(a)

Figure 5.12: Instantaneous snapshots of the (a) blowing and (b) suction parts of the synthetic jet cycle.

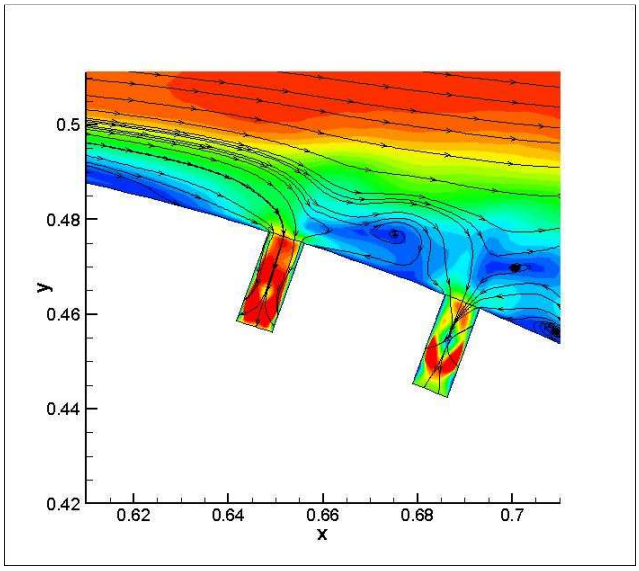

(b)

Figure 5.12 continued.

Single relaxation time (SRT) technique was used in the present calculations, instead of multiple relaxation time (MRT) [78], since the boundary conditions and the number of grid points in the LBE domain were sufficient to avoid any spurious variations in the conserved quantities as seen in the figures above. Also, as shown in the flow past a cylinder case in Section 4.1.3, SRT gives physical solutions for flows with low Reynolds numbers (~ O(100)). Since the local Reynolds number of the flow inside the synthetic jet was found to be around 213, SRT was sufficient for use in the present calculations.

The analysis of the time taken using only Navier-Stokes on the entire domain compared to using Lattice Boltzmann in the region near the synthetic jet shows that there is a 3% reduction in CPU time taken by using the latter. It must be noted that the present work only demonstrates the validity of the LB-NS coupled methodology for an AFC application. However, for a better saving on the computational time, it is proposed to use this coupled methodology for porous surface applications of AFC where there are several microscale cavities to model using LB [82].

CHAPTER 6

PRELIMINARY RESULTS OF THE THREE-DIMENSIONAL COUPLED LATTICE BOLTZMANN-NAVIER-STOKES SIMULATIONS

Two-dimensional studies of flow past a cylinder, documented in Chapter 5, showed a difference in the pressure distribution between experiment and computation in the wake of the cylinder. This difference was attributed to the massive separation behind the cylinder and the three-dimensional nature of the flow. In order to verify the validity of this statement, preliminary three-dimensional baseline computations are performed for flow past a cylinder. In addition, the ability of the coupled Lattice Boltzmann-Navier-Stokes (LB-NS) methodology is further explored in this chapter by performing preliminary three-dimensional coupled simulations using active flow control (AFC) techniques.

6.1 Baseline flow past a three-dimensional cylinder

As a starting point, baseline computations are performed for flow past a cylinder using a three-dimensional grid. The baseline, no active flow control, calculations are performed using the Navier-Stokes (NS) solver alone, for a Reynolds number of 75500, based on the cylinder diameter of 0.0632m. The AFC device was not needed, and there was no need to invoke the LB solver in the baseline studies.

The grid is generated by extrapolation of the two-dimensional 294x90 O-type grid in the third dimension with 30 grid points in this direction as shown in Figure 6.1. Spanwise periodicity is assumed beyond these surfaces. The initial conditions are set to

the freestream. The flow field is analyzed once the periodic vortex shedding is established behind the cylinder. The data is then time-averaged for one shedding cycle and along the span. The time-averaged pressure data from the three-dimensional simulations are in considerably better agreement with test data compared to the two-dimensional case, as shown in the Cp comparison in Figure 6.2. The drag coefficient calculated in the three-dimensional simulation, 0.9468, is within 1% of the experimental value of 0.95. It is thus concluded that the simulations agree well with experiment forming a baseline condition against which AFC studies may be compared.

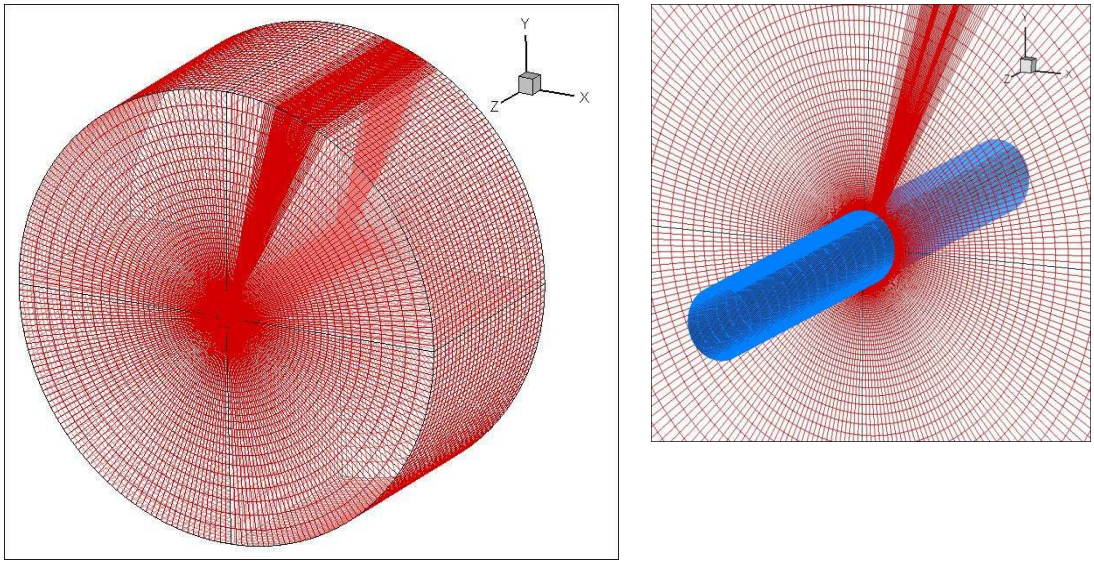

Figure 6.1: Grid of dimensions 294x90x30 used in the baseline three-dimensional flow past cylinder simulations.

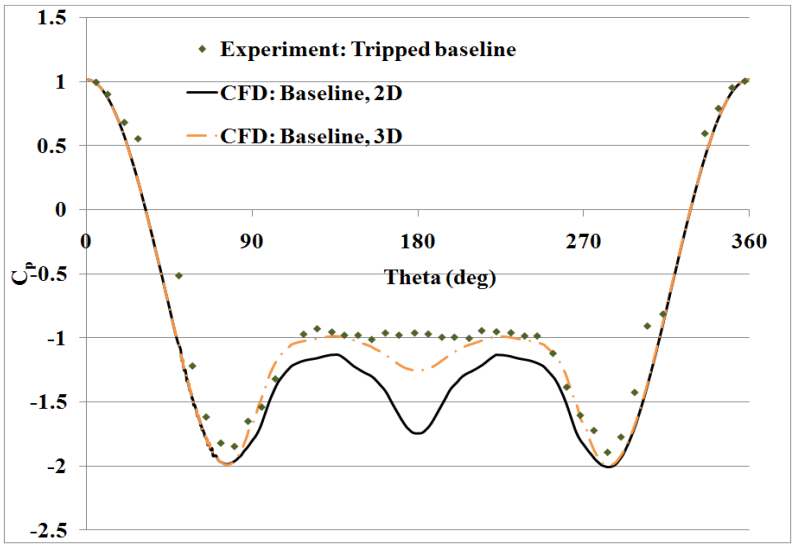

Figure 6.2: Comparison of Cp between experiment and two-dimensional as well as three-dimensional simulations.

The time-averaged and instantaneous vorticity contours for the three-dimensional flow past a cylinder simulation are shown in Figure 6.3. The streamlines in Figure 6.3(a) show the strong 3-D effect in the separated region of the flow discussed before. This three-dimensionality of the flow reduces the size of the separation bubble and allows for improved pressure recovery behind the cylinder compared to the 2-D case.

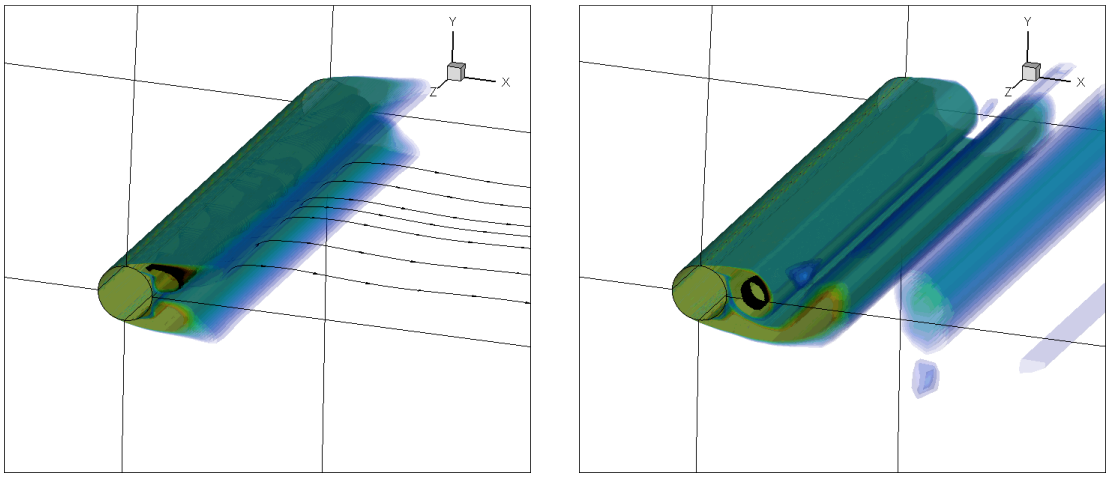

(a) (b)

Figure 6.3: Vorticity contours for the three-dimensional case of flow past a cylinder simulation (a) Time-averaged vorticity (b) Instantaneous vorticity contours.

A comparison of the pressure flow field between the 2-D and 3-D cases is shown in Figure 6.4. It can be observed that there is greater pressure recovery behind the cylinder in the 3-D compared to the 2-D pressure, as is also evident from Figure 6.2.

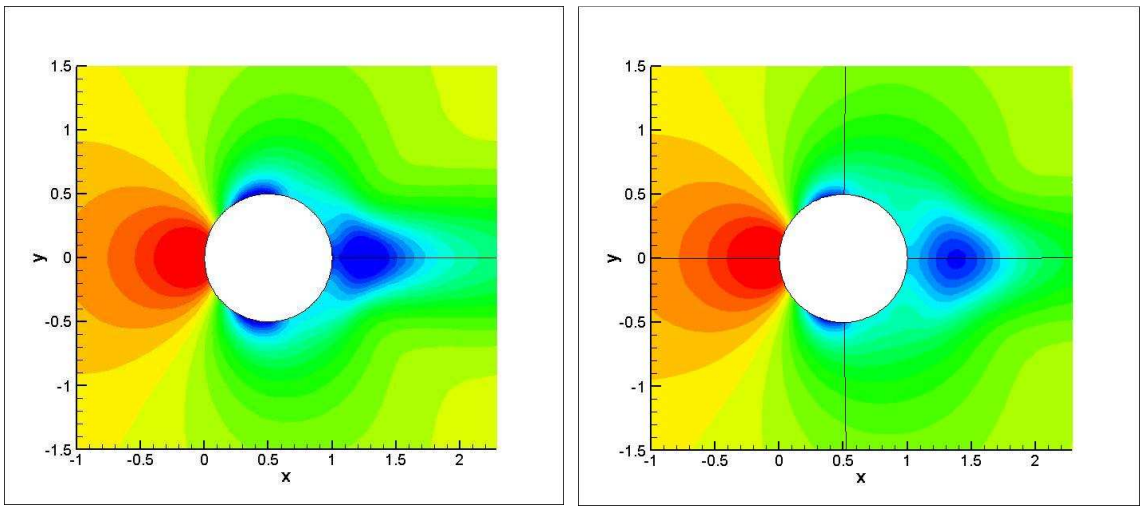

(a) (b)

Figure 6.4: Comparison of time-averaged pressure contours between baseline (a) 2-D and (b) 3-D flow past a cylinder.

Simulation of the same spanwise length as in experiment (~14D) would require a huge grid and immense computational resources. Therefore, the spanwise length simulated in the present studies is less than that in experiment. However, in order to compare the effect of the spanwise length on the flowfield, simulations have also been performed for a grid with 5 nodes in the spanwise direction. A comparison of the time-averaged Cp distribution between 5 and 30 spanwise stations is shown in Figure 6.5. It can be observed that there is no significant difference in the pressure distributions between the two simulations.

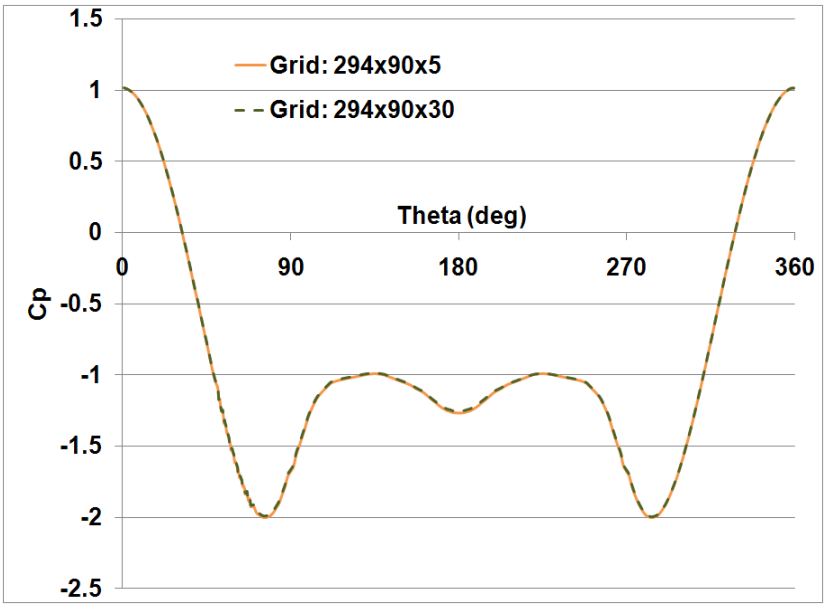

Figure 6.5: Comparison of time-averaged surface pressure distribution between 3-D baseline cylinder simulations with different spanwise lengths.

6.2 Active flow control using the coupled Lattice Boltzmann-Navier-Stokes methodology for flow past a cylinder

In order to break the coherence of the flow shown in Figure 6.3, active flow control has again been applied to the three-dimensional flow similar to that demonstrated in the two-dimensional studies. The configuration for the present 3-D studies is shown in Figure 6.6. The design has been obtained by extending the 2-D grid used in the active flow control studies in the third dimension with 30 spanwise stations. The synthetic jets are activated over specified spanwise locations as shown in Figure 6.6. Spanwise adjacent synthetic jets are set to be completely out of phase in order to break the coherence of the flow observed in the baseline 3-D studies. At each spanwise location, two synthetic jet slots are placed at approximately 110^{o} aft of the front stagnation point of the cylinder, similar to the 2-D setup.

Figure 6.7 shows the time-averaged Cp distribution on the surface of the cylinder. The phase-lagged synthetic jets show a suction peak in the pressure at the location of the jets and pressure recovery is observed behind the cylinder. The drag obtained for this case is 0.87 which is 8.5% less than that obtained from the baseline 3D simulation.

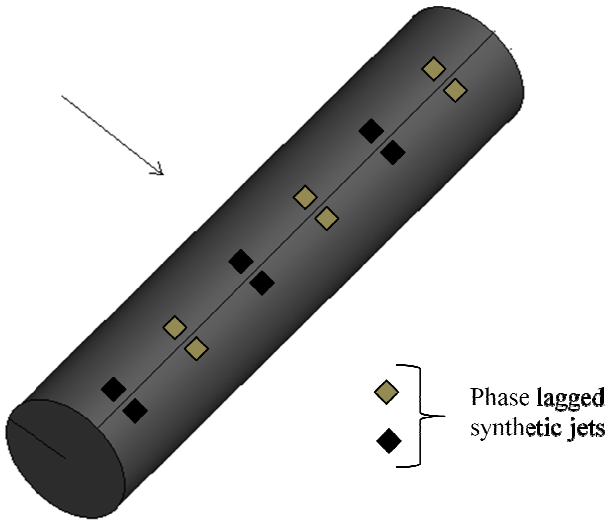

Figure 6.6: Active flow control configuration for the three-dimensional coupled Lattice Boltzmann-Navier-Stokes study.

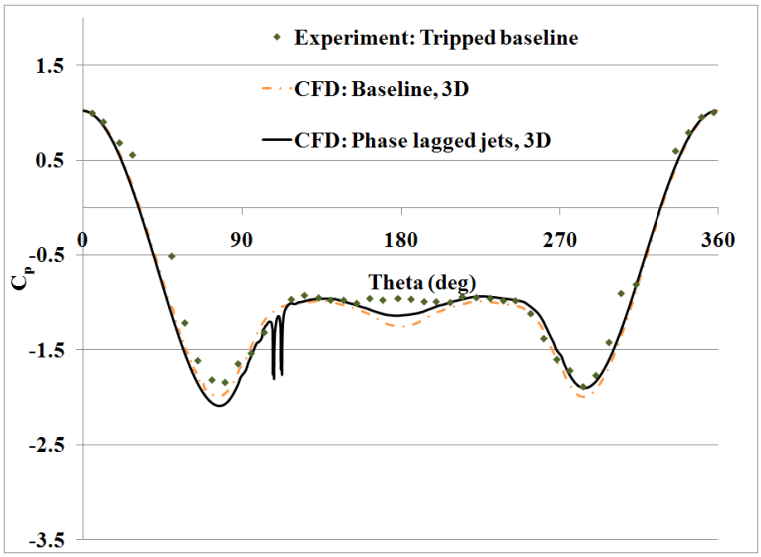

Figure 6.7: Comparison of time-averaged Cp distribution on the surface of the 3D cylinder between experiment and baseline and synthetic jet simulations.

Analysis of the flowfield was performed in order to observe the synthetic jet action. High pockets of velocity are observed to emerge alternatively from the spanwise adjacent jets as seen in the instantaneous Mach number contours in Figure 6.8. The coherence of the flow is broken due to the lag in the suction and the blowing phase between the jets.

In this 3-D study, the slot locations (azimuthal and spanwise) were chosen in an adhoc fashion and only an 8.5% reduction in drag over the baseline no control case was achieved. An optimization study dealing with spanwise placement distance, azimuthal locations, and frequency of the jets is needed to realize further drag reduction. This approach also lends itself to a collection of slots mimicking jets issuing out of a porous surface.

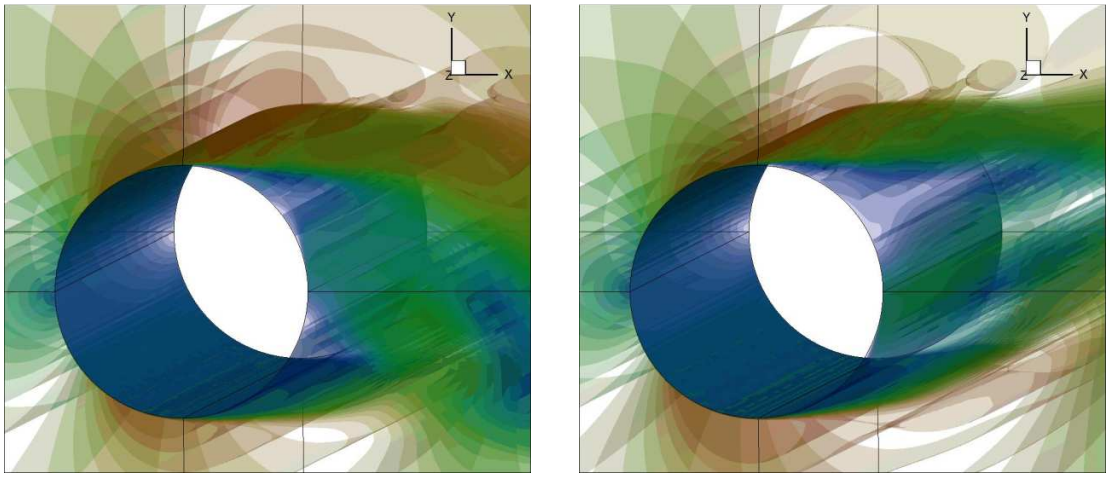

(a) (b)

Figure 6.8: Instantaneous Mach number contours around the 3-D cylinder with phase-lagged synthetic jets.

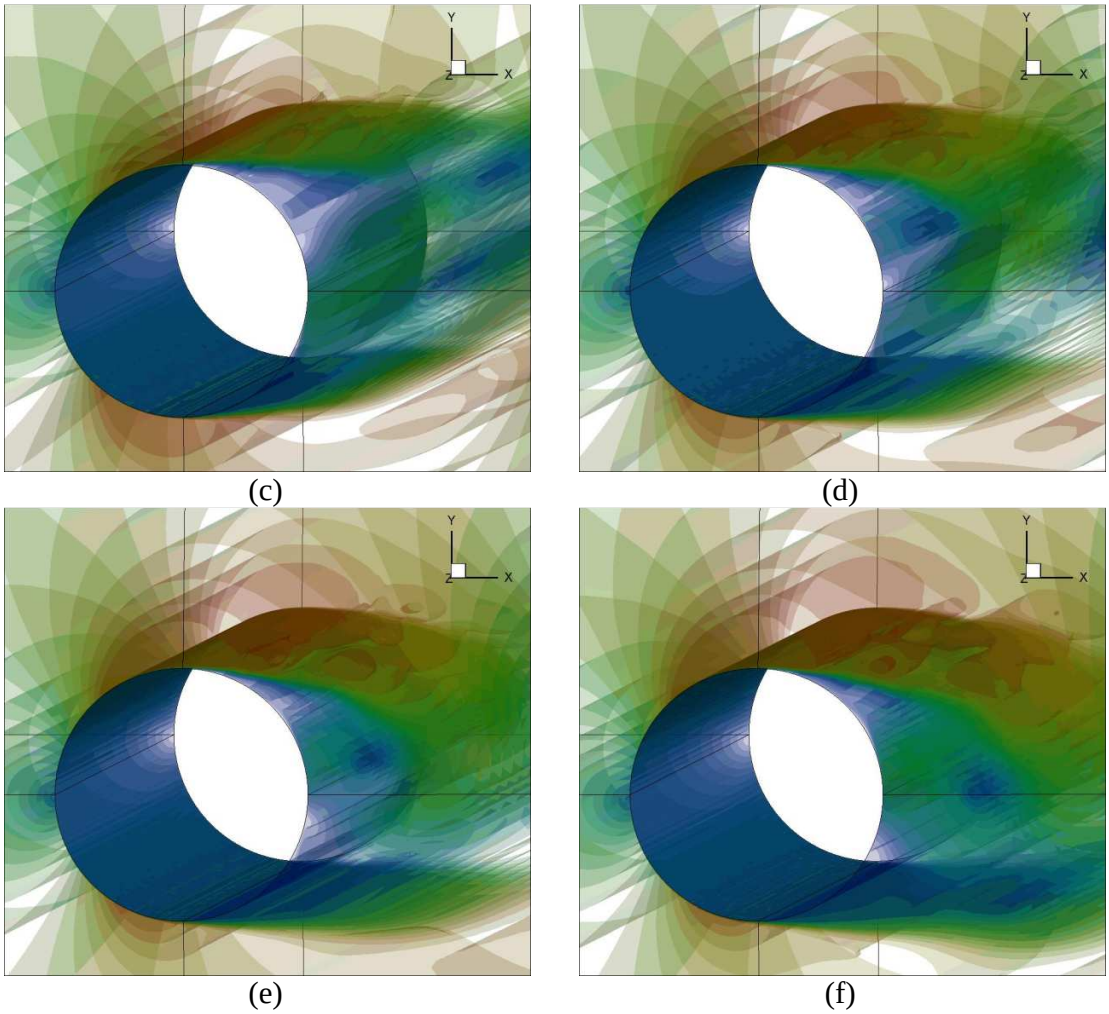

(c) (d)

(e) (f)

Figure 6.8 continued.

CHAPTER 7

CONCLUSIONS AND RECOMMENDATIONS

In the present work, a unique method to couple a Lattice Boltzmann (LB) and a Navier-Stokes (NS) solver has been developed. This coupling requires several steps. An existing Lattice Boltzmann equation (LBE) solver has been modified to convert microscopic probability density distribution to macroscopic flow field quantities so that one can derive each quantity accurately. All the conversions have been justified and mathematically shown. An existing NS solver has also been modified to allow interaction with the LBE solver. The exchange of information at the interface has been implemented as an interface boundary condition used in NS solvers. The present studies show the first application of the coupled methodology for active flow control (AFC) of bluff bodies.

A summary of the work done is listed below:

An existing three-dimensional NS solver has been used to study the physical mechanisms behind drag reduction of bluff bodies, representative of helicopter components, using AFC techniques. One of the cases studied was the flow past a hump model which has extensive experimental data for pressure and velocities at several locations in the separated region. Baseline study with no flow control has been performed and successfully validated against experimental data. A good comparison between pressure has been observed except in the separated region where computations predict higher pressure. The flow field has been studied and it was concluded that the reason for the discrepancy between CFD and experiment in the pressure and velocity data in the separated region is due to the prediction of higher Reynolds stress in computations.

Following this, active flow control simulations have been performed. These include steady suction and synthetic jet actuation. The results showed the pressure comparisons between CFD and experiment to have a trend similar to that of the baseline. In each case, the drag reduction has been compared to the baseline computational case and conjectures have been made on the mechanism behind this reduction in drag. It is concluded from these studies that AFC can successfully be used to reduce drag compared to the baseline no AFC case. Additional reduction in drag was observed in the case of the synthetic jet compared to the steady suction case.

In addition, the amount of power required to sustain the active flow control device is assessed alongside the power saved based on the amount of profile drag reduced. Power analysis was performed between suction and synthetic jet cases. It was found that for the same input in power, synthetic jets create additional reduction in drag. It is therefore concluded that synthetic jets are more efficient and advantageous for use as drag reduction devices compared to their steady counterparts.

Based on recommendations of the above NS studies, active flow control using synthetic jet devices has been chosen for follow up studies of drag reduction on massively separated bodies like cylinders. Due to the incompressible nature of the flow surrounding these small synthetic jet devices, LBE are used in such regions. LBE better resolve the flow phenomena in these small length scale regions. However, using LBE in the whole external domain would be computationally expensive since the grid spacing in the LBE solver is of the order of the mean free path. Therefore, a coupled Lattice Boltzmann-Navier-Stokes (LB-NS) methodology has been developed.

An existing LBE solver has been extensively validated against benchmark problems like the Poiseuille flow, Couette flow and flow past a cylinder in a two-dimensional channel. The LBE solver was concluded to be of second order accuracy using grid sensitivity studies for the Poiseuille flow.

A comparison between NS and LB solvers was performed for flow past a cylinder in a channel. In order to compare the non-dimensional coefficients between the two solutions, a momentum-exchange method of force calculation was successfully implemented in the LBE solver. It is concluded that this method of force calculations showed good agreement between drag and Strouhal number values of simulation and benchmark data.

Equations have been developed to convert the values of the probability distribution function in the LBE solver to the macroscopic values of density and velocities to be used in the NS solver. Conversion of NS density and velocity to LB probability distribution function has been implemented in the LBE solver. An accurate calculation of the physical time step involved in the LBE solver has been shown. Correct exchange of the flow quantities between LB and NS domains has been implemented and this coupled methodology has been successfully validated for a wave travelling to and from the LB domain to the NS domain. It was seen that there was no abrupt change in the wave shape at the interface between the two domains. It is therefore concluded that the implementation of the LB-NS coupled methodology was correct.

This coupled LB-NS methodology is used for an AFC case of flow past a cylinder with synthetic jets located in the aft region of the cylinder. The synthetic jet slots are simulated using the LB solver while the external domain is solved using the NS

equations. The NS solver is separately validated for the baseline case of a flow past a cylinder. Extensive comparison of computed and experimental pressure data has been performed using different turbulent models. It is concluded that the difference in the pressure between experiment and simulations is due to the strong three-dimensional nature of the separated region in the wake of the cylinder. Grid sensitivity studies have been performed to verify the accuracy of the grid used for the AFC case in the next stage.

Coupled LB-NS AFC calculations have been performed and compared with the baseline CFD data. The flow field is analyzed and effect of the synthetic jet slot on the external flow is studied. It was observed that the separation is delayed in the cylinder due to the use of synthetic jets and reduces the drag by almost 40 percent compared to the baseline case. Therefore, the reduction in drag due to the AFC device is due to the addition of momentum due to the synthetic jet devices. The overlap of the LBE and NS domains is limited to the laminar sublayer of the flow. Therefore, it is concluded that the LBE solver without turbulence modeling was sufficient for the present analysis.

Due to the three-dimensional nature of the flow, efforts were made to conduct preliminary three-dimensional baseline NS only studies for the baseline flow past a cylinder. The studies showed better comparison with experimental data compared to the two-dimensional case, leading to the conclusion that regions of large separation are computationally better resolved with 3-D simulations.

Efforts to actively break up the 3-D structures have been made using the 3-D coupled LB-NS methodology. Out of phase synthetic jet slots are placed in the aft of the cylinder and the resultant flow field is studied again using the coupled LB-NS methodology in three-dimensions. The results are hoped to show the viability of using

synthetic jets to break 3-D coherence of the flow with the use of out-of-phase synthetic jets.

7.1 Conclusions

Based on the current studies, the following conclusions may be drawn:

- The wave travelling between the NS and LB domains does not show reflections at the interface between the two solvers. This shows that although NS and LB solvers model the flow using different methods, they could be made compatible by the correct use of the microscopic to macroscopic conversion.
- NS and LB model two separate phenomena with different reference lengths and different time scales, but they could be connected using the present coupled methodology.
- Both LB and NS individually model Strouhal number and lift and drag coefficients accurately. Interestingly, when coupled, they model experiment and unsteady flow phenomena well.

In summary, it is hoped that the present work is a stepping stone for future work where standalone NS and LB equations do not capture the physics of the phenomena.

7.2 Recommendations

Based on the present studies and conclusions, the following recommendations are made for future research:

- Grid sensitivity studies have been performed separately for the LB and NS solvers. Temporal and grid convergence for the combined LB-NS solver could be performed.

- The present studies demonstrate the validity of the LB-NS coupled methodology for 2-D as well as 3-D computations. For this purpose, a simple cylinder geometry was chosen. Complex geometries could be chosen for the 3-D computations for AFC cases to see the break in coherence of the flow.
- The coupled methodology could be extended for application in sweeping jets. The LBE formulation could be used to solve the flow in the actuator and NS for the rest of the domain. Sweeping jets have been shown to reduce drag substantially and enhance lift.
- The coupled methodology could be implemented for the case of a porous wall where the porous cavities could be modeled using LBE and the external domain is simulated using NS equations. This case would clearly show the efficiency and computational advantage of using a coupled LB-NS formulation instead of a pure NS only computation.

APPENDIX A

CHAPMAN-ENSKOG EXPANSION

In order to show that the Boltzmann equation can be used to describe fluids, the Navier-Stokes equations are derived by a procedure called Chapman-Enskog expansion, or multi-scale analysis. It relies on the Knudsen number *Kn*, which is the ratio between the mean free path length (λ), and the characteristic shortest scale of the macroscopic system that needs to be considered (L). The Knudsen number has to be less than one, for the treatment of the fluid as a continuous system:

$$Kn = \frac{\lambda}{L} \tag{A.1}$$

For the derivation, a splitting of the Boltzmann equation into different scales for space and time variables (or a hierarchy of these) is performed. It is based on the expansion parameter ϵ for which the Knudsen number *Kn* will be used. The expansion is done in a way, that each scale models a process of interest. Usually the expansion is truncated after terms of second order. For the time variables, the following representation is chosen:

$$t = \epsilon t_1 + \epsilon^2 t_2 \tag{A.2}$$

The time *t* represents the very fast local relaxations in a fluid by collisions. Sound waves, as well as advection, are of the scale t_1, and considerably slower than the local relaxations. Still, these are faster than diffusion processes, that are of time scale t_2. Only one spatial expansion has to be considered, giving the following expansion of first order:

$$\vec{x} = \epsilon \vec{x}_1 \tag{A.3}$$

This is due to the fact, that advection and diffusion both are considered in similar spatial scales x_1. The representation of the differential operators is similar:

$$\frac{\partial}{\partial x_a} = \epsilon \frac{\partial}{\partial x_a}$$
$$\frac{\partial}{\partial t} = \epsilon \frac{\partial}{\partial t} + \epsilon^2 \frac{\partial}{\partial t} \tag{A.4}$$

For a consistent expansion, the second order terms in space are also necessary. The moment equations of f are directly expanded to a sum of the form:

$$f = \sum_{n=0}^{\infty} \epsilon^n f^n \tag{A.5}$$

Furthermore, it is assumed that the time dependence of f is only caused by the variables ρ, $\vec{u}$ and T. Expanding Equation (3.2) in both space and time up to second order yields the following equation:

$$\epsilon \frac{\partial f}{\partial t_1} + \epsilon^2 \frac{\partial f}{\partial t_2} + \epsilon u_a \cdot \frac{\partial f}{\partial x_a} + \frac{1}{2} \epsilon^2 u_a u_b \frac{\partial^2 f}{\partial x_a \partial x_b} = \Omega(f^0) + \epsilon \frac{\partial \Omega(f^1)}{\partial f} \tag{A.6}$$

Note that f^0 is a Maxwell distribution, and as such, due to the definition of the BGK collision approximation in Equation (3.7), $\Omega(f^0)$ is zero. The three scales from $\mathcal{O}(\epsilon^0)$ to $\mathcal{O}(\epsilon^2)$ can be distinguished in Equation (A.6), and are separately handled. From there on, subsequent expansions of the conservation equations can be performed. Expanding mass up to second order gives an equation of the form:

$$\epsilon \hat{m}_1 + \epsilon^2 \hat{m}_2 \tag{A.7}$$

As ϵ is the Knudsen number, it is necessarily larger than zero and so are the terms $\hat{m}_1$ and $\hat{m}_2$ that represent the expansions for first and second order, respectively [148].

For first order terms of Equation (A.6), using a mass and momentum of zero, results in the following two equations:

$$\frac{\partial \rho}{\partial t_1} + \rho \frac{\partial u_a}{\partial x_{1a}} = 0$$
$$\frac{\partial \rho u_a}{\partial t_1} + \frac{\partial \int u_a u_b f^0 d\vec{u}}{\partial x_{1b}} = 0 \tag{A.8}$$

The continuity equation is already recognizable. When the integral of the second equation is analytically performed, it can be replaced by $\rho u_a u_b + \rho T \delta_{ab}$:

$$\frac{\partial \rho u_a}{\partial t_1} + \frac{\partial \rho u_a u_b}{\partial x_{1b}} + \frac{\partial \rho T \delta_{ab}}{\partial x_{1b}} = 0 \tag{A.9}$$

Equation (A.9) may be recognized as the Euler equations for inviscid flows without dissipation. To get the Navier-Stokes equations from here, the second order equations have to be considered. These are much more complicated to handle, as both equilibrium and non-equilibrium levels are needed. Still, using first order conservation terms of zero, and restoring the continuous form of the equations, the Navier-Stokes equations emerge. This is possible as terms of $\mathcal{O}(u^3)$ can be neglected, due to the assumption of small velocities for the expansion. The expansion also yields the equation for the calculation of the viscosity from the LBM parameters. For more details refer to [145][148].

APPENDIX B

NUMERICAL STUDIES USING NAVIER-STOKES EQUATIONS

B.1 Introduction

Several studies have been done to validate the Navier-Stokes solver, used in the coupled Lattice Boltzmann-Navier-Stokes studies by the present researchers. These validations have been documented in detail in Ref. [133]. In order to assess the ability of Navier-Stokes solvers to capture large separated flows as well as their ability to predict the drag when using an active flow control device, a flow over a hump model is studied.

The main objective of the present research is to study the physical mechanisms behind the drag reduction caused due to the use of active flow control devices and to correctly model the flow field in such problems. In particular, the present work is applied to configurations representative of helicopter components. To this effect two cases were chosen: (a) Flow past a NACA 0036 airfoil (b) Flow over a hump model. The NACA 0036 airfoil is representative of a helicopter hub while the hump model is representative of the helicopter pylon. Drag reduction studies have been performed for these configurations using active flow control techniques [124]-[130]. The mechanism behind drag reduction for these cases was studied. Detailed information on the calculation and analysis for the NACA 0036 airfoil cases was documented in Ref. [130]. The analysis of the flow over the bump is described below.

B.2 Flow over a hump

A CFD validation workshop on synthetic jets and turbulent separation control (CFDVAL2004) (Ref. [142],[143]) was held in March 2004 in Williamsburg, VA. The

purpose of this workshop was to assess the current capabilities of different classes of turbulent flow solution methodologies to predict flow fields induced by synthetic jets and separation control. The 'Flow over a Hump Model' case chosen for the present validations is one of the three cases documented in this workshop. As a result, a large body of simulations is available for this configuration, in addition to test data.

The geometry of the hump system and the grid used in the present studies is shown in Figure B.1. The grid is non-dimensionalized with respect to the chord and extends up to 6.39 chords upstream to model the developed boundary layer in actual experiment and extends approximately 4 chord lengths downstream of the hump. The top wall of the geometry has been adjusted to approximately account for side plate blockage found in the experiment. The hump surface has a synthetic jet unit (cavity) attached to it at 65% chord, for use in the active flow control test cases. The slot height is 0.00187 times the chord. Slip-wall boundary conditions were applied at the bottom of block 4. The upper surfaces of block 1 and block 2 were modeled with a slip-wall boundary condition to account for wind tunnel blockage effect. Both the external flow and the flow within the cavity were modeled. The grid dimensions of blocks 1, 2, 3 and 4 are 25x109, 397x109, 61x33, 61x81 respectively.

In the experiment and the present study both, the freestream Mach number was 0.1 and the Reynolds number based on the 420 mm chord of the hump was 0.936 Million. The pressure and temperature at the inlet was set to 101325 Pa and 298 K, and the back pressure at the exit was set to 101271.3 Pa. Additional details of the test are available in Ref. [142]. The κ-ω SST turbulence model was used to examine the separated region by the present researcher.

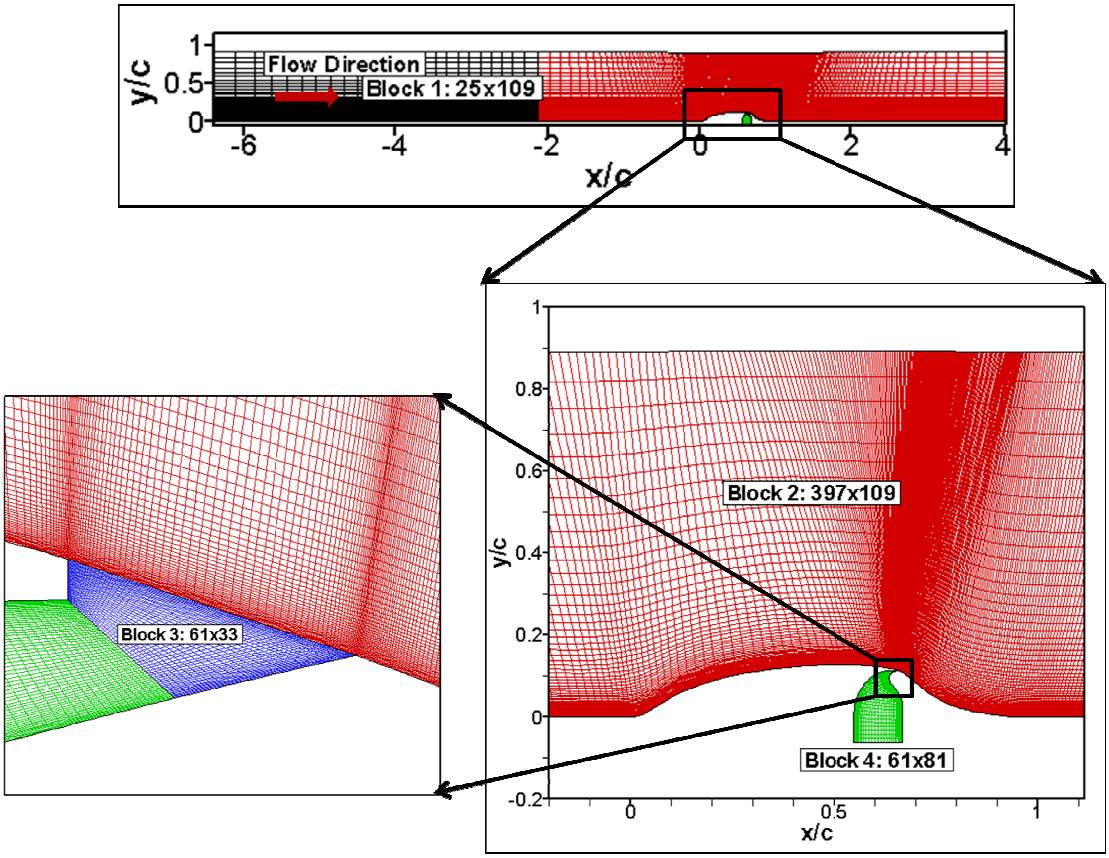

Figure B.1: Grid and geometry used in the flow over hump test case

B.2.1 Baseline no flow control case

First, the baseline case was modeled with the bottom wall of the cavity. This represents the baseline case with no flow control. The flow separates due to the adverse pressure gradient in the concave section in the aft of the hump geometry. Figure B.2 shows comparisons between computed and measured surface pressure distribution (C_p) over the hump. Good agreement is seen between the measurements and the predictions. The difference between the distributions can be observed in the separated region, aft of the hump. Figure B.3 shows the comparison of the separated flow region, aft of the hump, between experiment and the present simulations. Separation was found to start

around 0.66 chords in CFD against 0.66-0.67 chord of experiment. The reattachment point predicted by CFD is around 1.24 chords which is much further than 1.11 chord predicted by experiment. Most CFD data documented at the Williamsburg Workshop had a similar discrepancy. Therefore, κ-ω SST turbulence model predicts the onset of separated comparable to that found in experiment, however it predicts delayed reattachment. This may be due to the low levels of turbulent viscosity predicted by the κ-ω SST turbulence model in the separation region as shown by the non-dimensionalized Reynolds shear stress $\overline{u'v'}$, in Figure B.4. Although the qualitative behavior of the Reynolds shear stress is good with experiment, the magnitude is underpredicted. Figure B.5 shows the comparison of non-dimensional streamwise (u/U_∞) and cross stream (v/U_∞) velocities between experiment and computation for different locations in the separated region. Very good agreement between measured and computed values is observed qualitatively.

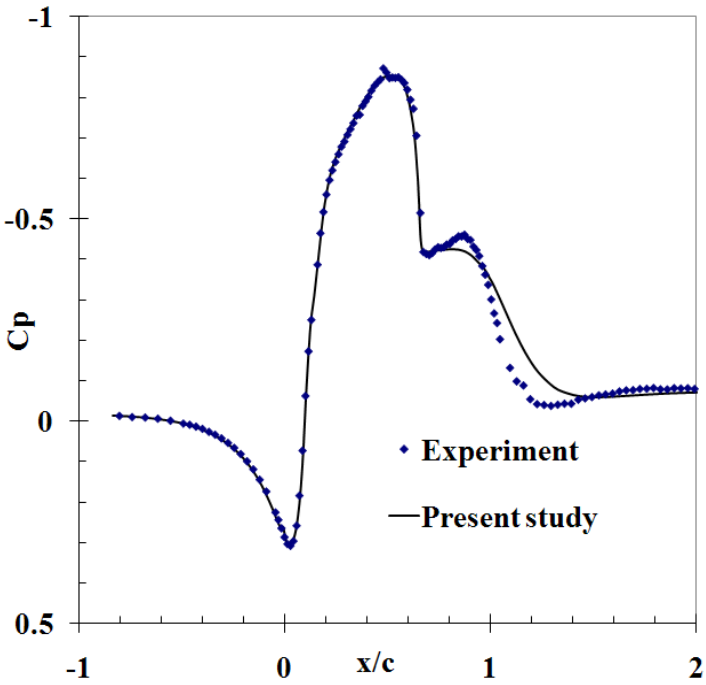

Figure B.2: Baseline Cp distribution comparison between experiment and computation.

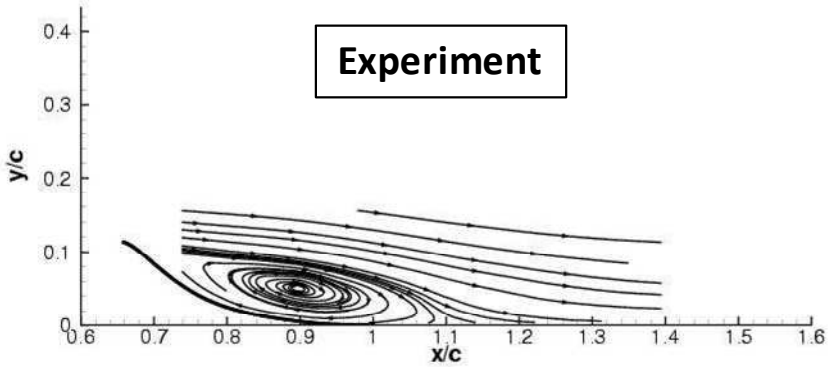

Figure B.3: Comparison of the separated flow region aft of the hump for the baseline case.

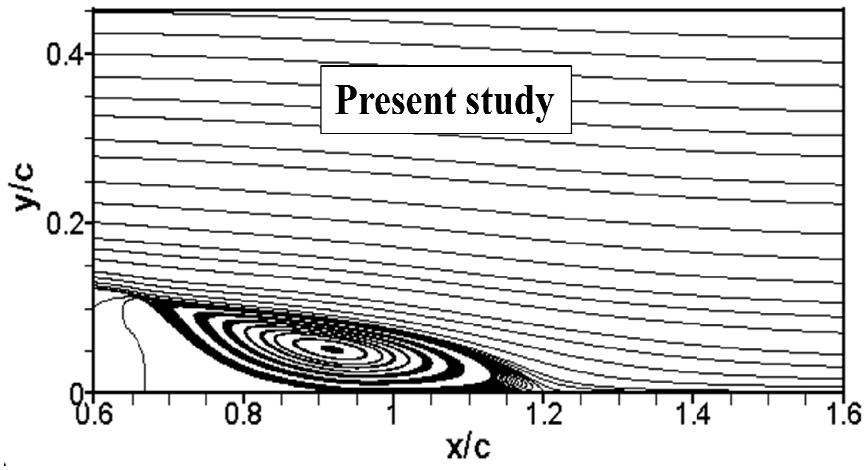

Figure B.3 continued.

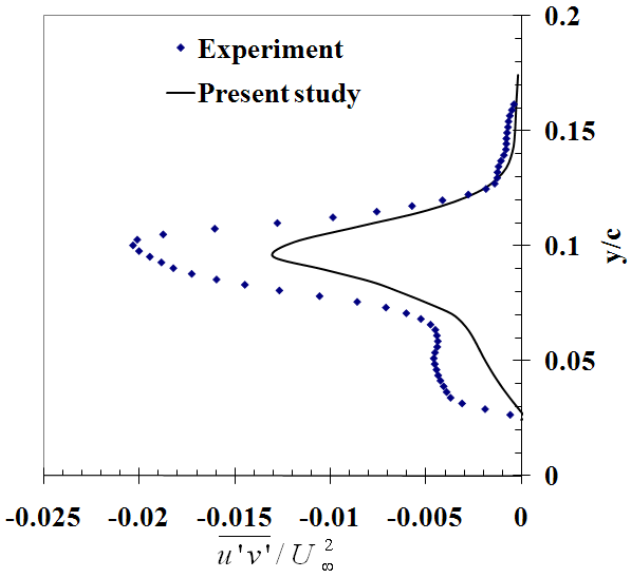

(a)

Figure B.4: Comparison of the Reynolds shear stress for baseline no flow control case at (a) x/c = 0.8 (b) x/c = 1.0 (c) x/c = 1.2.

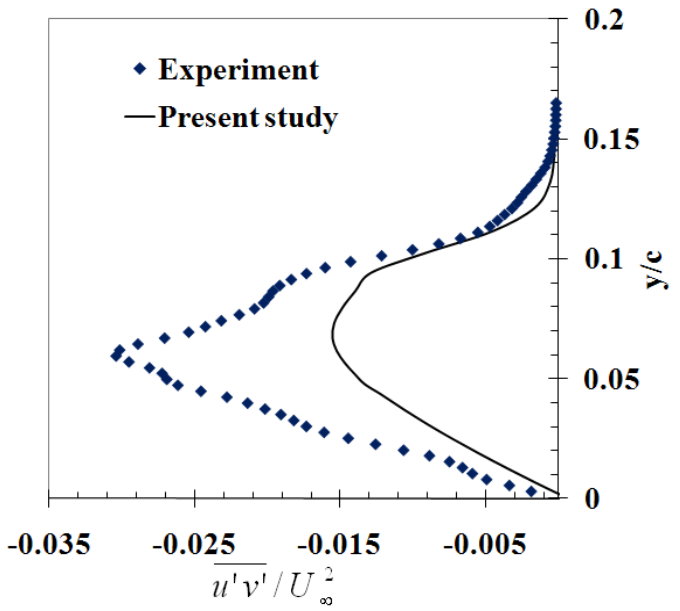

(b)

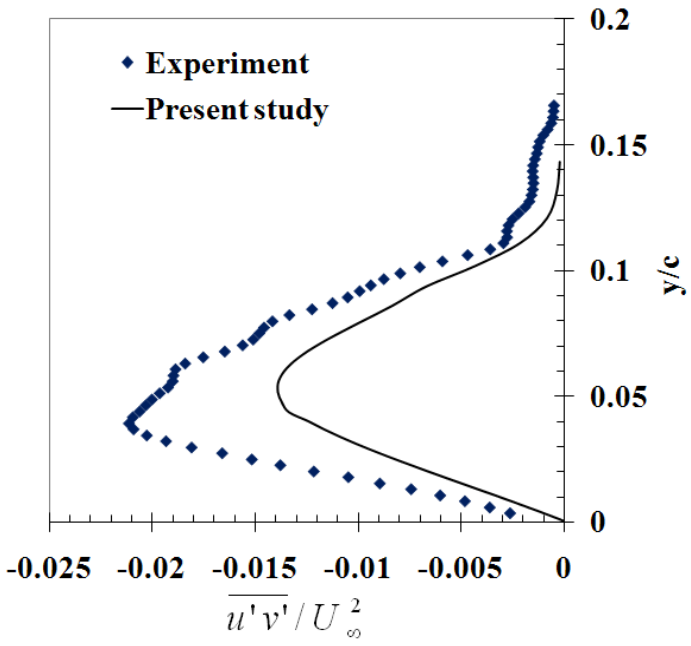

(c)

Figure B.4 continued.

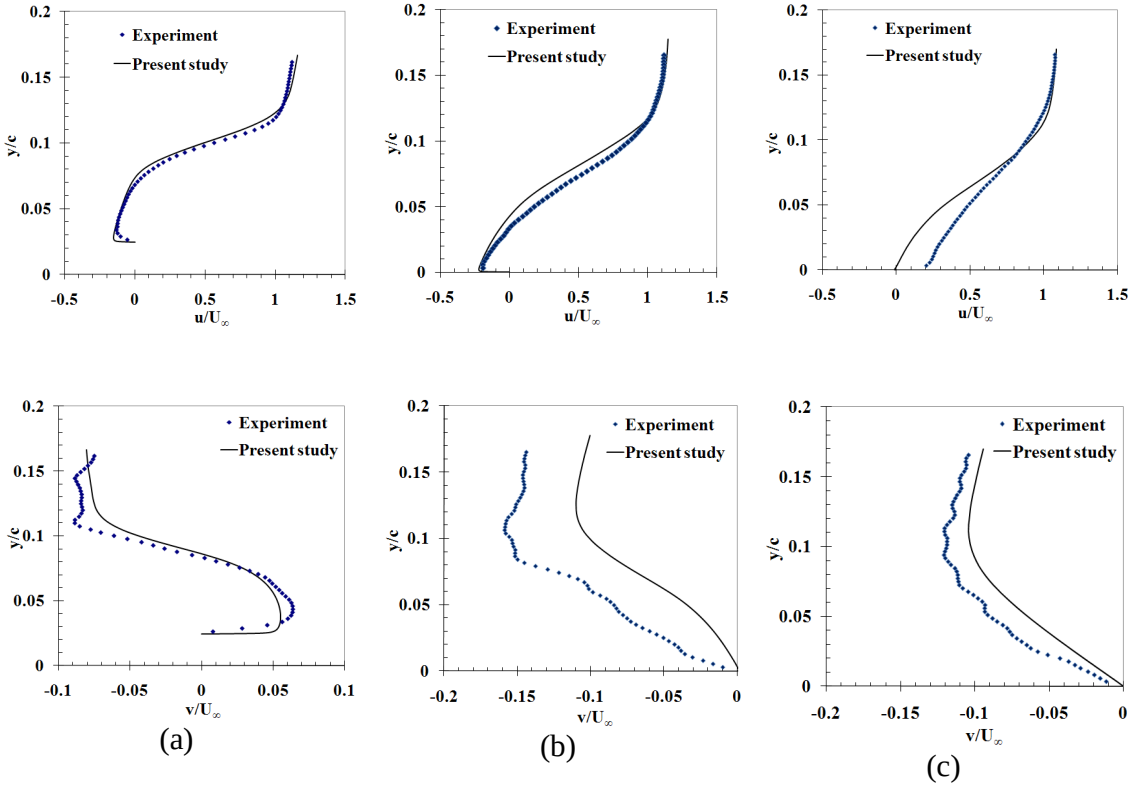

Figure B.5: Comparison of non-dimensional streamwise (top row) and cross stream velocities (bottom row) between experiment and simulations for the baseline case at (a) x/c = 0.8 (b) x/c = 1.0 (c) x/c= 1.2.

B.2.2 Active flow control cases

B.2.2.1 Steady suction

Next, active flow control studies were performed. Steady suction and synthetic jet concepts were explored. For the steady suction case, mass was removed at the bottom of the cavity at a rate of 0.01518 kg/s out of the domain. The Cp distribution for this CFD case again is in reasonable agreement with experiment everywhere except the separated region, as shown in Figure B.6. Figure B.7 shows the Reynolds stress variation across separated flow region at three x/c locations. As in the baseline case, the computed Reynolds stress levels were lower than those measured. This influenced the prediction of

pressure recovery and the reattachment point, both. It can be observed from Figure B.8 that for this case the separation occurs at x/c = 0.6618 in CFD while experiment predicts a separation between x/c = 0.675 and 0.685. The reattachment point predicted by CFD is at x/c = 1.19 which is further downstream of that predicted by experiment, x/c = 0.94. Note that the Reynolds shear stress values are lower in the steady suction case compared to the no flow control case, indicating that for this case the decrease in separation is due to the removal of the low momentum fluid due to suction. The difference between measurement and computation in the separated region is also noticed in the non-dimensional velocity comparison plots shown in Figure B.9. The negative streamwise velocity from computation in Figure B.9(b) shows that the flow is still separated at x/c = 1.0 in computations while it is already attached in measurements.

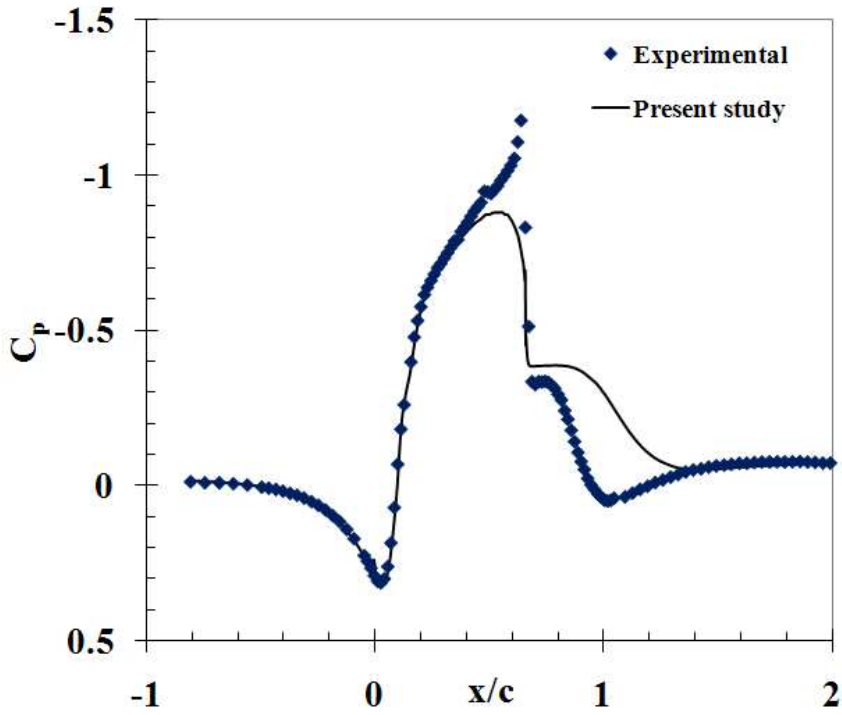

Figure B.6: Cp comparison between experiment and computation for flow over a hump steady suction case.

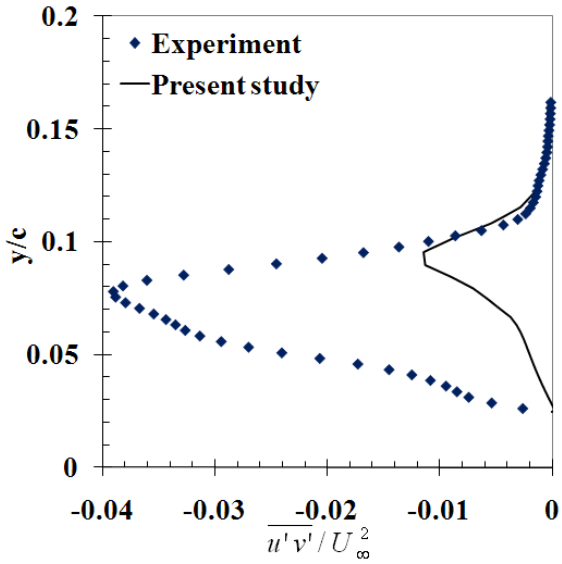

(a)

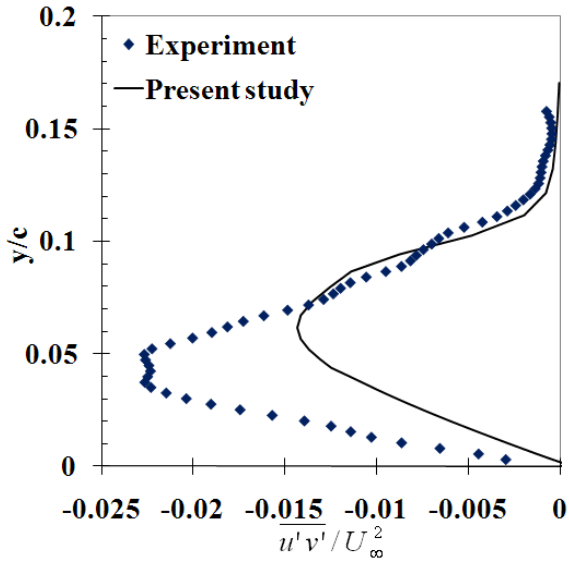

(b)

Figure B.7: Comparison of the Reynolds shear stress $\overline{u'v'}$ for the suction flow control case at (a) x/c = 0.8 (b) x/c = 1.0 (c) x/c = 1.2.

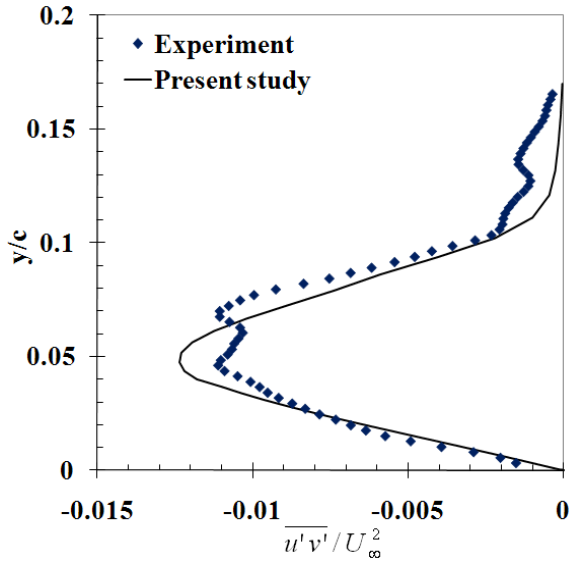

(c)

Figure B.7 continued.

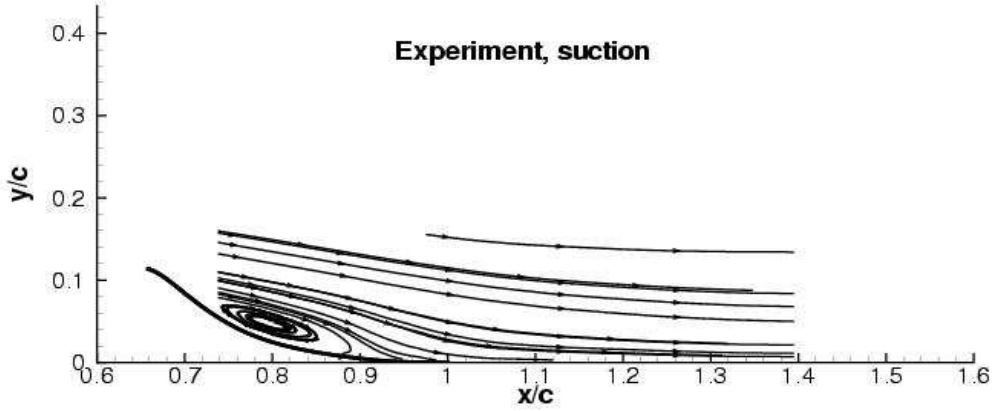

Figure B.8: Comparison of the separated flow region aft of the hump for the suction case.

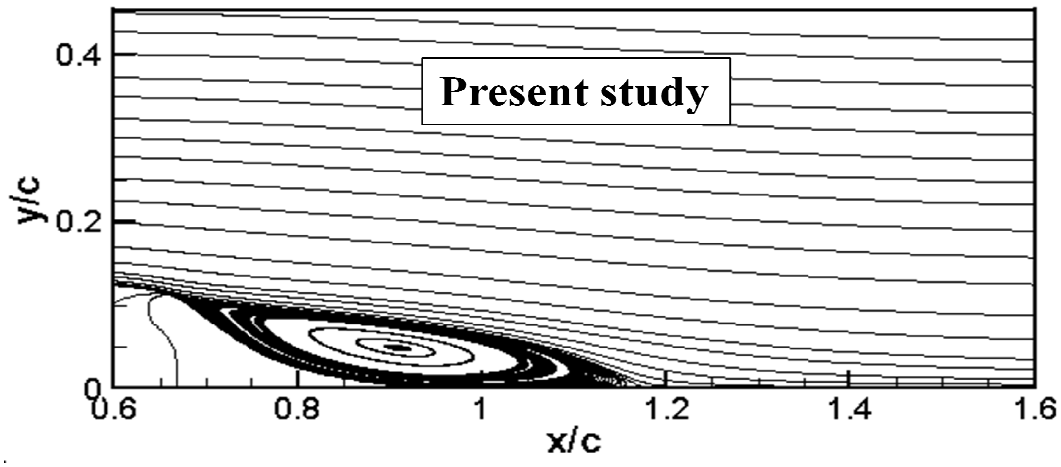

Figure B.8 continued.

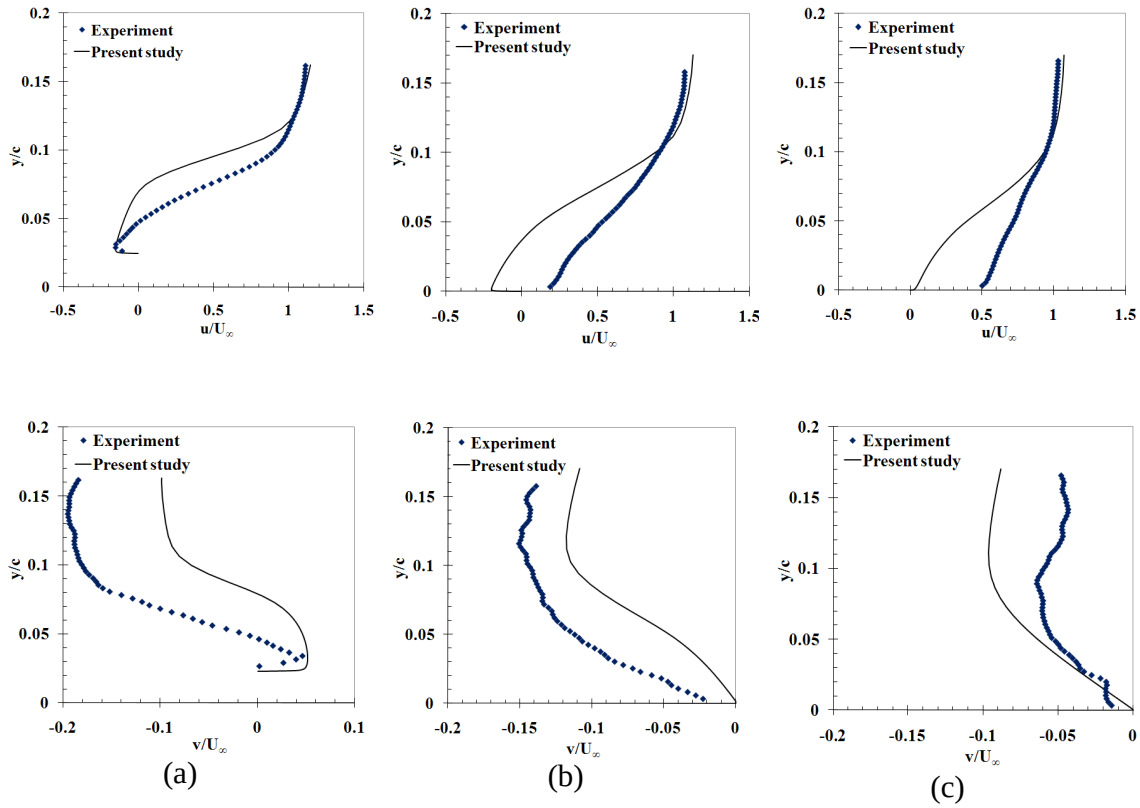

Figure B.9: Comparison of non-dimensional streamwise (top row) and cross stream velocities (bottom row) between experiment and simulations for the suction case at (a) x/c = 0.8 (b) x/c = 1.0 (c) x/c= 1.2.

B.2.2.2 Synthetic jet

Finally, the synthetic (oscillatory) jet case was simulated by imposing a sinusoidal velocity boundary condition at the bottom wall of the cavity. This jet has a frequency of 138.5 Hz and a peak velocity of 26-27 m/s. Further details of the CFD setup can be found in the paper by Rumsey[129]. As shown in Figure B.10, the Cp distribution agrees very well with experiment up to the slot location, but as in the previous cases, the agreement is not good in the separated flow region. The sudden change in Cp at the synthetic jet slot exit location could be attributed to the rapid change in the dynamic pressure in this region due to the synthetic jet. The reattachment takes place earlier than that predicted in the no control or even the steady suction case showing a decrease in the separation region, an improvement in pressure recovery compared to the baseline case, and an attendant decrease in the drag. This could be because of a dual mechanism taking place in the case of the synthetic jet compared to the suction case. Both concepts remove the low momentum fluid due to suction. Only the synthetic jet subsequently adds high momentum fluid into the flow.

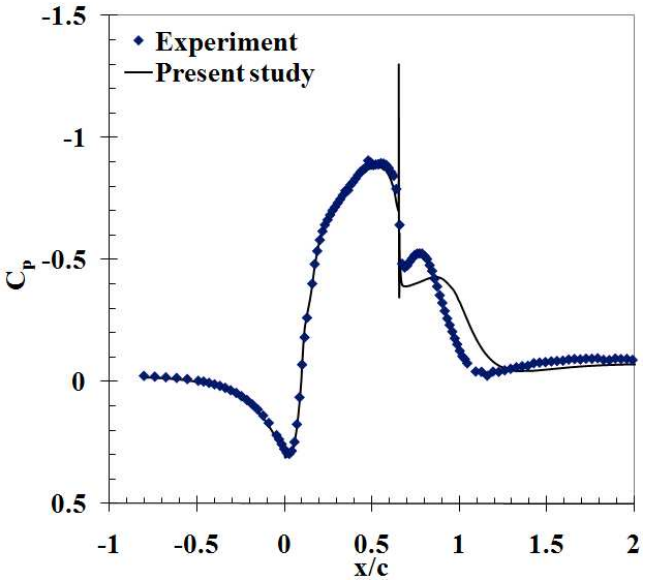

Figure B.10: Cp comparison between experiment and computation for flow over a hump synthetic jet case.

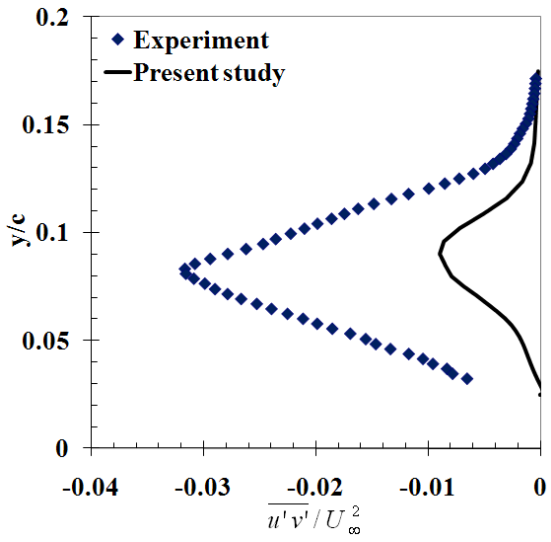

(a)

Figure B.11: Comparison of non-dimensional Reynolds shear stress $\overline{u'v'}$ for synthetic jet case at phase of 260^o at (a) x/c = 0.8 (b) x/c = 1.0 (c) x/c= 1.2.

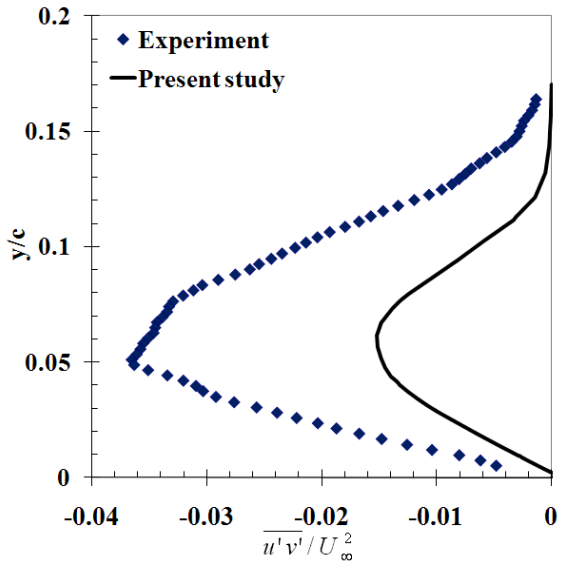

(b)

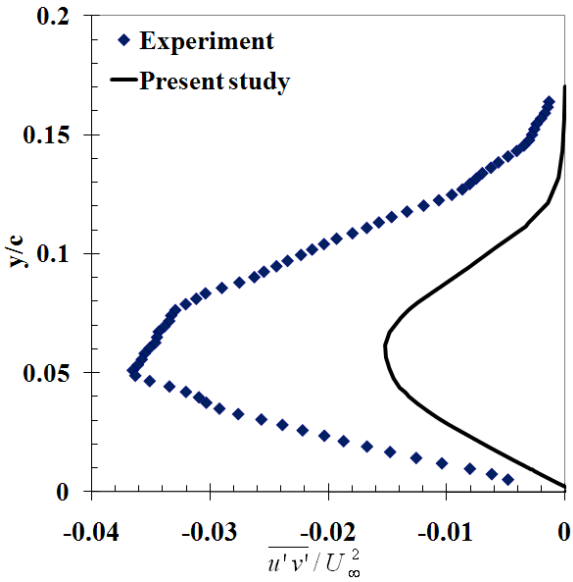

(c)

Figure B.11 continued.

A comparison of the Reynolds shear stress with experiment at a phase of 260^o of the synthetic jet cycle is shown in Figure B.11. Although the instantaneous values of Reynolds shear stress for this particular phase are greater than the corresponding parts in

the suction and baseline cases, the time averaged values are smaller as shown in Figure B.12. In order to confirm the conjecture that the increase in momentum of the flow due to the jet is a probable cause for drag reduction, comparison of Mach number contours are shown in Figure B.13. The higher Mach numbers with the synthetic jet device are in support of this conjecture.

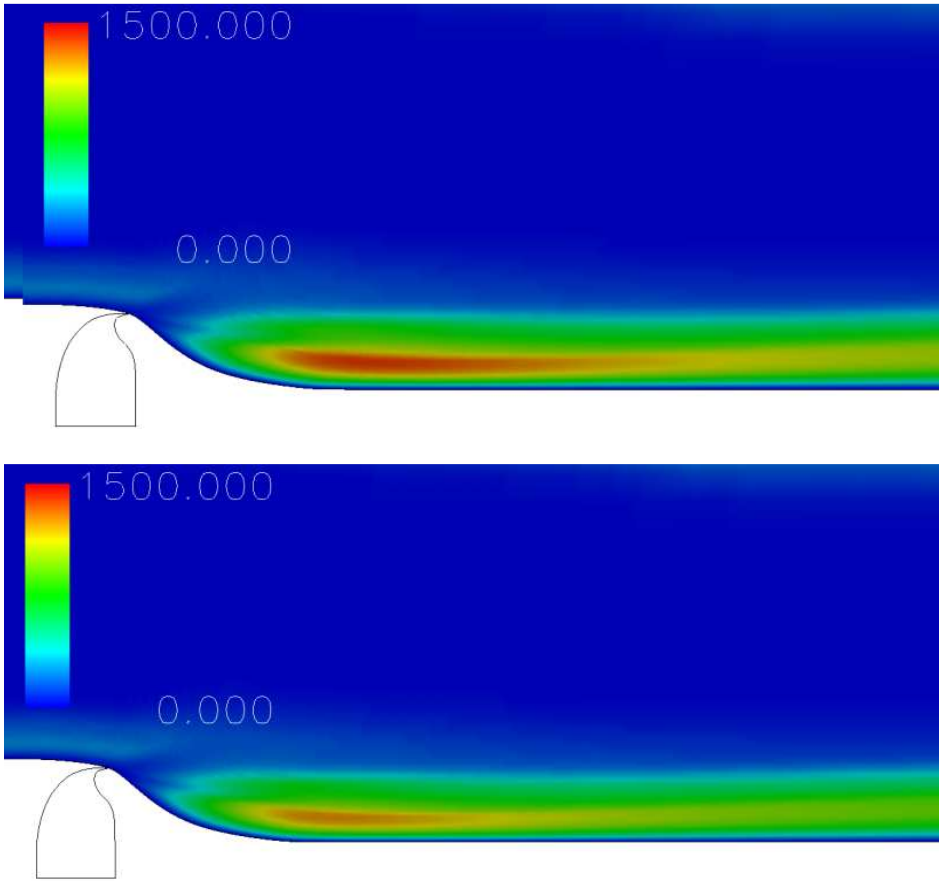

Figure B.12: Comparison of Turbulent viscosity contours between (a) Baseline (b) Steady Suction (c) (Time averaged) synthetic jet.

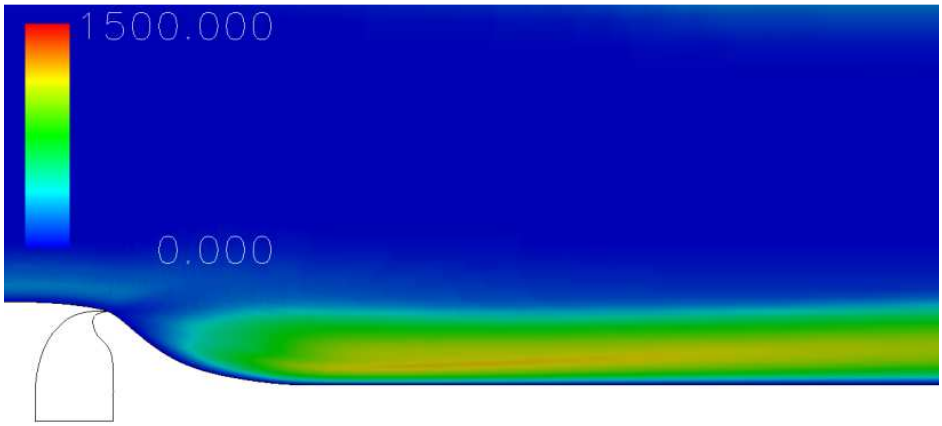

Figure B.12 continued.

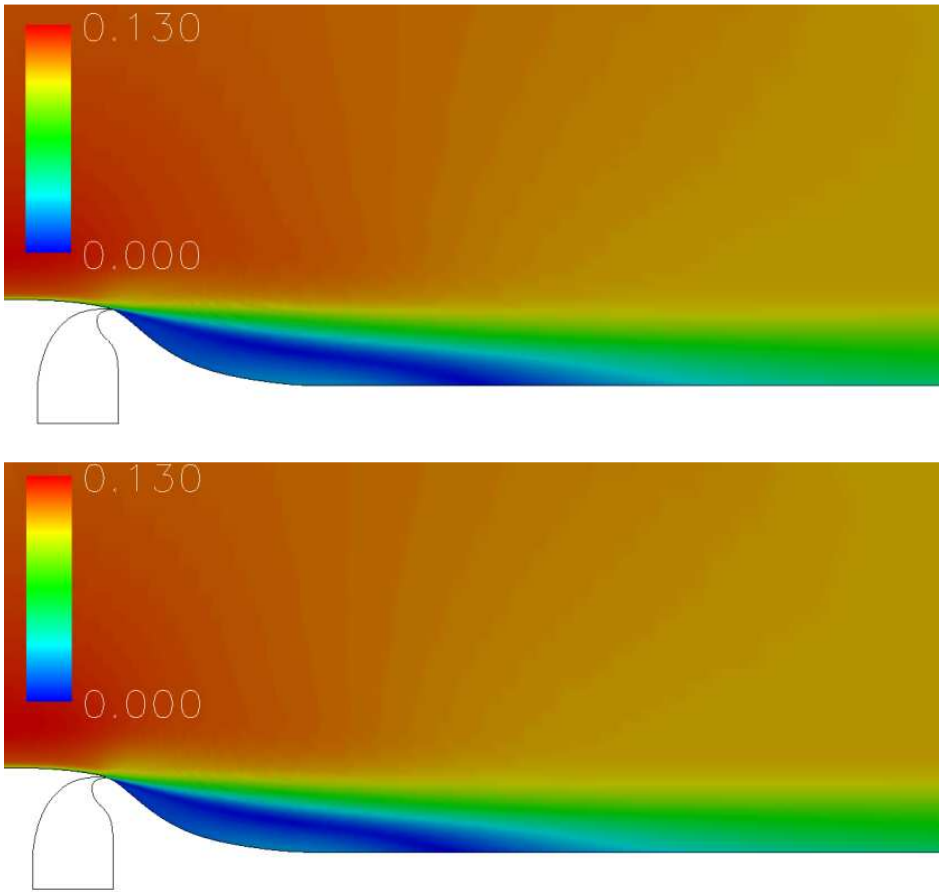

Figure B.13: Comparison of mach number contours between (a) Baseline (b) Steady Suction (c) (Time averaged) synthetic jet.

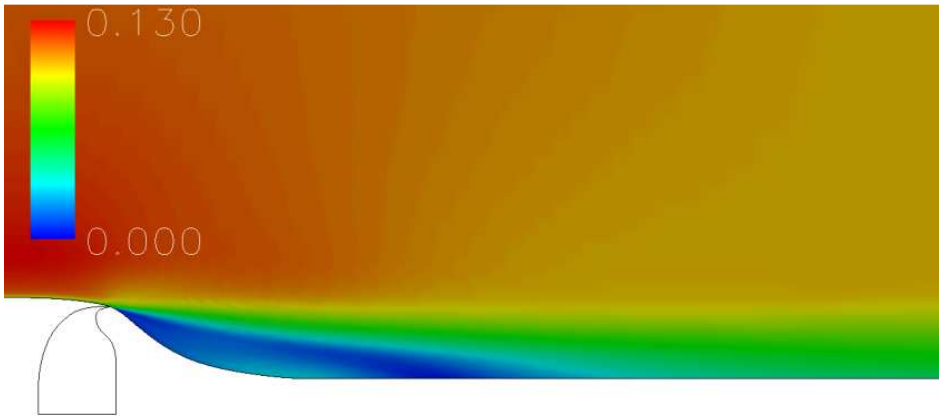

Figure B.13 continued.

The pressure distribution over the hump shape has been integrated, from x/c = -0.5 to x/c = 1.5, to extract the pressure drag forces. Because this is not a finite geometry (as in the case of airfoils) absolute drag values are not as interesting as the trends themselves. The bar graph in Figure B.14 shows the comparison of pressure drag between the baseline, suction and synthetic jet cases. The pressure drag coefficient has been non-dimensionalized with the baseline pressure drag. Hence the graph shows the decrease in pressure drag due to active flow control for the hump case. It can be seen that there is a decrease of around 11% and 14% in drag from the baseline to the suction and synthetic jet cases respectively. While the decrease from the suction case to the synthetic jet case is only around 3%, it should be noted that the mean C_μ in the synthetic jet case shown is slightly less than that for the suction case. In addition, the energy required to drive the piezoelectric actuator in the former case is much lower than in the latter case, making the use of synthetic jet devices more advantageous.

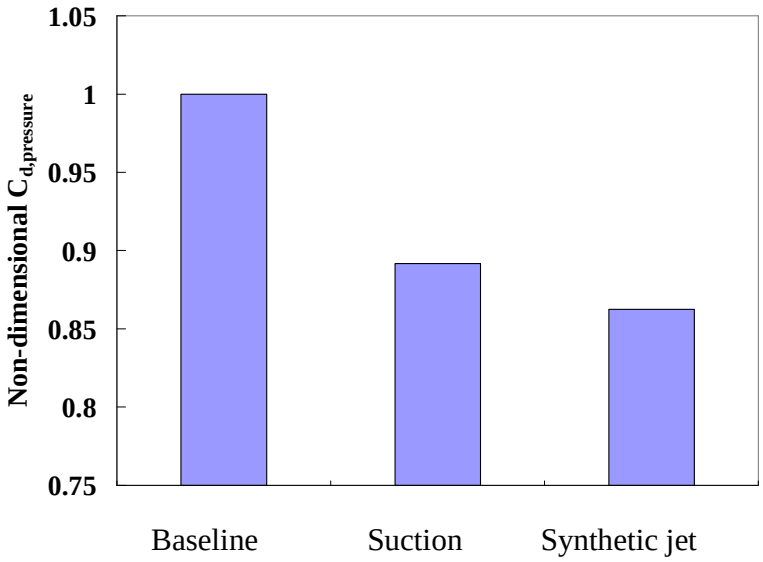

Figure B.14: Pressure drag coefficient (non-dimensionalized with respect to the baseline drag) decrease from baseline case to suction and time averaged value of synthetic jet case.

B.2.3 Power analysis

Now, the amount of power consumed by the two active flow control cases is examined. If the power saved is less than the power expended on the device, active flow control would not be an attractive prospect. The ratio of the power saved by the device to the power used is studied. The power used by the device (P_j) can be written as

$$P_j = \frac{1}{2\eta}\dot{m}_J V_J^2 \tag{B.1}$$

where η is the efficiency of the device (nominally assumed to be 0.8 in this study), $\dot{m}_J$ is the mass flow rate into or from the active flow control device and V_J is the jet velocity. In the case of the synthetic jet devices V_J is the root mean square velocity and $\dot{m}_J$ is given by

$$\dot{m}_J = \rho_J A_J V_J \tag{B.2}$$

where ρ_J is the density of the jet and A_J is the area of cross section of the jet slot. In the present two-dimensional case it is the width or height of the slot per unit span.

The power saved by the device (P_s) may be written as

$$P_s = \frac{1}{2}\rho_\infty V_\infty^2 c.V_\infty \Delta C_{do} \tag{B.3}$$

where ρ_∞ is the freestream density and V_∞ is the freestream velocity. Also, c is the chord and ΔC_{do} is the reduction in total drag due to active flow control. For the configurations considered here, ΔC_{do} is predominantly due to pressure recovery affected by the reduction in separation. The ratio of P_s to P_j indicates whether using active flow control is suitable for any given case. The higher the ratio, the smaller the amount of power required to drive the flow control device and hence more attractive for commercial use.

In practical applications, other factors enter into the acceptance of these devices. These include the ease with which these devices may be incorporated in existing and new configurations, their robustness in harsh environments, and manufacturability. A system of systems approach is needed for designing these devices, where aerodynamic analyses such as those attempted here form a single but important component.

In the present study, the ratio of power saved by the steady suction jet to the power consumed by it is 25.0 whereas that for the synthetic jet is 37.0. Note that efficiency has been assumed to be 0.8 for comparisons. In other words, with a small 2% to 3% expenditure in power, substantial savings in the power consumption associated with drag may be achieved. While both approaches were successful, the increased

reduction in drag, the lower power required, and the elimination of suction pumps, make synthetic jets a more attractive drag reduction device compared to steady blowing jets for this configuration.

APPENDIX C

ADDITIONAL BASELINE FLOW PAST CYLINDER VALIDATIONS

The present NS solver has also been validated for Reynolds numbers other than that shown in Chapter 5. Firstly, comparison of the flow past a cylinder without active flow control has been performed for a low Reynolds number of 3900 and compared to existing data. Secondly, the simulations have been validated for a higher Reynolds number of $3x10^5$.

C. 1 Reynolds number = 3900

For a standard O-grid of size 257x129 two-dimensional grid, the NS solver has been used to simulate the flow past a 2-D cylinder in an external flow. For a low Reynolds number of 3900, surface pressure distributions have been compared to existing data presented by Xu et al[154]. The results presented here have been performed by Mr. Jeewoong Kim, using the same NS solver as discussed before.

Figure C.1 shows the comparison of surface pressure distribution between the present analysis and existing data. It can be seen that the present NS solver is in good comparison to other simulated data. The Strouhal number obtained from the present simulations is 0.213 which is within 1% of the experimental value of 0.215 (± 0.005). However, as discussed in Chapter 5, these 2-D simulations overpredict the value of the drag coefficient. The C_d obtained from simulations is 1.497 while that from experiment is 0.99 (± 0.05).

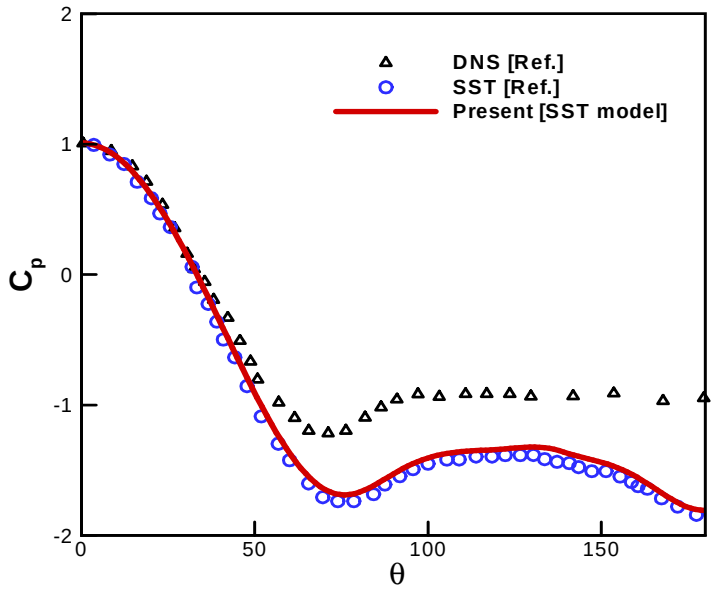

Figure C.1: Comparison of time-averaged surface pressure distribution between simulated data for Re = 3900.

C. 2 Reynolds number = 3.8×10^5

For an O-type grid of size 294x90, analysis has been done for a Reynolds number of 3.8x105 based on the cylinder diameter. The Reynolds number used is the same as in the experiments conducted by Ribeiro[157]. In these experiments, one of the methods used to obtain surface roughness on the cylinder was to use two-dimensional wire screens. This has been done so that turbulent separation is obtained in the wake of the cylinder. Therefore, this data could be used to compare to present simulations where the flow field is assumed to be fully turbulent. The comparison of time-averaged surface pressure data between experiment and simulations has been shown in Figure C.2. The pressure recovery behind the cylinder would be improved when compared with 3-D simulations, as discussed in Section 6.1.

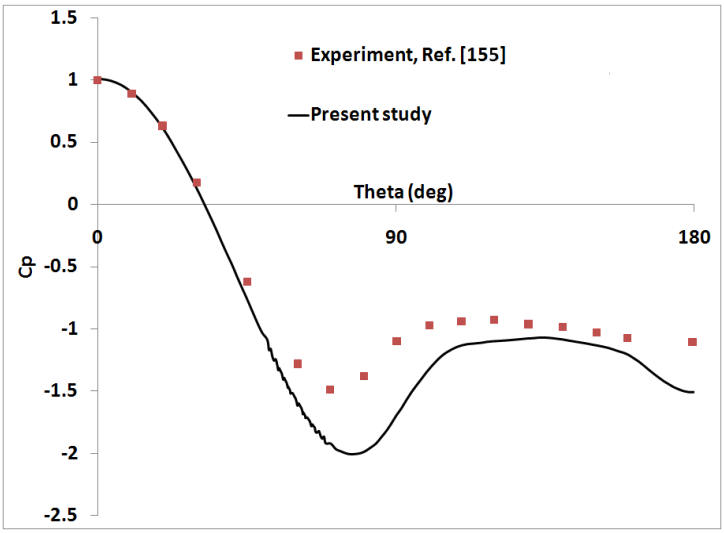

Figure C.2: Comparison of time-averaged surface pressure distribution between experiment (Ref. [157]) and simulations for Re = 3.8×10^5.

REFERENCES

[1] http://www.militaryfactory.com/blueprints/rah66.asp (cited 13th September, 2010).

[2] Prouty, R. W., Helicopter Performance, Stability and Control, Malabar, Fla.: R.E. Krieger Pub. Co., 1990.

[3] Aamo, O.M. and Krstic, M., "Flow control by feedback: stabilization and mixing," New York: Springer-Verlag, 2003.

[4] GadelHak, M., "The fluid mechanics of microdevices- the Freeman Scholar Lecture," *Journal of Fluids Engineering*, Vol. 121, pp. 5–33, Mar 1999.

[5] GadelHak, M., "Flow control: the future," *Journal of Aircraft*, Vol. 38, no. 3, pp. 402–418, 2001.

[6] Rathnasingham R. and Breuer, K. S., "Coupled fluid-structural characteristics of actuator for flow control," *AIAA Journal*, vol. 35, no. 5, pp. 832–837, 1997.

[7] Glezer A. and Amitay, M., "Synthetic jets," *Annual Review of Fluid Mechanics*, Vol. 34, pp. 503–529, 2002.

[8] Smith B. and Glezer, A., "The formation and evolution of synthetic jets," *Physics of Fluids*, Vol. 10, No. 9, pp. 2281–2297, Sep 1998.

[9] Amitay M. and Glezer, A., "Role of actuation frequency in controlled flow reattachment over a stalled airfoil," *AIAA Journal*, Vol. 40, pp. 209–216, 2002.

[10] McLaughlin, T. E., Munska, M. D., Vaeth, J. P., Dauwalter, T. E., Goode, J. R., and Siegel, S. G., "Plasma-Based Actuators for Cylinder Wake Vortex Control," 2nd AIAA Flow Control Conference, 2004, AIAA Paper 2004-2129.

[11] Gilarranz, J., Traub, L. and Rediniotis, O., "Characterization of a compact, high-power synthetic jet actuator for flow separation control," *AIAA Paper*. 2002-0127.

[12] Amitay, M., Smith, D., Kibens, V., Parekh, D. and Glezer, A., "Aerodynamic flow control over an unconventional airfoil using synthetic jet actuators," *AIAA Journal*, Vol. 39, pp. 361–370, 2001.

[13] Stroub, Robert H.; Young, Larry A.; Graham, David R.; Louie, Alexander W., "Investigation of generic hub fairing and pylon shapes to reduce hub drag," 13th European Rotorcraft Forum, Sept. 8-11, 1987.

[14] Stroub, Robert H., "Introduction of the M-85 high-speed rotorcraft concept," Proceedings of the 48th Annual American helicopter Society Forum, Vol. 2, June 1992.

[15] Young, Larry A.; Graham, David R.; Stroub, Robert H.; Louie, Alexander W., "Reduction of hub- and pylon-fairing drag," 43rd AHS Forum, Saint Louis, MO, May 18-20, 1987.

[16] Saltzman, Edwin J. and Meyer, Robert R., Jr., "Drag Reduction Obtained by Rounding Vertical Corners on a Box-Shaped Ground Vechicle," NASA TM X-56023, 1974.

[17] Saltzman, Edwin J., Meyer, Robert R., Jr., and Lux, David P., "Drag Reductions Obtained by Modifying a Box-Shaped Ground Vehicle," NASA TM X-56027, 1974.

[18] Montoya, Lawrence C. and Steers, Louis L., "Aerodynamic Drag Reduction Tests on a Full-Scale Tractor-Trailer Combination with Several Add-On Devices," NASA TM X-56028, 1974.

[19] Steers, Louis L., Montoya, Lawrence C., and Saltzman, Edwin J., "Aerodynamic Drag Reduction Tests on a Full-Scale Tractor-Trailer Combination and a Representative Box-Shaped Ground Vehicle," SAE Paper 750703, 1975.

[20] Waring J., "Reduction of drag of a submerged swimmer using vortex generators," Department of Mechanical and Aerospace Engineering. Ottawa: Carleton University. p 76, 1999.

[21] http://www.aerospaceweb.org/question/aerodynamics/q0215.shtml (cited 1st March, 2010).

[22] Reidy, L. W., "Flat plate drag reduction in a water tunnel using riblets," NOSC Tech. Rep. 1169, 1987.

[23] Anderson, E. J., MacGillivray, O. S., and DeMont, M. E., "Scallop shells exhibit optimization of riblet dimensions for drag reduction," Biol. Bull. 192:341-344, 1997.

[24] Blick, E. F. and Walters, R. R., "Turbulent boundary-layer characteristics of compliant surfaces," Journal of Aircraft, 5:11-16, 1968.

[25] Miklosovic, D. S., Murray, M. M., Howle, L. E. and Fish, F. E., "Leading-edge tubercles delay stall on humpback whale (Megaptera novaeangliae) flippers," *Physics of Fluids*, Vol. 16, No. 5; 39-42, May 2005.

[26] Fish, F. E., and Hui, C. A., "Dolphin swimming – a review," *Mammal Review*, Vol. 21, No. 4; 181-195, 1991.

[27] Triantafyllou, G. S., Triantafyllou, M. S. amd Gosenbaugh, M. A., "Optimal thrust development in oscillating foils with application to fish propulsion," Journal of Fluids Structure, 7:205-224, 1993.

[28] Gopalkrishnan, R., Triantafyllou, M. S., Triantafyllou, G. S., and Barrett, D. "Active vorticity control in a shear flow using a flapping foil," Journal of Fluid Mechanics, 274:1-21, 1994.

[29] Yi Liu, Lakshmi N. Sankar, Robert J. Englar, and Krishan K. Ahuja, "Numerical simulations of the steady and unsteady aerodynamic characteristics of a circulation control wing airfoil", Aerospace Sciences Meeting and Exhibit, 39th, Reno, NV, Jan. 8-11, 2001, AIAA 2001-0704.

[30] Williams, D., R., Mansy, H. and Amato, C., "The response and symmetry properties of a cylinder wake subjected to localized surface excitation," *Journal of Fluid Mechanics*, 234, pp. 71-96, 1992.

[31] Kim, J. and Choi, H., "Distributed forcing of flow over a cylinder," *Physics of Fluids*, 17, 033103, 2005.

[32] Amitay, M., Honohan, A. M., Trautman, M., and Glezer, A., "Modification of the aerodynamic characteristics of bluff bodies using fluidic actuators," 28th AIAA Fluid Dynamics Conference, Snowmass, Colorado, 1997, AIAA Paper 97-2004.

[33] Amitay, M., Smith, B. L., and Glezer, A., “Aerodynamic flow control using synthetic jet technology,” 36th AIAA Aerospace Sciences. Meeting 98–0208, Reno, Nevada, 1998.

[34] Kral, L. D., Donovan, J. F., Cain, A. B., and Cary, A. W., “Numerical simulation of synthetic jet actuators,” 28th AIAA Fluid Dynamics Conference 97-1824, Reno, Nevada, 1997.

[35] Smith, D. R., Amitay, M., Kibens, V., Parekh, D. E., and Glezer, A., “Modification of Lifting body aerodynamics using synthetic jet actuators,” 36th AIAA Aerospace Sciences Meeting 98-0209, Reno, Nev., 1998.

[36] Amitay, M., Kibens, V., Parekh, D. E., and Glezer, A., “Flow reattachment dynamics over a thick airfoil controlled by synthetic jet actuators,” 37th AIAA Aerospace Sciences Meeting 99-1001, Reno, Nevada, 1999.

[37] Amitay, M., Smith, D. R., Kibens, V., Parekh, D. E., and Glezer, A., “Aerodynamic flow control over an unconventional airfoil using synthetic jet actuators,” AIAA Journal 39:361–70, 2001.

[38] Seifert, A. and Pack, L. G., “Oscillatory control of separation at high Reynolds numbers,” AIAA Journal 37(9):1062–71, 1999.

[39] Lorkowski, T., Rathnasingham, R., and Breuer, K. S., “Small-scale forcing of a turbulent boundary layer,” AIAA 28th Fluid Dynamics Conference 97-1792, 1997.

[40] Davis, S. A. and Glezer, A., “Mixing control of fuel jets using synthetic jet technology,” AIAA 37th Aerospace Sciences Meeting 99-0447, Reno, Nevada, 1999.

[41] Amitay, M., Pitt, D., Kibens, V., Parekh, D. E., and Glezer, A., “Control of Internal Flow Separation using Synthetic Jet Actuators”, AIAA Paper 2000-0903.

[42] Ben-Hamou, E., Arad, E., and Seifert, A., “Generic Transport Aft-Body Drag Reduction using Active Flow Control,” AIAA Paper 2006-2509, 2nd AIAA Flow Control Conference, Portland, OR, 28 June – 1 July 2004.

[43] Hassan, A. A. and Munts, E. A., “Transverse and Near-tangent Synthetic Jets for Aerodynamic Flow Control,” AIAA Paper 2000-4334, 18th Applied Aerodynamics Conference, Denver, Colorado, 2000.

[44] Jacot, D. and Mabe, J., "Boeing Active Flow Control system for V-22," AIAA Paper 2000-2473, Fluids 2000, Denver, Colorado, June 2000.

[45] Grife, R., Darabi, A., and Wygnanski, I. J., "Download reduction on a Three Dimensional V-22 Model Using Active Flow Control," AIAA 2000-3071, 1st Flow Control Conference, St. Louis, MO, June 2002.

[46] Greenblatt, D. and Wygnanski, I. J., "The Control of Flow Separation By Periodic Excitation," Progress in Aerospace Sciences, Vol. 36, Pergamon, 2000, pp. 487-545.

[47] Naim, A., Greenblatt, D., Seifert A., and Wygnanski, I., "Active Control of a Circular Cylinder Flow at Transitional Reynolds Numbers," (part of AIAA Paper 2002-3070), special Issue of Flow, Turbulence and Combustion on "Air-jet actuators and their use for flow control," (2007), 78: 383-407.

[48] Ben-Hamou, E., Arad, E., and Seifert, A.., "Generic Transport Aft-Body Drag Reduction Using Active Flow Control," (previously AIAA paper 2004-2509), special Issue of Flow, Turbulence and Combustion on "Air-jet actuators and their use for flow control," (2007), 78: 365-382.

[49] Palei, V. and Seifert, A., "Effects of Periodic Excitation on the Flow around a D-Shaped Cylinder at Low Reynolds Numbers," special Issue of Flow, Turbulence and Combustion on "Air-jet actuators and their use for flow control," (2007), 78: 409-428.

[50] Lim C. Y., Shu C., Niu X. D., and Chew Y. T., "Application of lattice Boltzmann method to simulate microchannel flows," *Physics of Fluids*, vol. 14, No. 7, pp. 2299-2308, 2002.

[51] Beylich, A. E., "Solving the kinetic equation for all Knudsen numbers," *Physics of Fluids*, Vol. 2, No. 2, February 2000.

[52] Bird, G. A., *Molecular Gas Dynamics*, Oxford University Press, 1976.

[53] Schillar, U. D., "Dissipative Particle Dynamics: A Study of the Methodology Background," *Diploma Thesis*, University of Bielefeld, 2005.

[54] Español, P., "Fluid particle dynamics: a synthesis of dissipative particle dynamics and smoothed particle dynamics," *Europhysics Letters*, 22 May 1997.

[55] Hardy, J. and Pomeau, Y., “Thermodynamics and hydrodynamics for a modeled fluid,” *Journal of Mathematics and Physics*, vol. 13, No. 7, pp. 1042-1051, 1972.

[56] Hardy, J., DE Pazzis, O., and Pomeau, Y., “Time evolution of a two-dimensional model system. I. Invariant states and time correlation functions,” *Journal of Mathematics and Physics*, vol. 14, pp. 1746, 1973.

[57] Frisch U., Hasslacher B., and Pomeau Y., “Lattice-Gas Automata for the Navier-Stokes Equations,” *Physical Review Letters*, vol. 56, pp. 1505-1508, 1986.

[58] Frisch U., d’Humières D., Hasslacher B. Lallemand P., Pomeau Y., and Rivet J. P., “Lattice Gas Hydrodynamics in Two and Three Dimensions,” *Complex Systems,* vol. 1, pp. 649-707, 1987.

[59] Wolfram S., “Cellular automaton fluids 1: Basic theory,” *Journal of Statistical Physics*, vol. 45, pp. 471-526, 1986.

[60] Chen S., Diemer K., Doolen G. D. (Ed.), Eggert K., Fu C., Gutman S., and Travis S. J., “Lattice gas automata for flow through porous media,” *Physica D,* vol 47, pp. 72-84, 1991.

[61] Satofuka N., and Nishioka T., “Parallelization of Lattice Boltzmann Method for Incompressible flow Computations,” *Computational Mechanics*, vol. 23, pp. 164-171, 1999.

[62] McNamara G., and Zanetti G., “Use of the Boltzmann Equation to Simulate Lattice-Gas Automata,” *Physical Review Letters*, vol. 61, Issue 20, pp. 2332-2335, 1988.

[63] Higuera F., and Jimenez J., “Boltzmann Approach to Lattice Gas Simulations,” *Europhysics Letters*, vol. 9, Issue 7, pp. 663-668,1989.

[64] Higuera F., and Succi S., “Simulating the Flow Around a Circular Cylinder with a Lattice Boltzmann Equation ,” *Europhysics Letters*, vol. 8, Issue 6, pp. 517-521,1989.

[65] Qian Y., “Lattice Gas and lattice kinetic theory applied to the Navier-Srokes equations,” *Ph.D. Thesis*, Universit é Pierre et Marie Curie, January 1990.

[66] Chen S., Chen H., Martinez D., and Matthaeus W. H., "Lattice Boltzmann model for simulation of magnetohydrodynamics," *Physical Review Letters*, vol. 67, Issue 27, pp. 3776-3779, 1991.

[67] Qian Y., d'Humières D., and Lallemand P., "Lattice BGK Models for Navier-Stokes Equations," *Europhysica Letters*, vol 17(6), pp. 479-484,1992.

[68] Chen H., Chen S., and Matthaeus W. H., "Recovery of the Navier-Stokes equations using a lattice-gas Boltzmann method," *Physical Review A*, vol. 45, Issue 8, pp. 5339-5342, 1992.

[69] Kingdon R. D., Schofield P., and White L., "A lattice Boltzmann model for the simulation of fluid flow," *Journal of Physics A: Mathematical and General*, vol. 25, Issue 12, pp. 3559-3566, 1992.

[70] Bhatnagar P. L., Gross E. P., and Krook M., "A Model for Collision Processes in Gases. I. Small Amplitude Processes in Charged and Neutral One-Component Systems," *Physical Review*, vol. 94, Issue 3, pp. 511-525, 1954.

[71] Rothman D. H., and Zaleski S., "Lattice-Gas models of Phase Separation: Interfaces, Phase Transitions, and Multiphase Flow," *Review of Modern Physics*, vol. 66, No. 4, pp. 1417-1479, 1994.

[72] He X., and Luo L. –S., "A priori derivation of the lattice Boltzmann equation," *Physical Review E*, vol. 55, Issue 6, pp. 6333-6336, 1997.

[73] He X., and Luo L. –S., "Theory of the lattice Boltzmann method: From the Boltzmann equation to the lattice Boltzmann equation," *Physical Review E*, vol. 56, Isuue 6, pp. 6811-6817, 1997.

[74] Abe T., "Derivation of the Lattice Boltzmann Method by Means of the Discrete Ordinate Method for the Boltzmann Equation," *Journal of Computational Physics*, vol. 131, Issue 1, pp. 241-246, 1997.

[75] d'Humières D., "Rarefied Gas Dynamics: Theory and Simulations," *Progress in Astronautics and Aeronautics*, vol. 159, edited by Shizgal B/ D., and Weaver D. P. (AIAA, Washington, D. C., 1992).

[76] Lallemand P., and Luo L. –S., "Theory of the lattice Boltzmann method: Dispersion, dissipation, isotropy, Galilean invariance, and stability," *Physical Review E*, vol. 61, Number 6, pp. 6546-6562, June 2000.

[77] Bouzidi M., d'Humières D., and Lallemand P., "Lattice Boltzmann Equation on 2D Rectangular Grid," *Journal of Computational Physics*, vol. 172, pp. 704-717, 2001.

[78] Mei R., Yu D., and Shyy W., "Assessment of the Multiple-Relaxation-Time and Single-Relaxation-Time Models in the Lattice Boltzmann Equation Method," *15th AIAA CFD Conference, Anaheim, CA, 11-14 June, 2001,* AIAA 2001-2666.

[79] Feiz, H., Soo, J. H. and Menon, S., "LES of Turbulent Jets using the Lattice Boltzmann Approach," 41st Aerospace Sciences Meeting and Exhibit, 6-9 January, 2003, Reno, Nevada, AIAA 2003-780.

[80] Menon, S. and Soo, J. H., "Simulation of vortex dynamics in three-dimensional synthetic and free jets using the large-eddy lattice Boltzmann method," *Journal of Turbulence*, Vol. 5, Art. No. N32.

[81] Orphee, J., Gugnor, A. G., Rocha, M. S. and Menon, S., "Direct and Large-Eddy Simulation of Decaying and Forced Isotropic Turbulence Using Lattice Boltzmann Method," 36th AIAA Fluid Dynamics Conference and Exhibit, 5-8 June 2006, San Francisco, California, AIAA 2006-3904.

[82] Feiz H., "LES of Multiple jets in Cross-Flow using a Coupled lattice Boltzmann-Navier-Stokes solver," *PhD Thesis*, Georgia Institute of Technology, Atlanta, 2006.

[83] Noble D. R., Chen S., Georgiadis J G., and Buckius R. O., "A consistent hydrodynamic boundary condition for the lattice Boltzmann method," *Physics of Fluids*, vol. 7, number 1, pp. 203-209, January 1995.

[84] Inamuro T., Yoshino M., and Ogino F., "A non-slip condition for lattice Boltzmann simulations," *Physics of Fluids*, vol. 7, number 12, pp. 2928-2930, Decebmer 1995.

[85] Zou Q., and He X., "On pressure and velocity boundary conditions for the lattice Boltzmann BGK model," *Physics of Fluids*, vol. 9, number 6, pp. 1591-1598 , June 1997.

[86] Bouzidi M., Firdaouss M., and Lallemand P., "Momentum transfer of a Boltzmann-lattice fluid with boundaries," *Physics of Fluids*, vol. 13, number 11, pp. 3452-3459, November 2001.

[87] Mei R., Yu D., Shyy W., "Force evaluation in the lattice Boltzmann method involving curved geometry," *Physical review E*, vol. 65, 041203, 2002.

[88] He X., Luo L. –S., and Dembo M., "Some Progress in Lattice Boltzmann Method. Part I. Nonuniform Mesh Grids," *Journal of Computational Physics*, vol. 129, pp. 357-363, 1996.

[89] Inamura T., Suzuki K., Nakamura T., and Yoshida M., "Acceleration of steady-state lattice Boltzmann simulations on non-uniform mesh using local time step method," *Journal of Computational Physics*, vol. 202, pp. 645-663, 2005.

[90] He X., and Doolen G., "Lattice Boltzmann Method on Curvilinear Coordinates System: Flow around a Circular Cylinder," Journal of Computational Physics, vol. 134, pp. 306-315, 1997.

[91] Filippova O., and Hänel D., "Boundary-fitting and local grid refinement for lattice-BGK models," *International Journal of Modern Physics C*, vol. 9, No. 8, pp. 1271-1279, 1998. Also presented at the *7th International Conference on the Discrete Simulation of Fluids*, University of Oxford, 14-18 July, 1998.

[92] Benzi R., Succi S., and Vergassola M., "The Lattice Boltzmann Equation: Theory and Applications," *Physics Reports* , vol. 222, No. 3, pp. 145-197, 1992.

[93] Chen S., and Doolen G. D., "Lattice Boltzmann Method for Fluid Flows," *Annual Review of Fluids Mechanics*, vol. 8, No. 9, pp. 2527-2536, 1996.

[94] Yu D., Mei R., Luo L. –S., and Shyy W., "Viscous Flow Computations with the Method of Lattice Boltzmann Equation," *Progress in Aero Sciences*, vol. 39, pp. 329-367, 2003.

[95] Succi, S., Benzi R., and Higuera F., "The lattice Boltzmann equation: A new tool for computational fluid-dynamics," *Physica D*, vol. 47, pp. 219-230, 1991.

[96] Chen S., Wang Z., Shan X., and Doolen G. D., "Lattice Boltzmann computational fluid dynamics in three dimensions," *Journal of Statistical Physics*, vol. 68, pp. 379-400 , 1992.

[97] McNamara G., and Alder B., "Lattice Boltzmann Simulation of High Reynolds Number Fluid Flow in Two dimensions," *Microscopic Simulations of Complex Hydrodynamic Phenomena*, edited by M. Mareschal and B. L. Holien (Plenim, New York, 1992).

[98] Martinez D. O., Matthaeus W. H., Chen S., and Montogomery D. C., "Comparison of spectral method and lattice Boltzmann simulations of two-dimensional hydrodynamics," *Physics of Fluids*, vol. 6, Issue 3, pp. 1285-1298, 1994.

[99] Rothman D., "Macroscopic laws for immiscible two-phase flow in porous media: results from numerical experiments," *Journal of Geophysical Research*, vol. 95, pp. 8663-8674, 1990.

[100] Chen S., Diemer K., Doolen G. D., Eggert K. Fu C., Gutman S., and Travis B. J., "Lattice gas automata for flow through porous media," *Physica D*, vol. 47, pp. 72-84, 1991.

[101] Chen H., and Matthaeus W. H., "New cellular automaton model for magnetohydrodynamics," *Physical Review Letters*, vol. 58, pp. 1845-1848, 1987.

[102] Martinez D. O., Chen S., and Matthaeus W. H., "Lattice Boltzmann magnetohydrodynamics," *Physics of Plasmas*, vol. 1, Issue 6, pp. 1850-1867, 1994.

[103] Rothman D., and Keller J. M., "Immiscible cellular-automaton fluids," *Journal of Statistical Physics*, vol. 52, pp. 1119-1127, 1988.

[104] Somers J. A., and Rem P., "Analysis of surface tension in two-phase lattice gases," *Physica D*, vol. 47, pp. 39-46, 1991.

[105] Gurunau D., Chen S., and Eggert K., "A lattice Boltzmann model for multi-phase fluid flows," *Physics of Fluids A*, vol. 5, Issue 10, pp. 2557-2562, 1993.

[106] Shan X., and Chen H., "Lattice Boltzmann model for simulating flows with multiple phases and components," *Physical Review E*, vol. 47, Issue 3, pp. 1815-1819, 1993.

[107] Dab D., Lawniczak A., and Masiar P., "Lattice-gas automata for coupled reaction-diffusion equations," *Physical Review Letters*, vol. 66, Issue 19, pp. 2535-2538, 1991.

[108] Kapral R., Lawniczak A., and Masiar P., "Oscillations and waves in a reactive lattice-gas automaton," *Physical Review Letters*, vol. 66, Issue 19, pp. 2539-2542, 1991.

[109] Dawson S. P., Chen S., and Doolen G. D., "Lattice Boltzmann computations for reaction-diffusion equations," *Journal of Chemical Physics*, vol. 98, Issue 2, pp. 1514-1523, 1993.

[110] Kuksenok O., Yeomans J. M., Balazs A. C., "Creating localized mixing stations within micro fluidic channels," Langmuir, vol. 17, No. 23, pp. 7186–7190, 2001.

[111] Lim C. Y., Shu C., Niu X. D., and Chew Y. T., "Application of lattice Boltzmann method to simulate microchannel flows," *Physics of Fluids*, vol. 14, No. 7, pp. 2299–308, 2002.

[112] Wang H., and Menon S., "Fuel-Air Mixing Enhancement by Synthetic Microjets," *AIAA Journal*, Vol. 39, No. 12, December 2001.

[113] Mautner T., "Application of the synthetic jet concept to low Reynolds number biosensor microfluidic flows for enhancing mixing: a numerical study using the lattice Boltzmann method," *Biosensors and Bioelectronics*, vol. 19, pp. 1409-1419, 2004.

[114] Bourgat, J. F., Tallec, P. L., and Tidriri, M. D., "Coupling Boltzmann and Navier-Stokes equations by friction," *Journal of computational physics*, vol. 127, pp. 227–245, 1996.

[115] Tallec, P. L. and Mallinger, F., "Coupling Boltzmann and Navier-Stokes equations by half flux," *Journal of computational physics*, vol. 136, pp. 51–67, 1997.

[116] Crouseilles, N., Degond, P., and M., L., "A hybrid kinetic/fluid model for solving the gas dynamics Boltzmann-BGK equation," *Journal of Computational Physics*, vol. 199, pp. 776-808, 2004.

[117] Degond P., Jin S., and Misussens L., "A smooth transition model between kinetic and hydrodynamic equations," *Journal of Computational Physics*, vol. 209, pp. 665–694, 2005.

[118] Nourgaliev R.R., Dinh T.N., Theofanous T.G., Joseph D., "The lattice Boltzmann equation method: theoretical interpretation, numerics and implications," *International Journal of Multiphase Flow*, vol. 29, pp. 117-169, 2003.

[119] Kolobov, V. I., Arslanbekov, R. R., Aristov, V. V., Frolova, A. A. and Zabelok, S. A., "Unified solver for rarefied and continuum flows with adaptive mesh and algorithm refinement," *Journal of Computational Physics*, Vol. 223, pp. 589-608, 2007.

[120] Lätt, J., "Hydrodynamic Limit of Lattice Boltzmann Equations," PhD Dissertation, University of Geneva, 2007.

[121] Iourokina, I. V. and Lele, S. K., "Towards Large Eddy Simulation of Film-Cooling Flows on a Model Turbine Blade Leading Edge," 43rd AIAA Aerospace Sciences Meeting and Exhibit, 10-13 January 2005, Reno, Nevada, AIAA 2005-670.

[122] Hou, Y. and Mahesh, K., "A robust, collocated, implicit algorithm for direct numerical simulation of compressible, turbulent flows," *Journal of Computational Physics*, Vol. 205, Issue 1, pp. 205-221, 2005.

[123] Tannehill, J. C., Anderson, D. A., and Pletcher, R. H., "Computational Fluid Dynamics and Heat Transfer," *Series in Computational and Physical Processes in Mechanics and Thermal Sciences*, second edition.

[124] Martin P.B, Tung C., Chandrasekhara M. S., and Arad E, "Active Separation Control: Measurements and Computations for a NACA 0036 Airfoil," AIAA 2003-3516, 2003.

[125] Wilson, J. S., "Turbulence measurements on a 2D NACA 0036 with synthetic jet flow control," *62nd AHS Annual Forum*, Phoenix, AZ, May 2006, p. 106-122. Also, AIAA 2006-3157, 2006.

[126] Arad E., Martin P.B., Wilson J., and Tung C., "Contol of Massive Separation on A Thick-Airfoil Wing: A Computational and Experimental Study," AIAA 2006-322, 2006.

[127] Sellers, W. L. and Rumsey, C. L., Langley research center workshop: CFD validation of synthetic jets and turbulent separation control. URL: http://cfdval2004.larc.nasa.gov (cited 4 May 2005).

[128] Rumsey, C. L., Gatski, T. B., Sellers III, W. L., Vatsa, V. N., and Viken, S. A., "Summary of the 2004 computational fluid dynamics validation workshop on synthetic jets," *AIAA Journal* 2006; 44(2):194–207. also AIAA Paper 2004-2217, June–July 2004.

[129] Rumsey, C. L., “Reynolds-Averaged Navier-Stokes Analysis of Zero Efflux Flow Control over a Hump Model,” *Journal of Aircraft*, Vol. 44, No. 2, March-April 2007.

[130] Yeshala N., Min, B. Y., and Sankar L. N., “Drag Reduction Using Active Flow Control,” AIAA 2008-2870, *4th Flow Control Conference*, 23-26 June, 2008, Seattle, Washington.

[131] Min, B. Y. and Sankar, L. N., “Enhancements to a Hybrid Navier-Stokes/Free Wake Method for Improved Prediction of Blade-Vortex-Interaction Phenomena,” AIAA 2009-3860, *27th AIAA Applied Aerodynamics Conference*, San Antonio, Texas, June 22-25, 2009.

[132] Min, B. Y., Lee, W., Englar, R. and Sankar, L. N., “Numerical Investigation of Circulation Control Airfoils,” *Journal of Aircraft*, Vol. 46, No. 4, July-August 2009, pp. 1403-1410.

[133] Min, B. Y., “A Physics Based Investigation of Gurney Flaps for Enhancement of Rotorcraft Flight Characteristics,” *PhD Thesis*, Georgia Institute of Technology, Atlanta, 2010.

[134] Roe, P. L., "Approximate Riemann Solvers, Parameter Vectors, and Difference Schemes," *Journal of Computational Physics*, Vol. 43, 1981, pp. 357-372.

[135] Van Leer, B. "Upwind Difference Methods for Aerodynamic Problems Governed by the Euler Equations," *Lectures in Applied Mathematics*, Vol. 22, 1985.

[136] Van Albada, G. D., van Leer, B., and Roberts, W. W. Jr., "Comparative Study of Computational Methods in Cosmic Gas Dynamics," *Astronomy and Astrophysics*, Vol. 108, 1982, pp. 76-84.

[137] Vinokur, M. and Liu, Y., "Equilibrium Gas Flow Computations. II. An Analysis of Numerical Formulations of Conservation Laws," AIAA Paper 88-0127,1988.

[138] Pulliam, T. H. and Steger, J. L., "Implicit Finite Difference Simulations of Three Dimensional Compressible Flow," *AIAA Journal*, Vol. 18, No. 2, 1980, pp. 159-167.

[139] Yoon, S. and Jameson, A., "Lower-Upper Symmetric-Gauss-Seidel Method for the Euler and Navier-Stokes Equations," *AIAA Journal*, Vol. 26, No.9, 1988, pp. 1025-1026.

[140] Spalart, P. R. and Allmaras, S. R., "A One-Equation Turbulence Model for Aerodynamic Flows," *La Recherche Aerospatiale*, 1994.

[141] Hoffmann, K. A. and Chiang, S. T., *Computational Fluid dynamics Volume II, Fourth Edition*, Engineering Education System, Wichita, Kansas, 2000.

[142] Sellers, W. L. and Rumsey, C. L., Langley research center workshop: CFD validation of synthetic jets and turbulent separation control. URL: http://cfdval2004.larc.nasa.gov (cited 4 May 2005).

[143] Rumsey, C. L., Gatski, T. B., Sellers III, W. L., Vatsa, V. N., and Viken, S. A., "Summary of the 2004 computational fluid dynamics validation workshop on synthetic jets," *AIAA Journal* 2006; 44(2):194–207. also AIAA Paper 2004-2217, June–July 2004.

[144] Bogoliubov, N., "Problems of a dynamical theory in statistical mechanics," *Studies in Statistical Mechanics*, Vol .1, Amsterdam, Netherlands. J. de Boer, G. E. Uhlenbeck, 1962.

[145] Wolf-Gladrow, D. A., "Lattice-Gas Cellular Automata and Lattice Boltzmann Models," Springer, 2000.

[146] Treibig, J., "Simulation von Gas-Feststoff-Mehrphasensystemen mit dem Lattice Boltzmann Verfahren," *PhD Thesis*, Universitaet Erlangen-Nuernberg, Erlangen, Germany, 2002.

[147] Bronstein, Semendjajew, Musiol, and M¨uhlig, "Taschenbuch der Mathematik. Verlag Harri Deutsch," 1999.

[148] Harris, S., "An Introduction to the Theory of the Boltzmann Equation," Holt, Rinehart and Winston Inc., 1971

[149] Thürey, N., "A single-phase free-surface Lattice Boltzmann Method," *PhD Thesis*, Friedrich-Alexander-Universität Erlangen-Nürnberg, 2003.

[150] Schäfer M. and Turek S., "Benchmark computations of laminar flow around a cylinder," in Flow Simulation with High-Performance Computers II, edited by E.H. Hirschel, Notes in Numerical Fluid Mechanics (Viewed Braunschweig, 1996), Vol. 52, pp. 547-566.

[151] Mei R., Yu D., Shyy W., "Force evaluation in the lattice Boltzmann method involving curved geometry," *Physical review E*, Vol. 65, 041203, 2002.

[152] Yeshala, N. and Sankar, L.N., "Boundary Condition Implementation for a Coupled Lattice Boltzmann and Navier-Stokes Methodology," AIAA 2010-715-273.

[153] Glezer, A., Amitay, M. and Honohan, A. M., "Aspects of Low- and High-Frequency Actuation for Aerodynamic Control," *AIAA Journal*, Vol. 43, No. 7, July 2005.

[154] Xu J. and Ma, H., "Applications of URANS on predicting unsteady turbulent separated flows," *Acta Mechanica Sinica*, Vol. 25, No. 3, pp 319-324.

[155] Seele, R., Tewes, P., Woszidlo, R., McVeigh, M. A., Lucas, N. J. and Wygnanski, I. J., "Discrete Sweeping Jets as Tools for Improving the Performance of the V-22," *Journal of Aircraft*, Vol. 46, No. 6, November-December, 2009.

[156] Tewes, P., Taubert, L. and Wygnanski, I. J., "One of the Use of Sweeping Jets to Augment Lift of a Lambda Wing," 28th AIAA Applied Aerodynamics Conference, 28 June – 1 July 2010, Chicago, Illinois, AIAA 2010-4689.

[157] Ribeiro, J. L. D., "Effects of surface roughness on two-dimensional flow past circular cylinders I: mean forces and pressures," *Journal of Wind Engineering and Industrial Aerodynamics*, Vol. 37, 1991, pp. 299-309.